An investigation of machining induced residual stresses on Grade 4 and 5 titanium alloys

by

Kyle Douglas Edkins

200601286

A dissertation submitted to the Faculty of Engineering in partial fulfilment of the requirements for the degree of

MAGISTER INGENERIAE

in

MECHANICAL ENGINEERING

in the

FACULTY OF ENGINEERING AND THE BUILT ENVIRONMENT

at the

UNIVERSITY OF JOHANNESBURG

Supervisor: Prof R.F. Laubscher

Co-Supervisor: N. Janse van Rensburg

2012

Abstract

Titanium and its alloys have the potential to serve as a strategic economic driver of the South African economy. The manufacture and use of high strength, lightweight materials such as titanium alloys have become of great importance in the aerospace and biomedical industries over the past few decades. The manufacturing costs of titanium alloy components however, are considered high due to the poor machinability of the material. Furthermore, as with all metals during machining, surface residual stresses are induced into the material. These are of particular interest in the aerospace industry as they can be either detrimental or beneficial to the performance and fatigue life of materials. The aim of this investigation is therefore to examine the effect that machining parameters have on the magnitude, sign and distribution of residual stresses induced in Grade 4 and 5 titanium alloys during high performance machining (turning).

The effect of these machining parameters is investigated by residual stress measurements conducted with X-ray diffraction and grain structure analysis of the machined surfaces by optical microscopy. Results show that cutting speed and depth of cut have a significant effect on the residual stresses. At low cutting speeds, the surface residual stresses are largely compressive, becoming more tensile with an increase in cutting speed. An increase in depth of cut also introduces more compressive residual stresses into the material. The microstructural analysis of the alloys shows that grain deformation decreases with an increase in cutting speed and cutting depth.

Table of Contents

List of Figures

List of Tables

Chapter 1. Introduction

1.1 General remarks

South Africa is the second largest producer of Titanium-bearing minerals in the world, delivering approximately 22% of global production thereof, only second to Australia with 29% production [1]. Canada and China produce 16% and 10% respectively while the rest of the world produces the remaining 23%. Furthermore, Richards Bay Minerals in KwaZulu-Natal, South Africa, is known for being the largest producer of titanium slag in the world [2]. Despite the increasing need for titanium and South Africa having rich mineral reserves, a large amount of this production is unexploited and exported to other countries for manufacturing. The benefits for South Africa of adding value to these minerals before being sold to other countries is vital in the socio-economic impact and incentive of sustainable development. Recently, The National Development Plan, the New Growth Path, and the associated Industrial Policy Action Plan, of South Africa, all documented a plan to increase the beneficiation of strategic minerals, including titanium, in order to improve the value of exports and encourage investment into manufacturing [3]. Currently, the national market for titanium metal is limited to only approximately 5% of its potential size. This equates to only about 200 000 tons per year [4]. The utilisation and production of titanium and its alloys will however continue to increase due to the salient benefits of titanium. Whether South Africa becomes a major contender in global titanium component production on the other hand, depends on the improvement of titanium alloy manufacturing, and therefore the ability to “intelligently” and effectively machine titanium and its alloys to increase the strength and fatigue life of machined components.

Titanium alloys are of great engineering importance due to their high specific strength maintained at elevated temperatures, low density, exceptional

resistance to corrosion, and fracture resistance [5,6]. These properties of titanium alloys have in the past two decades increased its use in aerospace (jet engines, missiles, and spacecraft), the military, industrial processes (chemicals and petro-chemicals, desalination plants, pulp and paper), automotive fields, agri-food, medical prostheses, orthopaedic implants, dental and endodontic instruments, dental implants, sporting goods, jewellery, mobile phones, and other applications [7]. The titanium alloys of interest to this investigation are Grade 4 and 5. Grade 5 is the most extensively used titanium alloy, accounting for nearly 60% use. It is generally the material of choice where high strength and low density is required. Grade 4 is a commercially pure titanium alloy that is also extensively used. It is used in the biomedical field and offers excellent corrosion resistant properties and reasonable strength. Aerosud and Denel Aviation are among a few major corporations in South Africa whom utilise Grade 5 in the manufacture of lightweight aerospace technology. Southern Implants, another South African corporation, utilise Grade 4 for implants in the biomedical field.

Despite the beneficial properties of titanium, the use and application thereof is considered low when compared to other engineering materials such as steel. This is mainly due to titanium alloys having high production costs and being difficult to machine. The high cost of titanium alloy component production is attributed to material costs being exasperated by the complexity of the extraction process and difficulty experienced during melting and manufacturing [8,9]. In most cases, when manufacturing machined titanium alloy components, the majority of the material, up to 95% of the bulk material, is machined away. Therefore, machining may comprise a significant part of the fabrication process and is an important step in the production of titanium alloy components. Reducing machining time and improving machining techniques will increase productivity and significantly reduce production costs. High Performance Machining (HPM) and High Speed Machining (HSM), a subset thereof, are therefore incorporated to increase this productivity. HSM is defined as machining done at high cutting speeds, as well as at higher values of other machining parameters than conventional

machining values. HPM incorporates HSM along with high precision machining. For these techniques to be implemented, their effect on surface integrity needs to be evaluated [5].

Titanium alloys have a poor machinability. This causes difficulties during machining and can be attributed to their physical properties. Properties such as a strong alloying tendency or chemical reactivity with most tool materials causes rapid cutting tool destruction, welding and smearing at the interacting surface [10]. Low thermal conductivity increases the temperature at the tool-workpiece interface which in turn considerably diminishes the tool life [6,11]. Other properties of high strength at elevated temperatures, low modulus of elasticity, and resistance to wear and chemical degradation also affect the machinability of titanium alloys. These properties cause problems of chatter and excessive tool wear [5,12] and affect the surface integrity of the material. Surface integrity is used to describe the characteristics of a machined surface and its relationship to functional performance. It can be divided into two aspects, namely the external topography of surfaces, and the microstructure, mechanical properties and residual stresses of internal subsurface layers [13].

Machining may introduce significant surface residual stresses. Residual stresses are internal stresses that are locked within a component when no external loads are present [14]. Manufacturing and processing methods of titanium alloy components induce residual stresses through plastic deformation and/or thermal gradients created at the tool-workpiece interface. The residual stresses can be either detrimental to the performance and fatigue life of the component or enhance these properties by increasing the component's durability. This is dependendant on the magnitude, sign and distribution of the stresses. Due to this influence on component performance, it is important that residual stresses and their effects on the mechanical properties are closely examined [15]. Evaluation of residual stresses provides a means for process control, quality control, design assessment and failure analysis [16]. Literature shows that depth of cut and cutting speed are the parameters which most affect

induced residual stresses. It is further suggested that these parameters also affect the grain orientation near the surface of machined components [17]. Hence, to add value and even further expand the application and production of titanium and its alloys in South Africa, the effect that these machining parameters have on induced residual stresses on Grade 4 and 5 titanium alloys is investigated.

1.2 Aim of investigation

The aim of this research is to investigate the machining induced residual stresses during turning of Grade 4 and 5 titanium alloys. More specifically, it is to evaluate the effect of cutting speed and depth of cut on these induced residual stresses. The nature of the residual stresses and the microstructural changes near the machined surface are investigated.

1.3 Scope of investigation

In order to address the aim of the investigation, as stipulated above, the following scope is required:

1. A literature review carried out to investigate the current state of technology and knowledge on the effect of cutting parameters on machining induced residual stresses of titanium alloys.
2. The mechanical properties of Grade 4 and 5 be evaluated by compression and microhardness tests.
3. Experimental work be conducted by machining Grade 4 and 5 on a Computer Numerical Control (CNC) lathe.
4. Determination of induced residual stresses.
5. Examination of microstructure to determine affected zone.
6. Presentation of results, discussion and conclusion.

1.4 Document preview

Chapter 1 outlines the problem statement and aim of the investigation. Chapter 2 presents a detailed review on the relevant literature concerning this investigation. It contains information regarding the materials used, mechanical property testing, machining, residual stresses, residual stress measurement, and microstructural analysis.

In Chapter 3, a comprehensive experimental setup is presented. The experimental fields include mechanical property evaluation, machining, sample preparation, residual stress measurement and microstructural analysis. The mechanical property evaluation comprises of microhardness and compression testing.

Chapter 4 illustrates the results and discussion of the findings. A comparison is made between residual stress change and machining parameters. The microstructural analysis, including grain shift and deformation, is also presented and compared.

Chapter 5 outlines the conclusions and the most important outcomes of the investigation. An evaluation of the problem statement and hypothisis, as outlined in Chapter 1, is also conducted. Potential and encountered problems are summarised, with opportunities for further work discussed.

Chapter 2. Literature Review

Certain research topics are reviewed for the investigation of machining induced residual stresses on titanium alloys. These are presented and discussed in the following subsections. The principal research topics of concern in this investigation include:

- Titanium, its alloys and properties;
- Mechanical property evaluation, including compression and microhardness testing;
- Machining, machining methods and machinability of titanium alloys;
- High performance machining
- Residual stresses
- Residual stress measurement techniques, including the hole-drilling method, digital image correlation, X-ray diffraction and synchrotron diffraction; and
- Microstructural analysis, by optical microscope and Scanning Electron Microscope (SEM)

2.1 Titanium

Titanium is considered a transition metal on the periodic table of elements with an atomic number of 22 and an atomic weight of 47.90. The atomic symbol used for titanium is Ti [18]. Titanium was first recognised by William Gregor in 1791, but was only named in 1795 by M.H. Klaproth where it was named after the “titans” who were said to be the mythological first sons of the Earth. Impure titanium was first prepared in 1887 by Nilson and Pettersson, but it was only in 1910 that the first pure metal (99.9%) was made when Matthew Hunter heated $TiCl_4$ with sodium in a steel bomb. William Kroll, however, then began experimenting with methods of efficiently isolating titanium, and this lead to the development of the Kroll process of isolating

titanium by reduction with magnesium in 1937. The first products of titanium were then introduced in the 1940's where components such as wires, sheets, and rods were made. It was not until 1947 though that titanium was produced in a large-scale under the direction of R.S. Dean where various modifications were made to Kroll's process in order to produce titanium on a large scale [18,19].

Titanium is the fourth most abundant metal and makes up approximately 0.62% of the earth's crust, but is seldom found in its pure form. It is generally found in minerals such as anatase, brookite, ilmenite, leucoxene, perovskite, rutile, and sphene, of which ilmenite, leucoxene, and rutile are considered the primary ores used for titanium production. Ilmenite (FeTiO3) and leucoxene contain 53% and 90% titanium dioxide (TiO2) and are typically found in hard rock deposits or in beaches and alluvial sands. Rutile however, is fairly pure titanium dioxide and is also found in beach and sand deposits. Although titanium is rather abundant, it is expensive when it comes to its production. This is due to the complexity of the extraction process, its difficulty to isolate [18], difficulty of melting, and problems during fabrication and machining of the titanium [8,9].

Some of the leading benefits of titanium and its alloys include a high specific strength (strength-to-weight ratio) which is maintained at elevated temperatures, exceptional resistance to corrosion, and fracture resistance [5,6,20-22]. To put its strength to weight ratio in perspective, commercially pure titanium has the same strength as mild steel, but is 45% lighter. When compared to aluminium it is 60% heavier, but twice as strong. This high strength to weight ratio, along with the high temperature properties of titanium make it useful to the aerospace industry [23,24]. Some of these physical properties of commercially pure titanium can be seen in Table 2.1. There are numerous applications of titanium and its alloys due to these properties. Approximately 80% of titanium alloys are used in the aerospace industry, such as for production of gas turbines etc. The remaining 20% is used by non-

aerospace industries, for example the production of various pumps, valves, and heat exchangers in the chemical processing industry. This is due to the material's corrosion resistance and resistance to chlorine and acid. Another useful property of titanium also allows it to be used in human implants, due to its compatibility with the human body. This makes it useful in hip replacements, pacemakers, defibrillators, and elbow and hip joints [18]. Other industrial and commercial applications include petroleum refining, surgical implantation, pulp and paper, pollution control, nuclear waste storage, food processing, electrochemical (including cathodic protection and extractive metallurgy) and marine applications [8].

Table 2.1 - Physical properties of commercially pure titanium [25]

Property	Value
Density	4510 kg/m^3
Tensile strength, ultimate	240 MPa
Tensile strength, yield	170 MPa
Modulus of elasticity	103GPa
Poisson's ratio	0,34
Specific heat capacity	528 $J/kg°C$
Thermal conductivity	16 $W/m°C$
Melting point	1671 $°C$

In conclusion, pure titanium is a relatively new engineering material with unique material properties. Although it is the fourth most abundant metal in the earth's crust, it is considered to be an exotic, highly specialised material. Titanium is however seldom used in its pure form. It is most often used in alloy form. There are many grades of titanium alloys, each with unique characteristics and properties. These are further discussed in the following section.

2.2 Titanium alloys

Titanium alloys are formed by adding alloying elements to pure titanium. These impurities enhance the properties of the material and increase its demand [18]. An allotropic transformation takes place at 882°C whereby pure titanium changes from a low temperature α-phase hexagonal-close-packed (hcp) structure to a higher temperature β-phase body-centred-cubic (bcc) structure. There are two types of stabilisers that alter the temperature at which the transformation from hcp to bcc occurs. These stabilisers are known as the α-stabilisers and β-stabilisers. α-stabilisers increase the transformation temperature, whereas β-stabilisers decrease the transformation temperature [26].

The α-stabilisers include aluminium, oxygen, nitrogen or carbon. When added to titanium, they raise the temperature as shown in Figure 2.1 (a). Tin or zirconium can also be added to titanium to increase its strength, but they do not have any effect on the transformation temperature, as seen in Figure 2.1 (b). They are therefore classified as neutral elements.

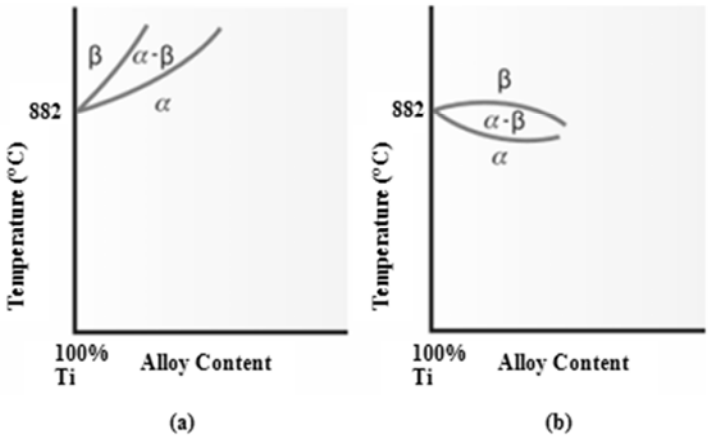

Figure 2.1 - The effect of α-stabilizers and neutral elements on titanium alloys [27]

The β-stabilisers on the other hand can be divided into two different categories depending on their influence when added to titanium. The β-isomorphous

elements, such as molybdenum, vanadium, niobium and tantalum have mutual solubility with titanium. With an increase in addition of these solute elements, the transformation temperature progressively decreases as seen in Figure 2.2 (a). The β-eutectoid elements, such as iron, chromium, copper, silicon and manganese have restricted solubility and form intermetallic compounds by eutectoid decomposition of the beta phase. The phase diagram is illustrated in Figure 2.2 (b) [27].

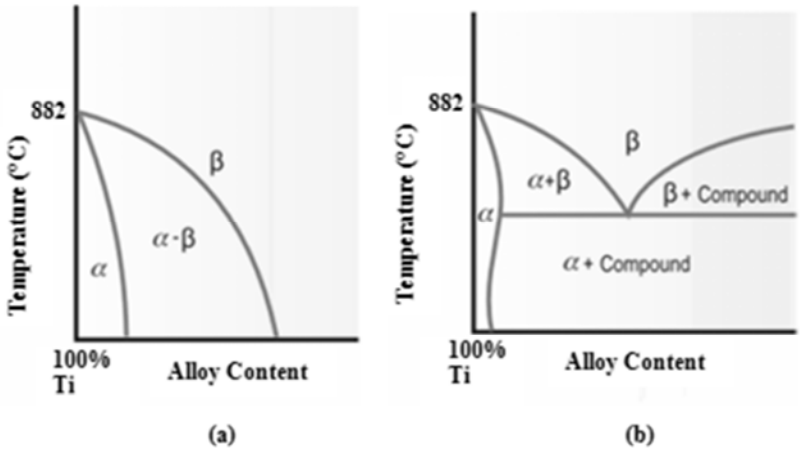

Figure 2.2 - The effect of (a) β-isomorphous elements and (b) β-eutectoid elements on titanium alloys [27]

Titanium alloys can be divided into four main categories, namely α-alloys, near α-alloys, α-β-alloys, and β-alloys. The α-alloys are the commercially pure grades of titanium which include iron and oxygen as some of their alloying elements. Grade 4 is part of this category, as it is a commercially pure grade. They are not heat treatable and are used in low temperature applications for corrosion resistance. They contain α-stabilisers as well as neutral alloying elements. Near α-alloys are used at operating temperatures between 400 and 520°C. They are used as non-structural components in aircrafts and contain mainly α-stabilisers with only a few β-stabilisers. They also mainly compose of α-phase titanium. α-β-alloys include both α- and β-stabilisers. Ti-6Al-4V (Grade 5), is part of the α-β-alloys and is the most used titanium alloy. They are used at temperatures between 315 and 400°C and for high strength applications. They can also be heat treated to an even higher strength. β-alloys

have large amounts of β-stabilisers which allow them to be completely β-phase when quenched. They can also be strengthened by solution treating [6,26].

Titanium alloys are available in a number of different grades. The commercially pure grades of titanium alloys include Grades 1 through 4, as identified in ASTM B265. Each grade contains a different amount of alloying elements with Grade 1 having the lowest amount. Grade 4 is stronger and less ductile than Grade 1. Grade 4 also contains higher levels of oxygen. This oxygen, along with nitrogen and carbon, dissolve interstitially into the crystal structure and strengthen the alloy by solid solution hardening. Oxygen is therefore the main alloying element controlling the strength of the commercially pure titanium alloy grades. Other properties of Grade 4 include good formability and corrosion resistance [28]. The composition of Grade 4 is presented in Table 2.2. It can be seen that only a small amount of alloying elements exist. For instance, there is only 0.4% oxygen and 0.1% carbon of the weight. Pure titanium is dominant with 99% of the weight [28,29].

Table 2.2 - Grade 4 chemical composition

Component	Wt. %
C	Max 0.1
Fe	Max 0.5
H_2	Max 0.015
N_2	Max 0.05
O_2	Max 0.4
Ti	Balance

The physical properties of Grade 4 are presented in Table 2.3 [29,30]. As can be seen, the ultimate strength of ±550 MPa is higher in comparison, for example, than mild steel with an ultimate strength of typically 400 MPa.

Table 2.3 - Grade 4 physical properties

Property	Value
Density	4510 kg/m^3
Tensile strength, ultimate	550 *MPa*
Tensile strength, yield	485 *MPa*
Modulus of elasticity	105 *GPa*
Poisson's ratio	0,37
Specific heat capacity	530 $J/kg°C$
Thermal conductivity	17.2 $W/m°C$
Melting point	Max 1660 °*C*

An example of the microstructure of Grade 4 is presented in Figure 2.3. Typically, a slightly smaller grain size is realised for Grade 4 when compared to Grade 2, depending on the manufacturing process. This partly explains why Grade 4 has superior mechanical properties as opposed to Grade 2.

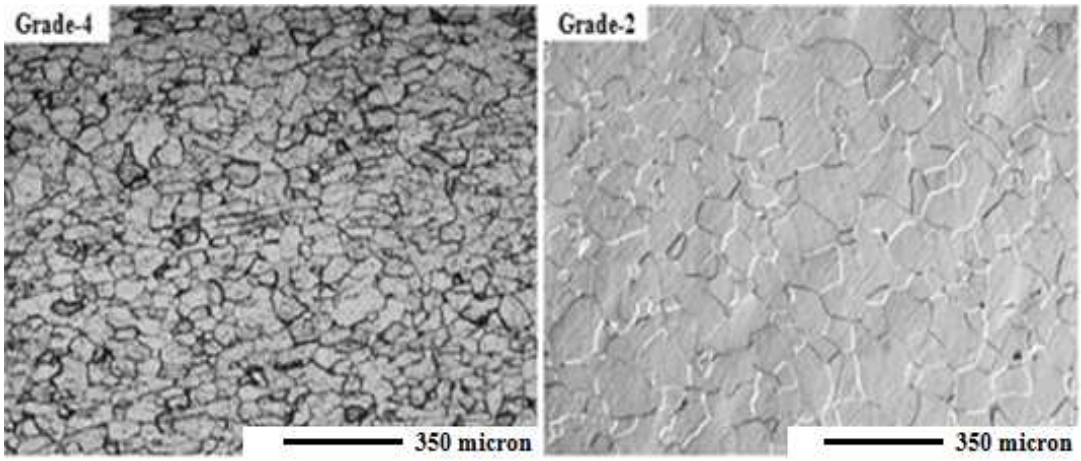

Figure 2.3 - Optical micrographs showing the equiaxed and Coarse Grained (CG) microstructures of Gr 4 and Gr 2 with average grain sizes of 70 µm and 110 µm, respectively [31]

Grade 5 on the other hand, also known as Ti-6Al-4V, has a considerably higher strength when compared to Grade 4. The maximum yield strength is comparable to that of high strength steels, but at a lower specific gravity of 4.5 as opposed to 7.8. Ti-6Al-4V is used in applications up to temperatures of

400°C and retains more than 50% of its yield strength at 300°C. Its high resistance to deformation at elevated temperatures reduces considerably above temperatures of approximately 800°C [26]. The composition of Ti-6Al-4V is presented in Table 2.4. It is noted that the amount of alloying elements are greater than that of Grade 4.

Table 2.4 - Grade 5 chemical composition [32]

Component	Wt. %
C	Max 0.8
Fe	Max 0.25
N_2	Max 0.05
O_2	Max 0.2
Al	5.5-6.76
V	3.5-4.5
H_2(sheet)	Max 0.015
H_2(bar)	Max 0.0125
H_2(billet)	Max 0.01
Ti	Balance

Table 2.5 contains the physical properties of Ti-6Al-4V. It can be seen that the strength of Ti-6Al-4V is much larger in comparison to Grade 4. Ti-6Al-4V has a typical ultimate strength of 950 MPa, which outperforms the 550 MPa for Grade 4. This shows that an increase in alloying elements strengthens the material.

Table 2.5 - Grade 5 physical properties [33]

Property	Value
Density	$4420 kg/m^3$
Tensile strength, ultimate	$950 MPa$
Tensile strength, yield	$880 MPa$
Modulus of elasticity	$113.8 GPa$
Poisson's ratio	0,342
Specific heat capacity	$560 J/kg°C$
Thermal conductivity	$7.2 W/m°C$
Melting point	$1641 °C (\pm 15°C)$

Grade 4 and 5 do however comprise of certain properties that affect their machinability. These properties include being chemically reactive, having a low thermal conductivity and modulus of elasticity, and the ability to maintain a high strength at elevated temperatures. Their effect on the machining and machinability of titanium alloys is discussed in more detail in a later subsection. Before these effects can be discussed however, the properties of the individual materials are evaluated.

2.3 Mechanical property evaluation

It is important, from a material characterisation point, to evaluate the materials under investigation in terms of their mechanical properties. To obtain these properties, certain material characterisation tests are performed. The definition of material characterisation, according to the ASM-International Materials Characterisation Handbook states that: "Characterisation describes those features of composition and structure (including defects) of a material that are significant for a particular preparation, study of properties, or use, and suffice for reproduction of the material" [34]. When used in materials science, material characterisation refers to the utilisation of external techniques in order to investigate the internal structure and properties of a certain material [35]. Characterisation tools include that of microscopy and failure analysis

techniques, traditional inspection methods as well as non-destructive methods, and advanced mechanical testing [36]. Two separate material characterisation techniques are conducted in this investigation, namely compression tests and microhardness tests. These techniques are briefly discussed in this section.

2.3.1 Compression testing

Compression testing of metallic materials is usually conducted when tensile testing cannot be conducted for a variety of reasons. In general, compression test specimens are simpler and require less material. The same range of material properties, as available for the tensile test, may be obtained except for the tensile strength and ductility. Compression tests can determine the yield strength, yield point, Young's modulus, stress-strain curve, and the compressive strength. The compressive properties obtained from the compression tests are important in the analysis of structures that are subject to compressive and bending loads. They are also important in the analysis of metal working and fabrication processes where large compressive deformations occur. Even though the compression test is not complicated by means of necking, such as that obtained during tension testing of certain materials, buckling and barrelling are issues that can complicate the results [37]. An example of a compression test machine is presented in Figure 2.4.

Figure 2.4 - INSTRON compression test machine [38]

2.3.2 Microhardness testing

Hardness testing is a relatively simple mechanical testing technique that provides useful comparative information about a material's strength (yield strength). Fundamentally a hardness value is obtained by measuring the size of a permanent indentation made by applying an indenter, with known geometry and force, to a flat surface. The softer the material, the larger the indentation. Most hardness testing techniques provide an overall assessment of the material's hardness which is directly related to its yield strength.

Microhardness testing does essentially the same except that the loads, and therefore the indentations, are much smaller. The indentations are usually not visible to the naked eye. This allows for localised hardness testing of features such as surface layers, different phases etc. This is of special significance for the current investigation because it makes it possible to evaluate the local mechanical properties of the materials.

According to the ASTM E384 standard for measuring microhardness, a diamond indenter is used to make an indentation on the surface of a metal. The size of the indent is then measured using a microscope and converted to a hardness value. The procedure is similar to that of a standard Vickers hardness test, except for being completed on a microscopic scale with higher precision instruments. There are two different types of indenters, namely a square base pyramid shaped diamond indenter and an elongated pyramid shaped diamond indenter. The square base indenter is used with the Vickers scale, whereas the elongated pyramid shaped indenter is used with the Knoop scale. Before indentation however, the sample is first prepared so as to fit in the tester and be sufficiently smooth and perpendicular to the indenter. The material sample is usually cross sectioned, mounted into a plastic medium and polished to achieve a metallographic finish. This allows for a regular indentation shape and therefore improved measurements. Once mounted and positioned in the tester, the indenter is applied to the sample with a fixed load which ranges

from 10 to 1000 grams. The smaller the load used, the higher the surface finish that is required. The indentations made should therefore be as large as possible to maximise the measurement resolution. Measurement of the indentations is achieved by using precision microscopes which usually have a magnification of approximately 500 times. These microscopes can measure to an accuracy of approximately 0.5 micrometres. Considerable care and experience is required in order to achieve this accuracy [39-41]. An example of a microhardness tester is presented in Figure 2.5.

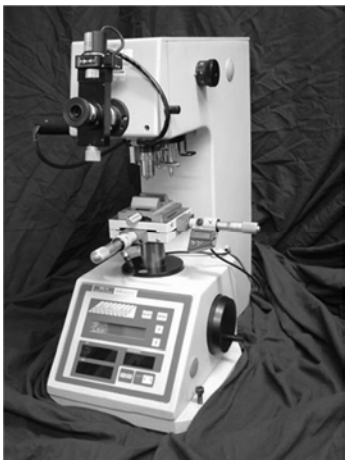

Figure 2.5 - ASTM E384 Knoop microhardness tester [39]

The effect that these properties have on the machining and machinability of titanium alloys is further described in Section 2.5, with a brief investigation into machining first presented in the following section.

2.4 Machining of materials

Machining is a term used to describe many different manufacturing processes designed to remove material from a workpiece [42]. There are several primary machining processes, namely, turning, shaping, milling, drilling, sawing, abrasive machining, and broaching. Many of these processes are used in the manufacture of titanium components. More advanced machining processes

that exist include Electric Discharge Machining (EDMs), laser cutting, chemical milling, high-pressure water cutting, and electrochemical machining.

All machining methods remove material from the workpiece to create certain shapes, angles or cuts. Some of the more commonly used machining methods include grinding, milling, drilling, wire electro-discharge machining (Wire EDM/WEDM), and turning. These methods are further discussed in this section, with turning being the technique central to this investigation.

2.4.1 Grinding, milling and drilling

Grinding is simply an abrasive machining process whereby material is removed in small chips/particles from the workpiece by means of a rotating wheel or disc. This rotating wheel is generally made from stone, diamond or other inorganic materials. Milling is a process whereby a rotating cutting tool on a spindle axis is used to remove a certain amount of material from a workpiece situated on a worktable. The worktable has the capability to manoeuvre in three directions with respect to the workpiece. Examples of typical operations carried out by a milling machine are slot and keyway cutting, planning, drilling, and contouring. Drilling is a technique whereby round holes are produced in the material by a rotating drill bit.

2.4.2 Wire EDM

Although the central theme of this investigation has to do with turning, wire EDM is extensively used during the sample preparation stage of this investigation. The technique of wire EDM is ideal for cutting the already machined titanium samples as it does not significantly add or change the induced residual stresses in the material. It is therefore briefly introduced here in more detail.

Wire EDM, which is the most recent and advanced process of those mentioned above, is a manufacturing technique that is used to achieve high precision cuts of complex shapes and hard metals such as titanium alloys. There are two primary parameters which govern the process of WEDM. These parameters include the power or electrical current, and the pause time [43]. WEDM uses a thermoelectric method whereby the workpiece is immersed in a dielectric fluid. Material is removed from the workpiece by means of melting and evaporation during single pulse sparks [44]. For this to occur however there must be electrical conductivity between the workpiece and electrode to create a spark [45].

Wire EDM primarily turns electrical energy into thermal energy to remove the unwanted material. As stated above, it achieves this by creating distinct electrical discharges between the work piece, which is immersed in a dielectric fluid, and an electrode [46-48]. As the electrode approaches the work piece, the gap between the two gets smaller until the voltage becomes large enough to ionise the dielectric [49]. The thermal energy which is generated from the electrical energy then creates a plasma channel between the workpiece and electrode [50] at temperatures in the region of 8000 - 12000°C [51] or even as high as 20000°C [52]. This causes a large amount of heat, and therefore localised melting of the material. Turning off the pulsed current supply of approximately 20000 - 30000 Hz [53] causes the plasma channel to break down, along with a sudden drop in temperature. This allows the dielectric fluid to wash away the molten material.

The fact that the wire EDM does not make any direct contact between electrode and work piece, eliminates most problems that may occur during the machining process. Examples of these problems include mechanical stresses, chatter, or vibration problems [54]. It can also cut through materials with any degree of hardness, provided the material is electrically conductive [55]. Wire EDM is therefore a non-abrasive cutting process which does not significantly affect the induced residual stresses.

2.4.3 Turning

Turning is fundamentally a cutting process where material is removed by the relative motion of a cutting tool on a rotating workpiece. Turning is an important manufacturing method that is applied to titanium alloys. It is a process whereby the workpiece rotates about a spindle axis and the cutting tool moves parallel to this axis [56]. The workpiece is held in position on its spindle axis by a chuck whereby an external, cylindrical shape is formed during material removal by the cutting tool. The machine used for turning is called a lathe. The different parameters considered with a lathe include cutting speed, feed rate and depth of cut (DOC). The cutting speed is the actual relative speed between the tool and workpiece and is influenced by or directly related to the rotational speed of the workpiece. The feed rate is the speed at which the cutting tool moves over the workpiece, and the DOC is the depth at which the cutting tool removes material from the workpiece. The parameters of concern for the current investigation however, include only the cutting speed and depth of cut, as outlined in Chapter 1. A Computer Numerical Control (CNC) lathe is a programmable and automatic lathe. It produces precise and accurate cuts at high speeds and is used for this investigation. Increasing the cutting speed also affects the cutting temperature and cutting force, which are recorded during machining.

There are three major factors that affect machining of metals during turning. These include the feed rate, geometry of the tool, and cutting speed. It has been found that low feed rates enhance the surface finish of metals. However, if too low, they may result in rubbing instead of actually cutting. Feed rates should generally not exceed approximately 80% of the tool nose radius value. The rake angle and clearance angle are features which have the greatest effect on the tool efficiency. The rake angle is the angle between the top face of the tool and the tool base for a horizontal tool. This angle can be positive, negative or neutral. The positive and negative rake angles are illustrated in Figure 2.6. The positive rake angle causes a decrease in frictional forces, forces on the

tool, and the area under shear. It also causes the chips to be thinner and the chip flow rate to be faster. The negative rake angle on the other hand causes an increase in frictional forces, forces on the tool, and the area under shear. The chips are also thicker and the chip flow rate is decreased [57].

Figure 2.6 - Positive and negative rake angles [57]

The total forces that are recorded in a cutting process can be attributed to the sum of the forces acting on the tool flank and its cutting edge, as well as on the face. There are three main forces that occur during this process i.e. the tangential/cutting force, the feed force and the active force. These are illustrated in Figure 2.7. Here, the active force is separated into the ploughing force and the chip forming force. The ploughing force is the force which directly acts on the cutting edge and is formed by plastic deformation of the material near the cutting edge [58]. This is the cutting force measured and monitored during machining for this investigation. It is used to define machining errors or irregularities experienced in the investigation.

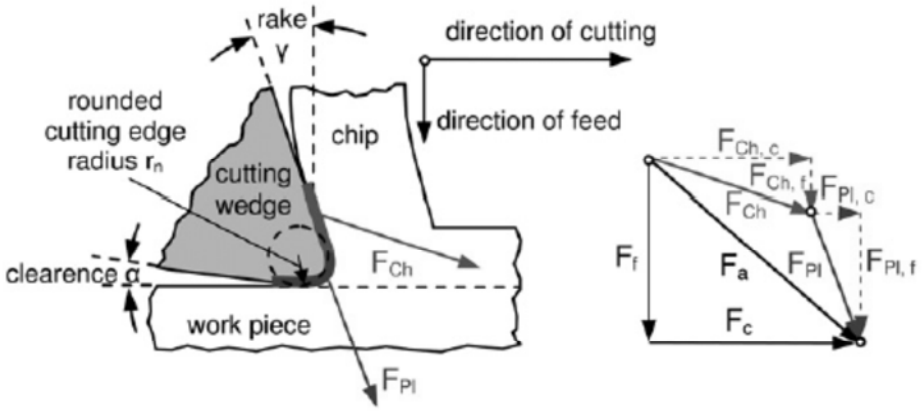

Figure 2.7 - Separation of active force F_a into ploughing force F_{Pl} and chip forming force F_{Ch} and components in feed and cutting direction [58]

The effects of slow cutting speeds tend to create a rough surface finish with segmented and broken chips. High cutting speeds on the other hand tend to create an enhanced surface finish, but in turn reduce the tool life. The cutting speed chosen is therefore important in preventing problems in chip formation and tool functionality. If too low, the chips are discontinuous and cause force fluctuations on the tool. If too high, the temperatures experienced at the interface become high and cause localised welding between the tool and workpiece (built-up edge). This built-up edge affects the cutting efficiency as it changes the geometry of the cutting tool. The built-up edge is however continuously torn away, but in so doing, adheres to either the chip or the workpiece and degrades the surface finish [57]. For the purpose of this investigation, the cutting speeds analysed range from speeds of 70 m/min to 300 m/min for Grade 4 and 70 m/min to 200 m/min for Grade 5. These are chosen to allow evaluation of both low and high cutting speed effects.

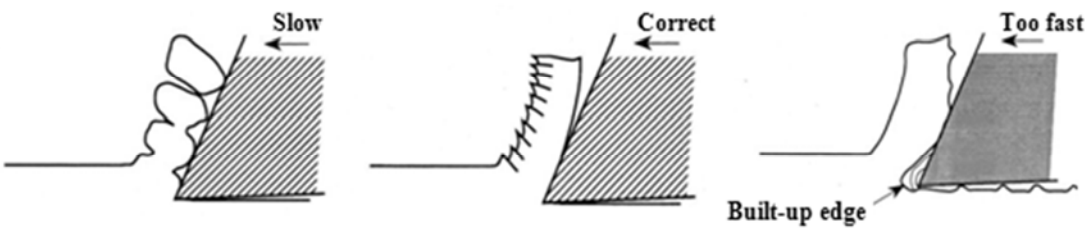

Figure 2.8 - Effect of cutting speed on cutting process [57]

In conclusion, certain problems can be caused during the turning process on titanium alloys. These problems aid in inducing residual stresses are better explained by understanding the machining and machinability of titanium alloys. The machining of titanium alloys is different to that of other materials and is therefore discussed in the following section.

2.5 Machining and machinability of titanium alloys

For machining of titanium, near net-shape methods have been introduced such as casting, isothermal forging, and powder metallurgy, in order to lower the cost of components [59-64] The majority of all titanium alloy components however, especially aerospace components, are still manufactured by the conventional machining methods, such as turning, milling, drilling, reaming, tapping, sawing, and grinding [65]. Gas turbine engines for example, incorporate turning and drilling as their main machining operations, with airframe production using end milling and drilling as the major operations [6]. These machining methods, including turning, are expensive when used on titanium alloys. This is mainly due to the machinability of the alloys.

Machinability can be described as the ease, or difficulty, at which a material can be cut, or machined, to a desired shape, surface finish, and tolerance with respect to the machining process used. Machinability can be measured by analysing different areas during a machining operation. These areas include tool life achieved, metal removal rate, component forces, power consumption, surface finish generated, surface integrity of the machined component, and chip shape and size. A number of different factors however, can significantly affect the machinability index. These factors include the properties of the material to be machined, the properties and geometry of the cutting tool used for machining, the cutting conditions used, and other miscellaneous factors as presented in Table 2.6 and Table 2.7. The machining productivity can be improved by achieving the right combination of cutting tools and cutting conditions. This allows for high speed machining to be achieved without

compromising the machined component. These conditions are required when machining difficult-to-cut alloys, such as titanium alloys, with properties that impair machinability [5].

Table 2.6 - Factors affecting machinability [66]

Factors indirectly affecting machinability		
Work material and tool material	Cutting conditions	Cutting tool part fixture
Mechanical properties Microstructure Physical properties Chemical properties Composition Inclusions Heat treatment Tool grain size Tool surface finish Tool coating	Cutting speed Depth of cut Feed rate Atmosphere Cutting liquid and cooling	Type of operation Vibration Rigidity Work piece holding device Power Tool geometry tool dullness
Factors directly affecting machinability		
Cutting mechanisms	Cutting forces	Cutting temperature

Table 2.7 - Machinability measurement parameters

Tool life	**Efficiency of chip removal**	**Workpiece quality**
Crater wear Flank wear Notch wear	Power required Cutting forces Chip form	Surface finish Surface integrity Dimensional accuracy

Titanium alloys are considered difficult to machine due to their physical properties. One property that hinders the machinability is a strong alloying tendency or chemical reactivity with most tool materials. This causes chipping,

rapid cutting tool destruction, welding and smearing at the interacting surface [10,12,67]. Ti-6Al-4V also has a low thermal conductivity which increases the temperature at the interface between the tool and workpiece. This in turn affects the tool life considerably [6,11,12,68,69]. Other properties which also affect the machinability include high strength at elevated temperatures, low modulus of elasticity, and resistance to wear and chemical degradation [5,12,70].

The energy that is consumed during a typical turning operation is mostly converted into heat. This heat generation is the cause of most machining problems and occurs mainly during the deformation process. During this process, large amounts of friction occur at the tool-chip and tool-workpiece interfaces. The heat generation is more intense when machining titanium as more energy is required to cut the material [5]. To decrease the amount of problems associated with the machining of titanium alloys and improve the poor machinability thereof, certain principle problems need to be overcome. These principle problems are related to the material's natural properties. They include high cutting temperatures, high cutting forces, chatter, and strong chemical reactivity [6]. For the purpose of this investigation, the cutting temperatures and cutting forces are monitored during the machining to aid in inconsistency detection.

2.5.1 High cutting temperatures

As previously discussed, high cutting temperatures are created whilst machining titanium alloys. These high temperatures occur close to the tool's cutting edge. This is one of the principle reasons for rapid tool wear that is experienced. Figure 2.9 clearly shows that approximately 70 - 80% of the heat generated during machining of titanium alloys is conducted by the tool [6]. When compared to AISI 1045, only about 40 - 50% is conducted by the tool. This higher percentage occurs for titanium alloys due its low thermal conductivity and high chip flow rate. The chip therefore cannot conduct the

heat as quickly as the tool, resulting in less heat absorbed by the chip [6,71]. Investigations have shown that the temperature gradients during titanium alloy machining are much steeper than other materials. The heat-affected zones are also much smaller and closer to the cutting edge. This is due to the produced chips and flow zone between the chip and tool being very thin. This high tool-tip temperature can reach values of about 1100°C [72-76]. The cutting temperatures measured during this investigation however, do not reach the high values as discussed in this section as they are measured at a point on the cutting tool, away from the cutting edge. They are monitored to detect any irregularities.

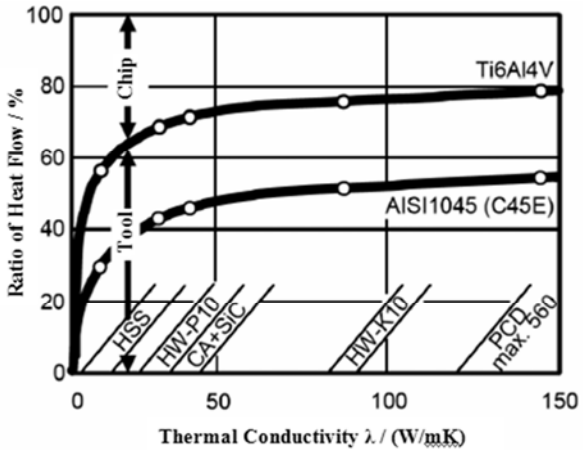

Figure 2.9 - Thermal load distribution when machining Ti-6Al-4V and AISI 1045 [6]

2.5.2 High cutting forces

The cutting forces achieved when machining titanium alloys are similar to those achieved when machining steels [77]. The power consumption during machining is therefore also approximately the same [78]. The production of high mechanical stresses near the cutting tool edge however, creates problems for the machining of titanium alloys. Konig [79] reported that the tool stresses when machining titanium alloys are higher than those achieved when machining nickel-based alloys, and approximately three to four times that of steel. This is summarised in Figure 2.10. These stresses may be attributed to

the small chip-tool contact area on the rake face for titanium. The contact area when machining titanium alloys is about one-third that for steel machined at the same feed rate and depth of cut [80]. The stresses are also attributed to titanium alloy's resistance to deformation at high temperatures, which begin to reduce above 800°C [79,81].

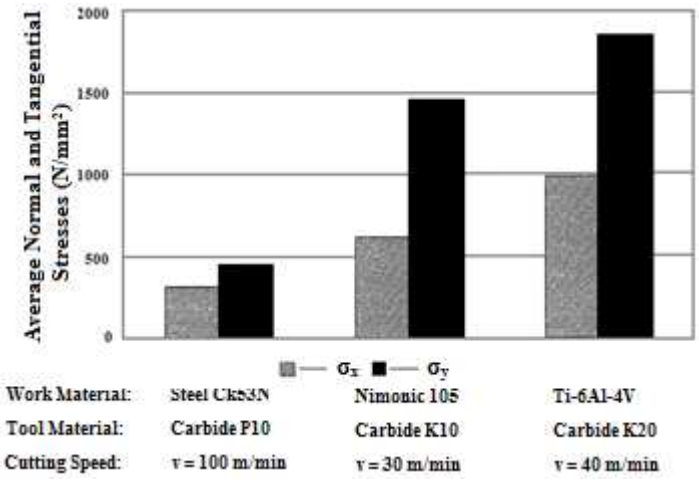

Figure 2.10 - Normal and tangential stresses in machining [79]

2.5.3 Chatter

Chatter is a common problem which occurs when machining of titanium alloys, specifically when it comes to the surface finish required. The principle cause of chatter comes from the low modulus of elasticity of titanium alloys. The material deflects almost double that of carbon steel when subjected to cutting pressures during machining. This greater spring-back behind the cutting edge is responsible for premature flank wear, vibrations, and higher cutting temperatures [81]. The effect which occurs can be described as a bouncing action at the point where the cutting edge enters the cut. The chatter may also be partly due to the high dynamic cutting forces which occur during the machining of titanium alloys. They can reach up to about 30% that of the static forces [79]. This is attributed to the 'adiabatic or catastrophic thermoplastic shear' process by which the titanium chips are created [82-87].

2.5.4 Cutting tools

Cutting tools often experience extreme thermal and mechanical stresses close to the cutting edge during the machining of difficult-to-cut alloys such as nickel-base and titanium alloys with poor machinability. This is due to the mechanical and chemical properties of the materials [58]. These stresses usually lead to plastic deformation, along with accelerated tool wear. A major requirement for these cutting tools is therefore the ability to withstand elevated temperatures during high cutting speeds and possess a sufficient hot hardness. The majority of cutting tools tend to lose their hardness when subjected to elevated temperatures. This results in the weakening of the inter-particle bonds of the tool and leads to accelerated tool wear [5]. Flank wear is another major factor that diminishes tool-life for a range of cutting conditions.

Advancements in cutting tool development have been achieved over the past couple of decades. These developments include coated carbides, ceramics, cubic boron nitride and polycrystalline diamond cutting tools. They have been tested and used particularly in the machining of cast irons, steels and nickel-based alloys. None of these newer developments however have had success in improving the machinability of titanium alloys. This is attributed to the principal qualities that are required by tool materials when machining titanium alloys. These qualities include [6]:

- High hot hardness to resist the high stresses involved
- Good thermal conductivity to minimise thermal gradients and thermal shock
- Good chemical inertness to reduce the tendency to react with titanium alloys
- Toughness and fatigue resistance to withstand the chip segmentation process
- High compressive, tensile and shear strength

Straight tungsten carbide cutting tools have been found to be beneficial in most cases when machining titanium alloys. Recent studies have also shown that straight cobolt-base tungsten carbide tools, implanted with chlorine or indium, are also effective in machining titanium alloys [88]. Another study proved that steel cutting Grades of cemented carbides are not suitable for machining titanium alloys. This is due to their greater wear rates that occurred and thermal properties [72,74,79,89]. General-purpose high speed steel tools have also been found to be suitable for titanium alloy machining, but the highly alloyed Grades have given the best results [78,90]. Ceramic tools however, have improved in quality and are being used more often, but are yet to replace the cemented carbides or high speed steels. This is mainly due to most ceramics being fairly reactive with titanium and having a poor thermal conductivity and low fracture toughness [91]. Superhard cutting tool materials such as cubic boron nitride and polycrystalline diamond also display good wear rates when machining titanium alloys [72,92], but are often not used due to their high price.

2.5.5 Additional challenges

Along with the problems previously described in this section, other problems also exist. The strong chemical reactivity of titanium alloys also causes damage to the cutting tools. The chemical reactivity causes the material to react chemically with almost all tool materials that are available for cutting temperatures exceeding 500°C. All the problems mentioned in this section can be minimised by the utilisation of rigid machines, proper cutting tools, large amounts of coolant, non-conventional cutting methods, minimising cutting pressures, and designing special tools [6].

2.6 High performance machining

In 1980, High Performance Machining (HPM) would refer to the machining of materials by applying large feed rates and cutting depths whilst simultaneously maintaining high cutting speeds. The process would be carried out on machines that had very powerful and rigid headstocks to maintain high precision. This traditional machining process is also known as 'high removal rate machining'. Relatively large chips would be formed as illustrated in Figure 2.11. Problems such as possible catastrophic tool failure due to the high cutting forces or edge breakages at multiple points did however occur with this method of machining. Due to these problems, only soft materials such as lightweight alloys, low resistance steels or steels prior to hardening through tempering could be machined [93]. In today's context, HPM refers to the improvement of two aspects of the machining process, namely productivity and quality. The productivity is the measure of the material removal rate. In other words, it is the amount of material that is removed in a unit of time. The quality is the accuracy and precision of the dimensional cut and surface finish achievable. Therefore, HPM is the machining of materials by incorporating high speed machining as well as high precision machining. As high speed machining is conducted in this investigation, it is briefly described in the following section.

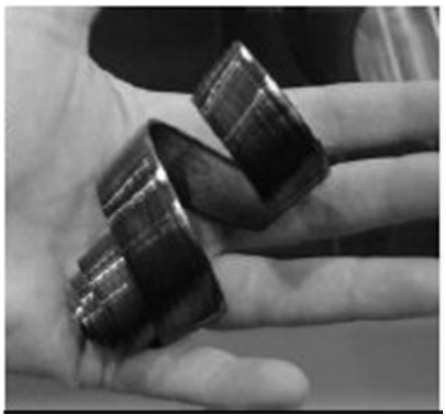

Figure 2.11 - Large chip created in high removal rate machining [93]

2.6.1 High speed machining

High Speed Machining (HSM) was first defined by C. Salomon in 1931. He found that cutting temperatures started decreasing above a certain cutting speed (see Figure 2.12). According to Salomon, the temperature for titanium alloys started decreasing at a cutting speed of approximately 250 m/min. Salomon also determined that for a certain range of cutting speeds, machining was not possible. In this range, the temperatures are too high for machining. Therefore, HSM only takes place after this region. It was also noted that HSM included any type of machining where cutting speeds exceeded the conventional cutting speeds by a factor of 5 to 10 for that process. Salomon's theory and findings were only verified and improved upon in later years when a better understanding of HSM was achieved. HSM is therefore defined by not only high cutting speeds, but also other machining parameters with higher values than those of the conventional machining values. These machining parameters, other than cutting speed, include rotational speed, feed rate and depth of cut. In this investigation, conventional cutting speeds of the titanium alloys are considered to be in the range of 30 - 100 m/min with the use of sintered carbide tools. According to Moriwaki's findings [94], it is suggested that the cutting speeds required for the HSM of titanium alloys are to be in the range of 100 m/min to 1000 m/min as illustrated in Figure 2.13. The comparison of HSM to conventional cutting speed machining is also presented in Table 2.8 [95-99]. For this study, the cutting speeds range from 70 m/min to 300 m/min for the grade 4 titanium alloys and 70 m/min to 200 m/min for the grade 5 titanium alloys.

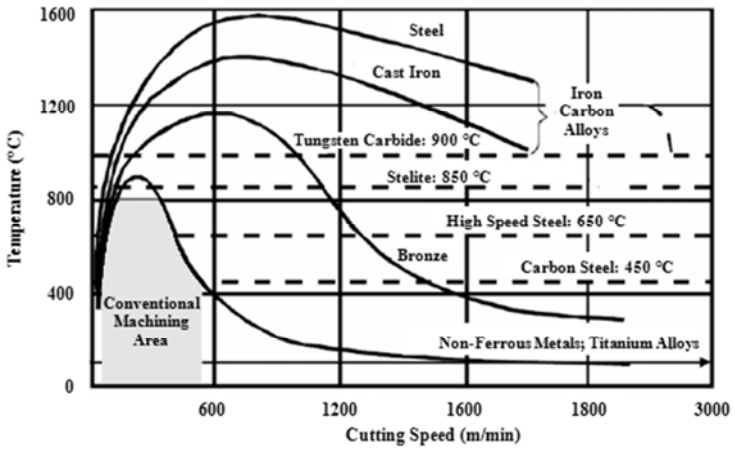

Figure 2.12 - Temperature as a function of cutting speed for different materials [99]

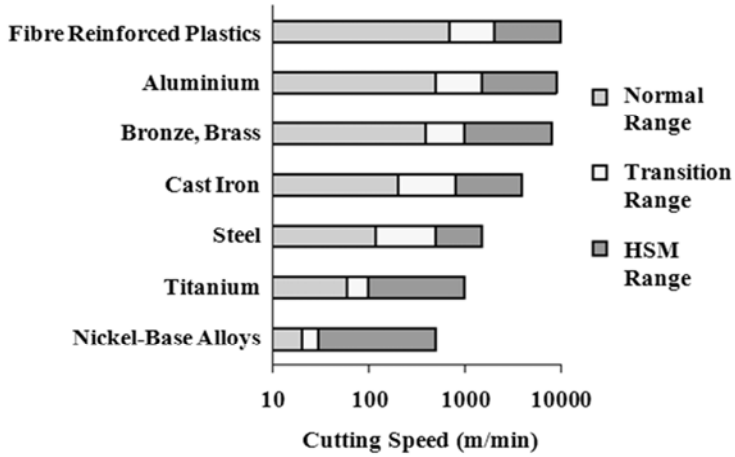

Figure 2.13 - Conventional, transition and HSM speeds for given materials [94,98]

Table 2.8 - Cutting speed comparison for HSM and conventional machining [99]

Work material		Solid tools WC, Coated WC, PCD, Ceramic		Indexable tools WC, Ceramics, Sialon, CBN, PCD	
		Typical cutting speed (m/min)	High cutting speed (m/min)	Typical cutting speed (m/min)	High cutting speed (m/min)
Aluminium		>305 (WC, PCD)	>3050 (WC, PCD)	>610	>3658 (WC, PCD)
Cast iron	**Soft**	152	366	366	1219 (Sialon, Ceramic)
	Ductile	107	244	244	914 (Ceramic)
Steel	**Free mach. steel**	107	366	366	610
	Alloy	76	244	213	366
	Stainless	107	152	152	274
	Hardness HRC 65	24	122	30(WC), 91(CBN, Ceramic)	46(WC), 183(CBN, Ceramic)
Titanium alloys		38	61	46	
Super alloys		46	76	84(WC), 213(CBN, Ceramic)	366 (Sialon, Ceramic)

HSM can be used with a number of different machining processes, for instance grinding, milling and turning. HSM does offer possible advantages in some cases. These may include productivity improvement, increased material removal rate, increased surface finish quality, increased dimensional accuracy and part quality, better machining tool utilisation leading to a reduction in machining costs, lower cutting forces, and fewer burrs [98]. There may however also be significant disadvantages associated with HSM. These include excessive tool wear, specialised and expensive machining tools, advanced machining tool materials and coatings, as well as the problem of having to balance the tool holder. The cutting speed used is constrained by the amount of heat that needs to be removed from the tool-workpiece interface [98]. The mean tool temperature on the rake face can be estimated by using the following function [100]:

$$T_{rake} = u\sqrt{\frac{Vf}{(k\rho C)}} \quad \text{……..(1)}$$

u is the specific cutting energy, V is the cutting speed, f is the feed rate, k is the thermal conductivity, ρ is the density, and C is the specific heat. The factor $k\rho C$ for titanium, is very small when compared with steel or aluminium, and leads to rapid temperature rises at low cutting speeds and feed rates [100]. This temperature rise can cause problems in the titanium alloy during machining. The cutting tool temperature is therefore monitored during machining to aid in the detection of irregularities and in turn additional, secondary residual stresses.

2.7 Residual stresses

Residual stresses are stresses that are locked in a structure or component, even when the part contains no external loads [101]. They are the stresses caused by incompatible permanent strains [102]. In other words, residual stresses are formed due to some property altering process, i.e. thermal, mechanical, or metallurgical. They then remain in the material even after the process has occurred. The stresses can also be described as self-equilibrating stresses which exist in a body with no external forces [103]. The internal stresses are therefore balanced, i.e. the tensile residual stresses in the component are counter balanced by the compressive residual stresses [104].

These residual stresses influence the component's characteristics. They can have a significant effect on the performance of an engineering component [16,105]. They can also directly influence the deformation, dynamic and static strength, and the chemical and electrical properties of a component [106]. The residual stress effects are dependent on the magnitude, sign and distribution of the stresses. Residual stress may be beneficial or detrimental to a component's mechanical performance [107]. Tensile residual stresses tend to be detrimental

because they may substantially reduce the fatigue life of components subject to dynamic loading [108]. Residual stresses are generally detrimental when their magnitude is in the range of the material's yield strength. It is beneficial to decrease these stresses. Compressive residual stresses on the other hand tend to be beneficial as they may enhance the fatigue life and performance of a component subject to dynamic loading.

Stresses from loading and residual stresses can be superimposed and result in much larger effects on structural components. There has been an ever increasing interest in residual stress effects on the mechanical properties of components due to their influence on structural failure [15]. An evaluation of these stresses provides a means for process control, quality control, design assessment and failure analysis [16].

In certain cases, the presence of residual stresses can be visible to the naked eye. Visibly deformed or distorted components may be a clear sign of the presence of residual stresses. This distortion can in some cases be useful in predicting the presence and/or sense of direction of the residual stresses. Thermal residual stresses generally cause visible distortions. These stresses are largely due to differential expansion, resulting from the heating and cooling of a metal [104].

More often than not, residual stresses have a negative influence on the performance and structural integrity of the component. This however is not always the case. They can, in some cases, play an important role in the prevention of component failure. An example of this is the shot peening surface treatment of a component. Shot peening causes compressive stresses to be induced in the surface of a component. This enhances the fatigue life of that component. The induced compressive residual stresses therefore decrease the fatigue crack growth rate of the component and increase its fatigue life [107].

Residual stresses can in many cases be reduced by certain methods or processes. The residual stresses in weld joints for example, can be reduced by heat treatment [109-111] or mechanical stress relieving [112]. Resonant vibration methods reduce the residual stresses in the weld by vibrating the component and weld joint at a certain frequency [113].

Pawade *et al.* [114], found that in order to achieve components with greater reliability and longevity, strict control on the quality of the machined surface and sub-surface during high speed machining of super-alloys was necessary. Analysis of the residual stresses, microhardness measurements and degree of work hardening in the machined sub-surfaces were used to create optimal machining conditions that resulted in machined surfaces with high integrity [114]. It was observed that by using machining parameters of the highest cutting speed, lowest feedrate, and a moderate depth of cut would induce desired compressive residual stresses in the machined surfaces, producing a longer fatigue life. Observations from Pawade *et al.* revealed that the residual stresses increased in the tensile direction with an increase in cutting speed from 125 m/min to 300 m/min. A further increase from 300 m/min to 475 m/min however, caused the residual stresses to change direction to compressive. Also, with an increase in depth of cut from 0.50 mm to 0.75 mm the residual stresses changed from tensile to compressive, and with a further increase to 1.00 mm, became even more compressive [114].

Ulutan and Ozel [21], presented an overview of machining induced surface integrity in titanium and nickel alloys. Residual stresses and surface alterations induced by the machining of these materials were found to be important due to safety and sustainability concerns. The paper also added that there are many important parameters that affect the surface quality of components. These included the cutting speed, feed rate, depth of cut, tool geometry and preparation, tool wear, and workpiece properties [21]. Observations that were achieved in the investigation showed that the residual stresses increased in compression with an increase in cutting speed until reaching a maximum

compressive stress of approximately 350 MPa at a cutting speed of around 80 m/min. A further increase in cutting speed caused the stresses to become more tensile (see Figure 2.14).

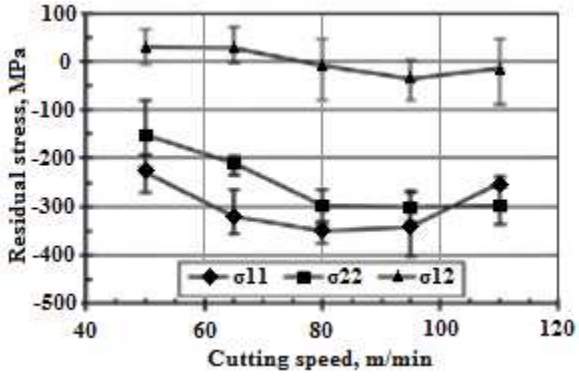

Figure 2.14 - Residual stress changes with cutting speed in end milling of Ti-6Al-4V with coated carbide tools at 1.5 mm DOC [115]

Puerta Velasquez *et al.* [17], summarised an extensive experimental study of the surface integrity and sub-surface microstructure of Ti-6Al-4V during high speed machining in orthogonal cutting conditions. The results revealed that residual stresses were compressive at low cutting speeds and tensile at high cutting speeds. A change from compressive to tensile was also found to occur at a specific machining speed of approximately 100 m/min. At this point the residual stresses were close to zero. These results are presented in Figure 2.15.

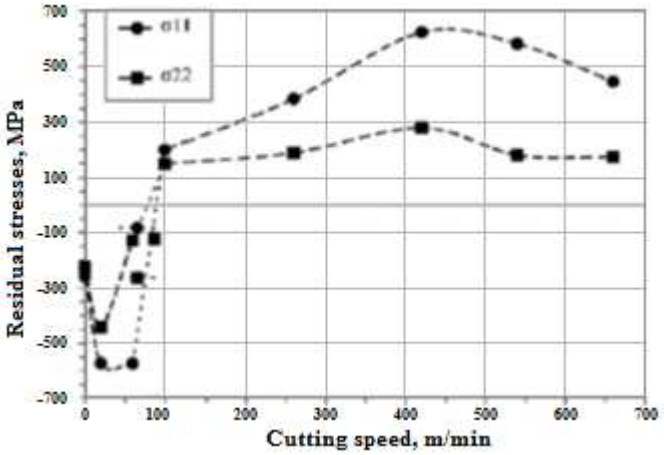

Figure 2.15 - Residual stresses as a function of cutting speed for Ti-6Al-4V [17]

Mantle and Aspinwall [116], also found that the residual stresses were generally compressive at low cutting speeds and tended towards tensile stresses with an increase in cutting speed. They also provided a graph illustrating the effects that different machining parameters had on the residual stresses induced in the material (see Figure 2.16).

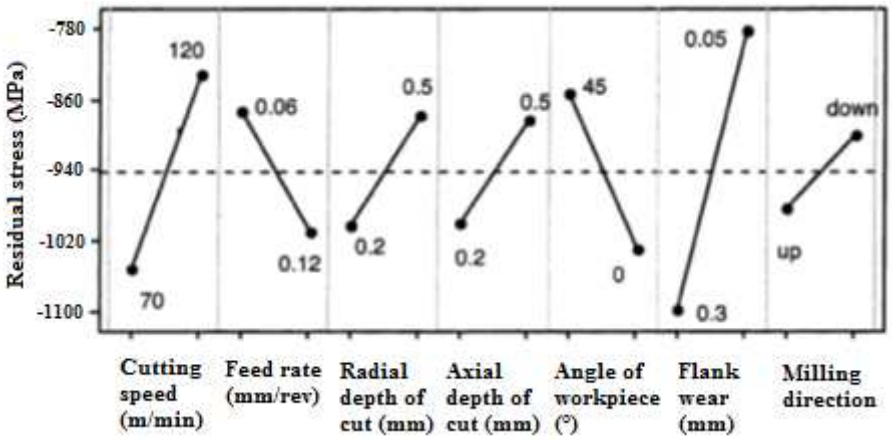

Figure 2.16 - Effects of machining parameters on residual stresses in high speed machining of Ti-45Al-2Nb-2Mn-0.8% [116]

It may be concluded that residual stresses can be either detrimental or beneficial, such that when in tension they are detrimental, and when in compression, beneficial. Certain mechanical methods alter the amount of stresses present in a component, inducing either tensile or compressive stresses. Although some sources of residual stresses are briefly mentioned in this section, they are further discussed in the following sections.

2.7.1 Sources of residual stresses

The majority of all structural components contain residual stresses. This can be due to a number of factors, operations, or processes. The main cause is due to local plastic deformation from thermal or mechanical operations. These thermal and mechanical processes take place during the manufacturing stage of a structural component [104,107]. Almost all manufacturing processes,

including welding, heat treatment, rolling, forging, casting, machining, straightening, flame cutting, plastic deformation during bending, or moulding, create residual stresses in components [104,117]. The following sections give a brief overview of the three main groups of induced residual stresses. These groups include metallurgically, thermally, and mechanically induced residual stresses.

2.7.1.1 Metallurgically induced residual stresses

Metallurgically induced residual stresses are formed by phase changes and localised volume changes in a metal. An increase in volume of a metal may cause compressive stresses to be formed. As an example, after heating steels to a temperature of typically 900°C, a phase change occurs from ferrite-pearlite to martensite when quenched. This change causes a 3 - 4% increase in volume of the metal and therefore causes residual stresses [118].

2.7.1.2 Thermally induced residual stresses

Thermally induced residual stresses are caused when a material is subjected to a temperature altering process, after which it is cooled down back to the ambient temperature. As the material cools, it undergoes uneven cooling rates, which in turn cause tensile and compressive stresses in the material. For thermal residual stresses to be induced in a component, two factors need to be present. These factors include thermal treatment and restraint. Thermal treatment is the heating or cooling of the material. Both these factors control the generation of thermal residual stresses [104]. There are many processes which can potentially induce thermal residual stresses. To name a few, these include hot-rolling, heat treatment, flame cutting, or welding. These processes each involve some sort of heating or cooling which results in the induction of thermal residual stresses.

2.7.1.3 Mechanically induced residual stresses

Mechanically induced residual stresses are the result of restrained deformations. This occurs when a material is deformed in some way, by either stretching or compressing it, and is then prevented from returning to its equilibrium position. This prevention causes restrained forces to occur within the material and therefore result in residual stresses. Examples include mechanical straightening and mechanical bending [118].

2.7.1.4 Machining induced residual stresses

Machining induced residual stresses are induced into a material during component machining. These stresses are a combination of thermally induced residual stresses and mechanically induced residual stresses as both heating and deformation occur during machining. The high temperatures generated near the tool-workpiece interface cause the thermally induced residual stresses. The material removal method that deforms the component causes the mechanically induced residual stresses.

2.7.2 Measurement of residual stresses

Along with the importance of safety increasing over the last couple of decades, so too has the urgency or need to accurately measure residual stresses. Residual stress measurement however is not a simple task. The techniques used still require a great deal of refining. Analytical predictions are available, but only serve as an approximation method and not as accurate data.

Various techniques are used to assess residual stress levels [119-122]. Examples include the layer removal/bending method, sectioning method, hole-drilling method, indentation method, contour method, crack compliance

method, diffraction methods, electromagnetic methods, piezo-spectroscopic methods, ultrasonic methods, thermo-mechanic methods or photo-elastic methods. These methods can be divided into three major groups. These are destructive, non-destructive, and semi-destructive measurement techniques. The destructive techniques involve methods which cause damage/destruction to the material's equilibrium stress state and render the component unusable thereafter. They can be mechanical, chemical, or thermal. The non-destructive techniques however do not damage the material at all. They use the material's properties in connection with its current stress state to determine the residual stresses. The properties used can be either physical or crystalline. The semi-destructive techniques use methods similar to the destructive techniques, however only generate a small amount of damage on the component [123]. In the following subsections, a few residual stress measurement techniques are discussed. Focus is placed on X-ray diffraction, which is the technique used in this investigation.

2.7.2.1 Hole-drilling

The hole-drilling technique has been around for over 70 years and was first described by Mather in 1934 [124]. As would be expected from a technique which has been around for so long, there are many different approaches to hole-drilling. These approaches include different drilling techniques, different calibration routines, and different analysis tools [125]. Hole-drilling however, is one of the most widely used methods for measuring residual stresses today [126].

The basic principle behind the hole-drilling method lies in the drilling of a small hole in the surface of a material. This hole therefore allows stress relaxation to occur and the strain around the hole is then measured. The strain is measured with the aid of triple strain gauge rosettes. Residual stresses are then calculated from these strains measured. The typical setup of the hole drilling technique with the addition of the triple strain gauge rosettes is

illustrated in Figure 2.17. The positioning of the strain gauges is critical for the measurement of released strains.

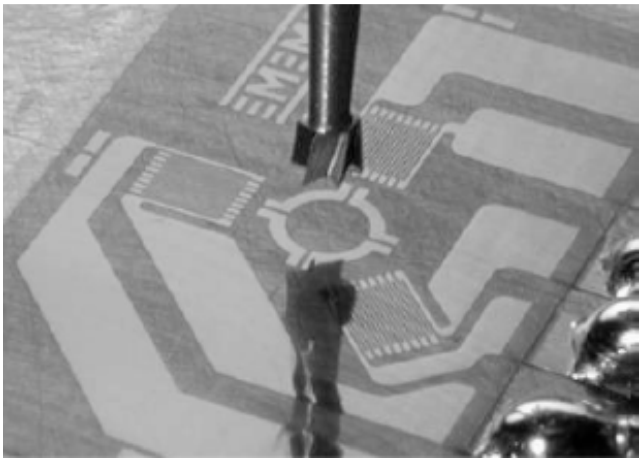

Figure 2.17 - A typical strain gauge rosette as used in the hole-drilling technique for residual stress analysis [127]

The strain relaxations, measured from the strain gauge rosettes (ε_1, ε_2, ε_3), allow for calculation of the in-plane stresses which were present in the material prior to drilling. This is achieved by using (Equation 2), where $\bar{a}$ and $\bar{b}$ have previously been geometrically determined for different setups [128].

$$\sigma_{max}, \sigma_{min} = -\frac{E}{2}\left(\frac{\varepsilon_3+\varepsilon_1}{(1+\upsilon)\bar{a}} \mp \frac{\sqrt{(\varepsilon_3-\varepsilon_1)^2+(\varepsilon_3+\varepsilon_1-2\varepsilon_2)^2}}{\bar{b}}\right) \quad \text{(2)}$$

This approach however, is only used when the stress field is uniform in depth, which is often not the case. In cases where it is not uniform, there are separate calculations available. Such cases use incrementally drilled holes with strain measurements taken at each depth [128].

2.7.2.2 Digital image correlation

Digital Image Correlation (DIC) is a full non-contact strain measurement technique. Its use in residual stress determination has increased significantly in

recent years. DIC works by comparing images of a test piece or component at separate stages during deformation and tracking blocks of pixels to measure the surface displacement [129]. A CCD camera is used to record the deformation. A digital image correlation process then determines the shift and/or rotation and distortion of the small facet elements. An accuracy of up to 1/100 of a pixel in displacement can be achieved with such algorithms [130].

When three-dimensional measurement is required, two cameras in different positions are used. With the object observed from two different angles, the position of each object point is focused on a single specific pixel. The three-dimensional coordinates of any surface point can be calculated by knowing the positions of the two cameras relative to each other, as well as the magnifications and imaging parameters. Calculating this for every point on the object's surface therefore gives a three-dimensional surface contour of the object. It is however important that the surface of the object being viewed displays sufficient structure in order for the algorithms to correlate identical points from both cameras. The principle behind three-dimensional correlation with two cameras is illustrated in Figure 2.18 [130,131].

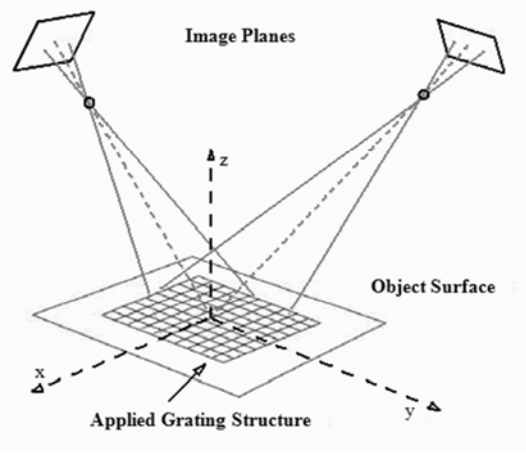

Figure 2.18 - Principle of 3D image correlation with 2 cameras for digital residual stress determination [130]

2.7.2.3 X-ray diffraction

All metals consist of atoms arranged in such a way that they form regular three-dimensional crystals. These atoms then randomly orientate themselves as tiny crystallites within the crystalline arrangement to form a bulk solid. When stress is introduced into such a metal, elastic strains are formed within the crystal lattice [132]. In other words, when a stress is applied to the material, it is taken up by interatomic strain, as long as it is below the material's yield strength. The technique of X-Ray Diffraction (XRD) then uses X-rays to penetrate the material and diffract off these layers of crystallites. The interatomic spacings caused by elastic strain in a material are then measured. With the original stress-free spacing and these altered spacings measured, the total stress on the metal can then be inferred. This is achieved by first calculating the elastic strain through using relations involving the wavelength, change in Bragg angle and the measured inter-planar spacings [133]. From the strain, and knowing the elastic constants of the material, the stress values can then be found. This is based on the assumption that stress is proportional to strain [132].

The method of XRD used in this investigation determines the strain in a material by comparing peak positions identified in the material's composition. Each stress free material has its own unique diffraction pattern which is identified by XRD over a 2θ scale. An example of a diffraction pattern scan for Ti-6Al-4V is illustrated in Figure 2.19. With the introduction of residual stresses causing the interatomic spacings of the material to change, the diffraction pattern for the material is therefore also shifted. It is this change in peak positions of the pattern scan which is used to eventually determine the residual stresses.

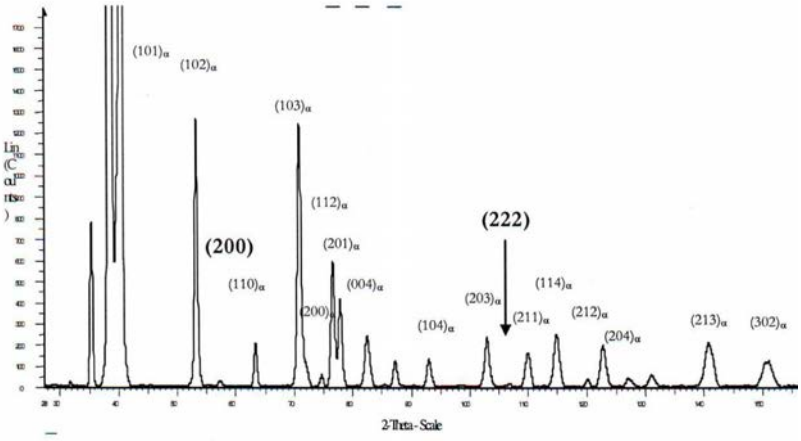

Figure 2.19 - Typical diffractogram for Ti-6Al-4V obtained with CuKα-radiation [134]

By superimposing the pattern scan of a stress induced material over the pattern scan of the stress free material, the change in peak positions can then be measured. With this measured change, and the use of (Equation 3) and (Equation 4), the resulting strain can then be determined.

$$\lambda = 2d_{hkl}\sin\theta \quad \text{.....(3)}$$

$$\varepsilon_{hkl} = \frac{d_{hkl} - d_0}{d_0} = -\cot\theta\Delta\theta \quad \text{.....(4)}$$

In (Equation 3), λ is the incident wavelength, d_{hkl} is the lattice spacing, and θ is the diffraction angle. For (Equation 4), ε_{hkl} is the elastic strain and d_0 is the stress-free lattice spacing measured using a texture-free sample containing no stresses. Once the strain is achieved, it is used to determine the full stress tensor. The principle stresses σ_1, σ_2 and σ_3, are finally found from this full stress tensor. The maximum principle stress, (Equation 5), minimum principle stress, (Equation 6), and Von Mises stress, (Equation 7) can then also be determined.

$$\sigma_{Max} = Max(\sigma_1, \sigma_2, \sigma_3) \quad \text{.....(5)}$$

$$\sigma_{Min} = Min(\sigma_1, \sigma_2, \sigma_3) \quad \text{.....(6)}$$

$$Mises = \sqrt{\frac{1}{2}\left[(\sigma_1 - \sigma_2)^2 + (\sigma_2 - \sigma_3)^2 + (\sigma_3 - \sigma_1)^2\right]} \quad \text{.....(7)}$$

XRD is used for residual stress measurement in this investigation due to it being non-destructive and its ability to penetrate titanium. Hole-drilling cannot be used because fundamentally the stress caused by machining is not uniform in depth. It only occurs within the first ±200 µm. The residual stresses on the Grade 4 and 5 samples are measured by the x-ray diffractometer situated at NECSA (Nuclear Energy Corporation of South Africa).

2.7.2.4 Synchrotron diffraction

Synchrotron radiation diffraction is simply a specialised X-ray diffraction technique. It uses intense beams of high energy electromagnetic waves of x-rays to achieve a greater penetration depth into a material. An average depth of 1 - 2 mm is generally achieved in most materials. This higher penetration depth gives this method the capability of providing high spatial resolution with three-dimensional mapping of strains in components. The spatial resolution however, is only limited by the size of the crystallite within the sample and not the instrument itself. The depth of penetration achieved by the beam, and the intense narrow beam size of 1 - 10 mm, are advantages of synchrotron diffraction. The measurements are also taken within fractions of a second, which is quicker than X-ray diffraction. This allows for more measurements to be taken in a shorter time interval. It also allows for detailed strain maps of components to be constructed within only a few hours of beam time [133].

2.8 Microstructural analysis

Microstructural analysis is a technique used to investigate the microstructure of materials. It ranges from simple determination methods of material parameters such as grain size, structure and orientation, to a full analysis of component degradation or failure mechanisms [135]. The microstructural analysis in this investigation however, only required the examination of the microstructure at the machined surface of the titanium alloy grades. The effect that the machining had on the grain size, structure, and orientation was therefore examined. To analyse this microstructure, an optical microscope and Scanning Electron Microscope (SEM) were used. These are presented in more detail in the following subsections.

2.8.1 Optical microscope

The optical microscope, in its simplest form, is used to magnify small images. It is considered one of the simplest and cheapest methods for microstructural analysis. It operates by using natural light and a system of lenses and mirrors to enlarge images of small samples. The optical microscope is often called the “light microscope” due to its operation. Most optical microscopes are simple and basic, however there are more complex designs available. These more complex designs are used to improve image quality by improving resolution and sample contrast [136]. Optical microscopes which include CCD cameras to examine samples are more commonly known as digital microscopes. They display the magnified image on a computer screen eliminating the need for eye-pieces. An example of an optical microscope, with an attached camera, similar to the one used in this investigation is presented in Figure 2.20.

Figure 2.20 - Example of an optical microscope [137]

2.8.2 Scanning electron microscope

A Scanning Electron Microscope (SEM) is a microscope that magnifies the image of a surface by utilising the wave and particle properties of electrons. It is commonly used to obtain the external morphology, chemical composition, crystalline structure and surface microstructure of a component. The microscope uses a focused beam of high energy electrons, incident on the test specimen, to generate the required output signals [138]. These output signals are achieved by the kinetic energy dissipation of the accelerated electrons upon collision with the specimen's solid surface and are characterised by their corresponding sources. These sources comprise of secondary electrons, backscattered and diffracted backscattered electrons, photons, visible light and heat. During the production of SEM images however, only the secondary electrons and backscattered electrons are used [138]. The built-in detectors in the SEM then analyse these output signals and produce digital images of the specimen surface at magnifications from 20X to approximately 30000X. A functional schematic of the SEM is illustrated in Figure 2.21.

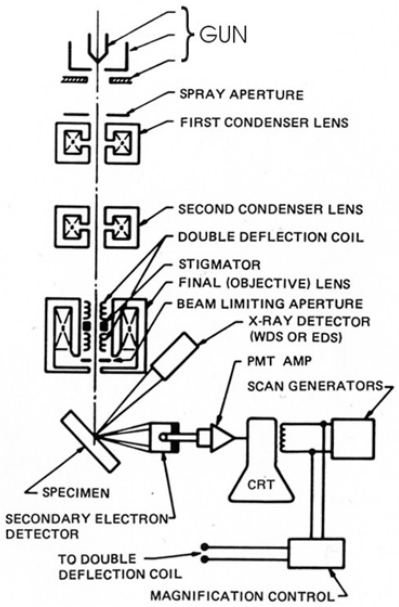

Figure 2.21 - SEM functional schematic [138]

Puerta Velasquez *et al.* [17] analysed the deformation depths generated by machining Ti-6Al-4V along with the residual stresses. Results show a general increase in deformation depth with an increase in cutting speed. A deformation depth of approximately 5 µm is observed for the cutting speed of 20 m/min, which increases to almost 35 µm for 420 m/min.

This chapter therefore presents the relevant literature concerning the entire investigation. All aspects of machining induced residual stresses on Grade 4 and 5 are covered. Research regarding titanium, its alloys and properties is first discussed before information on material characterisation, including compression and microhardness testing is provided. The machining of materials, specifically machining methods and machinability of titanium alloys is then presented. High performance machining, residual stresses and residual stress measurement techniques, including hole-drilling, digital image correlation, synchrotron diffraction and X-ray diffraction are then discussed. The final stage of the chapter introduces microstructural analysis, with details of optical microscopy and SEM techniques.

Chapter 3. Experimental Program

Chapter 2 presented a literature review as applicable to the current investigation. In this chapter, the experimental method and apparatus used for each testing stage during the experimental program are presented and discussed. These stages include mechanical property evaluation in the shape of microhardness and compression testing, machining, residual stress analysis, and microstructural analysis by optical microscopy and scanning electron microscopy analysis. Sample preparation was also completed prior to testing.

3.1 Mechanical property evaluation

3.1.1 Sample preparation

The samples required for mechanical property evaluation required several steps of preparation before testing could commence. The steps included the cutting, mounting, grinding and polishing of the materials. These steps are presented in the current section.

Cutting

The samples were cut from the un-machined part of the Grade 4 and 5 billets. Two disks of 3 mm thickness were cut by wire-EDM for each grade. The disks were then cut into 10 mm by 10 mm square samples and 65 mm by 16 mm rectangular samples. The square samples were used in the microhardness tests and the rectangular samples in the compression tests. The cutting plan for this disk is illustrated in Figure 3.1.

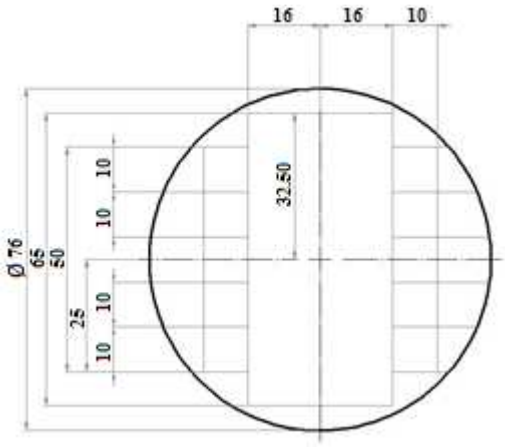

Figure 3.1 - Mechanical property evaluation sample cutting dimensions

The square specimens then went through a further three step process of mounting, grinding and polishing. This process produced a better surface finish with enhanced results. The rectangular samples however, did not require further sample preparation, but rather strain gauge mounting. This is briefly described in the compression testing section.

Mounting

The first step involved mounting the samples in a hot polyfast resin. The polyfast resin includes carbon filler which creates a better edge retention on the samples. The mounting process was done using a LECO mount press as illustrated in Figure 3.2. Care was taken to achieve a uniform sample mount height. This ensured an even force application on the samples during grinding and polishing. Before mounting the samples, the process selector switch (as identified in Figure 3.2) was turned to “heat” to preheat the chamber. The surface under examination was placed face down on the mounting piston, and lowered into the chamber by releasing the ram down valve. Once completely lowered, the ram down valve was closed again. Approximately 25 ml of polyfast resin was then poured into the chamber covering the sample. The removable ram was screwed into place over the chamber, and the ram control selector turned to “up”. This raised the lowered piston and pressurised the resin by compressing it between the two rams. Under the pressure and heat,

the resin melted and formed a thermoplastic mould around the sample. This pressurising step was done for approximately 8 minutes. The mould was then water cooled by turning the process selector switch to “cool”. This solidified the thermoplastic and produced the working mould after a further 8 minutes.

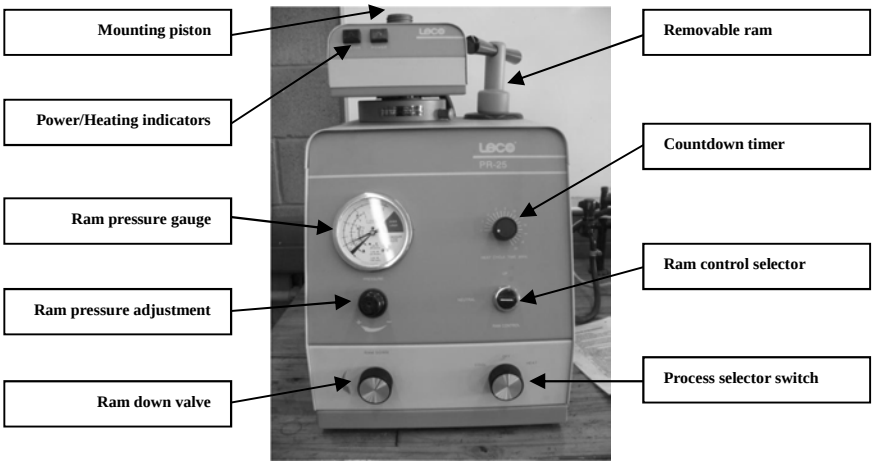

Figure 3.2 - LECO mounting press

Grinding and polishing

The next step involved the mechanical grinding and polishing of the samples. A Struers LaboPol21 grinding and polishing machine (see Figure 3.3) was used for this step. Successive grades of 320, 500, 800, and 1000 silicon carbide grit paper were used for the grinding. The samples were ground on each grade for 15 to 30 minutes, depending on the finish quality. The grit paper was then replaced with a polishing cloth for the mechanical polishing. Alumina powder slurry was added to the powder cloth to aid in the polishing. A particle size of 1 µm Al_2O_3 was used for rough polishing, 0.3 µm Al_2O_3 for intermediate polishing, and 0.05 µm Al_2O_3 for final polishing. The polishing times also vary between samples. The grinding and polishing machine operates by compressing the samples onto a rotating plate containing either the grit paper or polishing cloth. The position of the samples and direction of rotation was specified according to the required finish. The slurry dosage was also controlled and varied according to the finish required. The final finish

required for the microhardness tests showed a “mirror-like” finish. This indicated that the samples were completely smooth and flat.

Figure 3.3 - Struers LaboPol21 grinding and polishing machine

Once prepared, the mechanical property evaluation tests were then performed. Microhardness tests were completed on the mounted square samples and compression tests on the rectangular samples. The experimental procedures for these tests are presented in the following section.

3.1.2 Microhardness test

The TIME MH-6 digital microhardness tester (see Figure 3.4) was used in this investigation to test the hardness of the titanium alloys. The apparatus and techniques used for the test are specified in the ASTM E384-99 standard. A uniform un-etched surface finish is required for the test and this was achieved during sample preparation. A 100g load indenter with a dwell time of 10 seconds upon indentation was used. Microhardness measurements of only the bulk materials were required for this investigation. Each indentation was placed a sufficient distance apart to avoid overlapping. Multiple readings were taken near the centre of each sample. Three samples for each grade were also used to achieve a greater data distribution and better average hardness value. The microhardness testing experimental matrix for Grade 4 and 5 is presented

in Table 3.1. A final hardness value for each grade was calculated from all the tests.

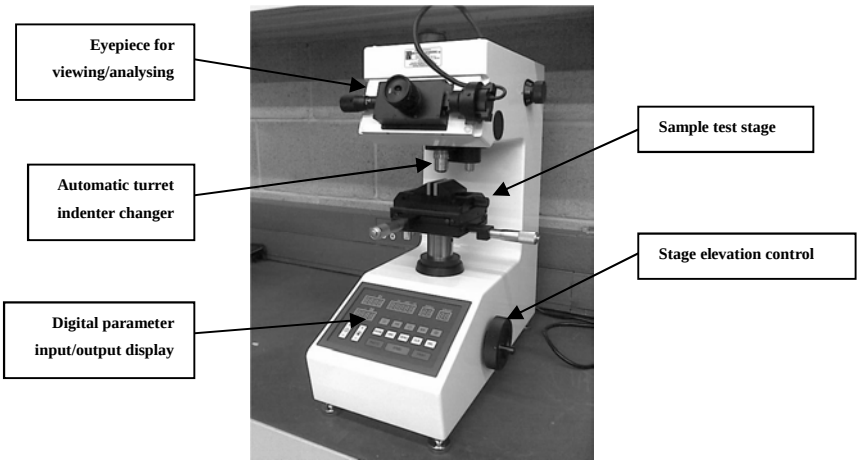

Figure 3.4 - TIME MH-6 digital microhardness tester

Table 3.1 - Vickers hardness experimental matrix

Grade 4					
Reading no.	**Sample #1**	**Reading no.**	**Sample #2**	**Reading no.**	**Sample #3**
1	VH Test 1	**1**	VH Test 16	**1**	VH Test 31
2	VH Test 2	**2**	VH Test 17	**2**	VH Test 32
3	VH Test 3	**3**	VH Test 18	**3**	VH Test 33
⋮		⋮		⋮	
14	VH Test 14	**14**	VH Test 29	**14**	VH Test 44
15	VH Test 15	**15**	VH Test 30	**15**	VH Test 45
Grade 5					
Reading no.	**Sample #1**	**Reading no.**	**Sample #2**	**Reading no.**	**Sample #3**
1	VH Test 46	**1**	VH Test 61	**1**	VH Test 76
2	VH Test 47	**2**	VH Test 62	**2**	VH Test 77
3	VH Test 48	**3**	VH Test 63	**3**	VH Test 78
⋮		⋮		⋮	
14	VH Test 59	**14**	VH Test 74	**14**	VH Test 89
15	VH Test 60	**15**	VH Test 75	**15**	VH Test 90

3.1.3 Compression test

The INSTRON 5500R compression test machine, as presented in Figure 3.5, was used to obtain properties of yield strength, Young's modulus, the stress-strain curve, and the compressive strength for the titanium alloys under investigation. The rectangular samples prepared from the stress-free materials were therefore tested under compression. Linear strain gauges were attached to each sample for strain measurement. The strain gauges were attached midway on both faces of the samples by a suitable adhesive. Connection terminals were also attached near the gauges. The connecting wires from the strain gauges and data acquisition system were then soldered to these terminals. An example of this strain gauge setup is illustrated in Figure 3.6. The samples were then placed length-ways in a bracket to prevent buckling or bending during compression. A 100 kN load cell applied a compressive force on the sample, with the strain measured continuously by the strain gauges. The data was captured on a computer from which the properties were determined. The compression testing experimental matrix for Grade 4 and 5 is presented in Table 3.2. From each test, the yield strength, compressive strength, young's modulus and stress-strain curve were determined.

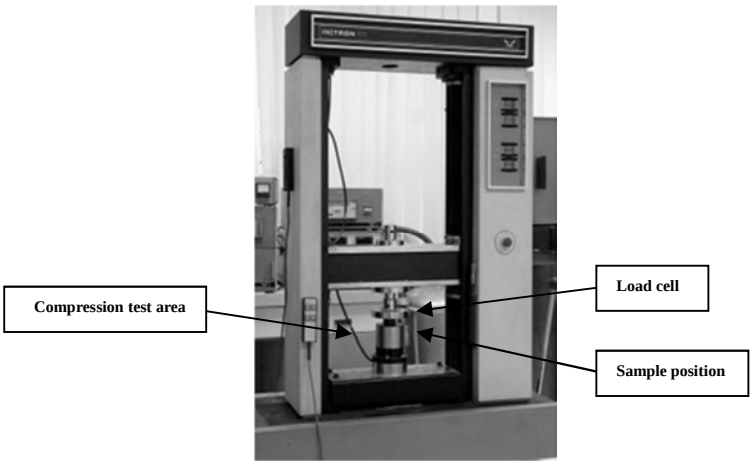

Figure 3.5 - INSTRON 5500R compression test machine

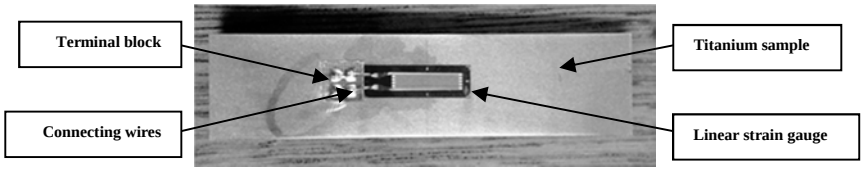

Figure 3.6 - Strain gauge setup for compression test

Table 3.2 - Compression test experimental matrix

Grade 4	
Sample #1	Comp Test 1
Sample #2	Comp Test 2
Grade 5	
Sample #1	Comp Test 3
Sample #2	Comp Test 4

3.2 Machining

The machining of the titanium alloys were conducted on an EFAmatic RT-20S CNC lathe (see Figure 3.7). The EFAmatic RT-20S is a slant bed CNC lathe that has a 200 mm three jaw power chuck. This machine was used due to its high accuracy and excellent production repeatability. It also allowed for fast cycle times, good chip flow and high pressure coolant usage. Both the x- and z-axes incorporate heavy-duty linear guides with large diameter ball-screws that are supported by precision angular bearings.

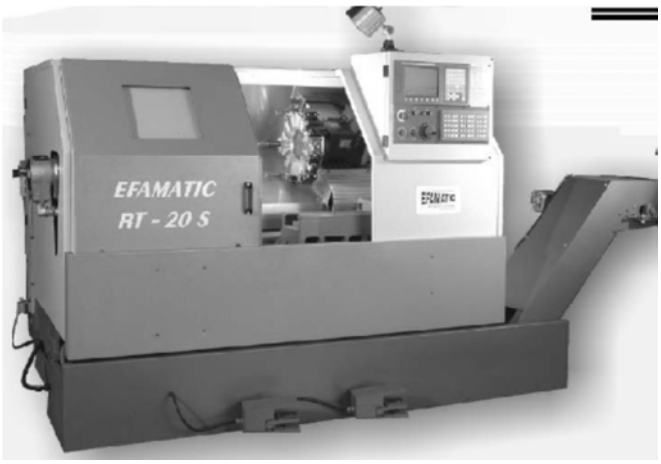

Figure 3.7 - EFAmantic RT-20S CNC lathe

The certified mechanical properties and chemical composition of the investigated materials are presented in Table 3.3 and Table 3.4. The cutting speed and depth of cut were varied during the machining of Grade 4 and 5 whilst the feed rate was kept constant. Cemented tungsten carbide Sandvik Coromant H1P tool inserts (see Figure 3.8) without chip breaker technology were used for the machining. The inserts have an 80° rhombic shape with a tool nose radius (r_t) of 0.8 mm. The entry angle of the tool was 95°.

Table 3.3 - Grade 4 mechanical properties and chemical composition

Mechanical properties		**Chemical composition**	
Tensile strength (MPa)	706	**N (%)**	0.006
Yield strength (MPa)	548	**C (%)**	0.008
Elongation (%)	24	**H (%)**	0.001
		Fe (%)	0.29
		O (%)	0.33
		Al (%)	-
		V (%)	-
		Ti (%)	Remainder

Table 3.4 - Grade 5 mechanical properties and chemical composition

Mechanical properties		**Chemical composition**	
Tensile strength (MPa)	990	**N (%)**	0.01
Yield strength (MPa)	890	**C (%)**	0.01
Elongation (%)	20	**H (%)**	0.002
		Fe (%)	0.03
		O (%)	0.06
		Al (%)	6.2
		V (%)	4.2
		Ti (%)	Remainder

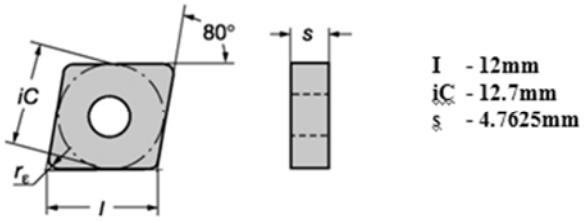

Figure 3.8 - Cemented tungsten carbide Sandvik Coromant H1P tool insert

The cutting parameters used in this investigation consisted of a 0.2 mm/rev constant feed rate at varying depths of cut and cutting speed. A 0.25 mm and 1.00 mm depth of cut were used. Cutting speeds of 70, 100, 150, 200, 250, and 300 m/min were used on Grade 4, and 70, 100, 125, 150, 175, and 200 m/min on Grade 5.

The cutting forces and cutting temperatures were continuously monitored during machining. The x, y, and z direction cutting forces were monitored and recorded by a piezoelectric dynamometer made by Kislter Instruments. The temperatures were measured by remote thermocouples at two different points on the cutting tool away from the cutting edge. The x, y and z orientations are illustrated in Figure 3.9. The x-axis runs parallel to the cutting tool and perpendicular to the billet. The y-axis is perpendicular to both the cutting tool and the billet. The z-axis runs axial to the billet and perpendicular to the cutting tool. The temperature measurement points were strategically placed to measure the cutting tool temperatures during machining. This positioning was simply for monitoring purposes and to identify any fluxes or sudden change in temperature during machining. If required, the temperature at the tool tip could be calculated from these points. The use and significance of the forces and temperatures measured are further explained in the results section. The experimental matrix for the machining of Grade 4 and 5 is presented in Table 3.5. The experiments were conducted in a randomised order to eliminate the possibility of false trends within the data.

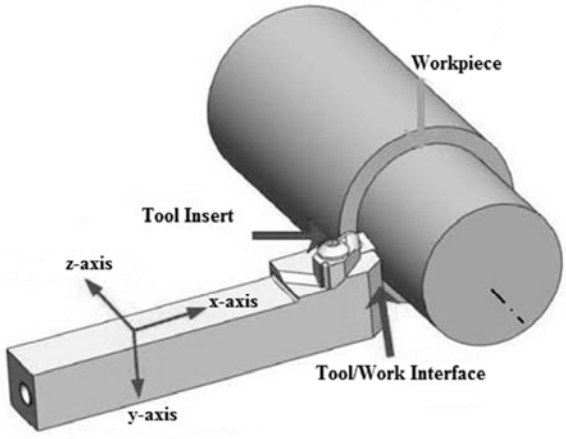

Figure 3.9 - Cutting force component orientation for machining

Table 3.5 - Machining experimental matrix

Grade 4				Grade 5		
Cutting speed (m/min)	**Depth of cut (mm)**			**Cutting speed (m/min)**	**Depth of cut (mm)**	
	0.25	**1.00**			**0.25**	**1.00**
100	Mach Test 1	Mach Test 2		**100**	Mach Test 13	Mach Test 14
150	Mach Test 3	Mach Test 4		**150**	Mach Test 15	Mach Test 16
70	Mach Test 5	Mach Test 6		**70**	Mach Test 17	Mach Test 18
300	Mach Test 7	Mach Test 8		**175**	Mach Test 19	Mach Test 20
200	Mach Test 9	Mach Test 10		**200**	Mach Test 21	Mach Test 22
250	Mach Test 11	Mach Test 12		**125**	Mach Test 23	Mach Test 24

3.3 Residual stress analysis

3.3.1 Sample preparation

The samples used for residual stress measurement were restricted by the size of the test area of the x-ray diffractometer in which they were analysed. The machined samples were therefore cut to a suitable size by wire-EDM due to its ability to produce a smooth, uniform cut without the addition of extra stresses, deformation or heat. This is important as these factors would alter the machining induced residual stresses, and prevent the observation of any effects. The machined sections were therefore separated by wire-EDM to

obtain smaller individual samples. Each sample represents a separate machining parameter. An example of these cut samples is presented in Figure 3.10.

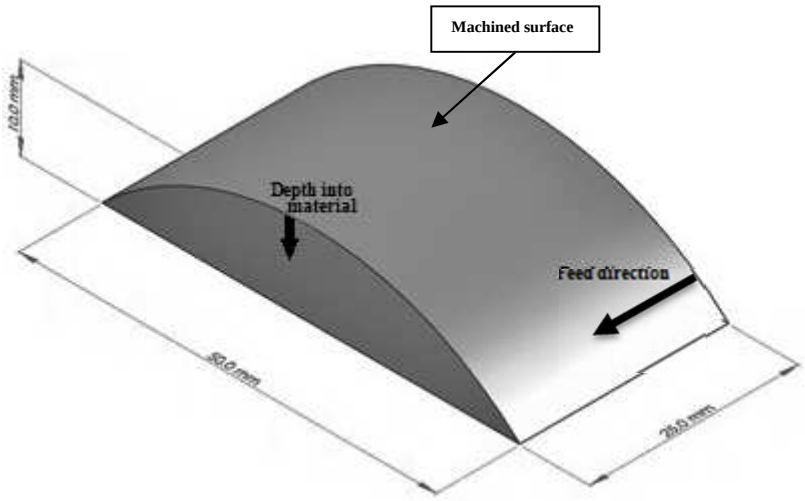

Figure 3.10 - Residual stress measurement sample

3.3.2 XRD measurement

X-Ray Diffraction (XRD) was used for the residual stress measurement due to its non-destructive nature and accuracy. A Bruker x-ray diffractometer (see Figure 3.11) was therefore used in this investigation. The residual stress measurements were conducted on the machined surface of the samples. The samples were then positioned and fixed at the centre of the sample stage of the X-ray diffractometer and the diffraction process was conducted.

Figure 3.11 - X-ray diffractometer

The first step in XRD was calibration. To calibrate the diffractometer, a specimen of known composition, such as tungsten, was measured. This also confirmed the alignment of the x-ray gun. Once calibrated, a stress-free, texture-free sample of the same material tested in the investigation was measured. This measurement was used to obtain the stress free lattice parameter (*do*) of the material. Copper (Cu-Kα) tube radiation was used to determine the peaks with the highest intensity. The samples were rotated through 3 specific tilt angles of Phi = 0°, 90° and 45°. Each Phi angle was also rotated through specific Psi angles and steps, all in the region of the most intense peaks. A diffractogram was obtained for each sample and superimposed on the stress-free pattern scan. Specific computer software then determined the peak variations for each sample and calculated the stress tensor. With the full stress tensor defined, the stress components of importance for this investigation could then be extracted. These included the longitudinal (σ_{11}), transverse (σ_{22}) and shear (σ_{12}) stresses. The longitudinal stresses run along the cutting direction and the transverse stresses run perpendicular to the cutting direction, as illustrated in Figure 3.12. This measurement process was repeated for each sample of Grade 4 and 5 and the experimental matrix representing each test is presented in Table 3.6. The tests were again randomised to eliminate any false trends in the data.

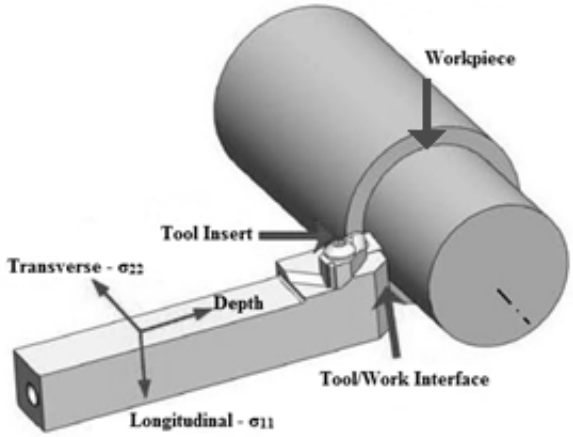

Figure 3.12 - Stress component orientation from machining

Table 3.6 - Residual stress experimental matrix

Grade 4				Grade 5		
Cutting speed (m/min)	Depth of cut (mm)			Cutting speed (m/min)	Depth of cut (mm)	
	0.25	1.00			0.25	1.00
100	RS Test 1	RS Test 2		**100**	RS Test 13	RS Test 14
150	RS Test 3	RS Test 4		**150**	RS Test 15	RS Test 16
70	RS Test 5	RS Test 6		**70**	RS Test 17	RS Test 18
300	RS Test 7	RS Test 8		**175**	RS Test 19	RS Test 20
200	RS Test 9	RS Test 10		**200**	RS Test 21	RS Test 22
250	RS Test 11	RS Test 12		**125**	RS Test 23	RS Test 24

3.4 Microstructural analysis

3.4.1 Sample preparation

The machined edge of each specimen was examined for microstructural analysis. Further cutting of the samples was therefore done to expose the machined edge. The reduced sample size from cutting also fitted into the moulds used during microscope analysis. The sample preparation steps of cutting, mounting, grinding, polishing and etching the samples are presented in the current section.

Cutting

Wire-EDM was used to cut the samples to ensure that no extra distortions were introduced as they may have affected the microstructure. The corner of the samples was cut to reveal the machined edge profile leading into the depth of the material. This allowed for analysis to be done on the curved section of the sample where the machining affected the material the most. An example of this test sample is presented in Figure 3.13. The highlighted portion represents the area under analysis.

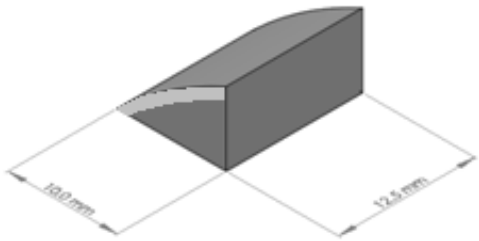

Figure 3.13 - Model of sample used for microstructural analysis

Mounting

The microstructural analysis samples were mounted in a LECO mount press, as was done with the microhardness samples. Care was taken to ensure that the surface exposing the machined edge was placed face down on the mounting piston. The same steps as set out in Section **Error! Reference source not found.** were followed to achieve the final mounted samples. Once all the samples were mounted and cooled, the subsequent steps of grinding and polishing were completed.

Grinding and polishing

The mechanical grinding and polishing of the samples was completed by following the same procedures set out in Section 0. The Struers LaboPol21

grinding and polishing machine was used with grit grades of 320, 500, 800, and 1000. The final surface finish however for these samples was crucial. The "mirror-like" finish was important for the ensuing step of etching. If not completed correctly, the etching would not reveal a clear grain structure. Extra care was therefore placed on the polishing to ensure an acceptable surface finish.

Etching

Kroll's reagent was used to etch the polished samples. It consists of 1-3 ml HF 40%, 2-6 ml HNO_3 55% and 91 ml water. The process of etching exposes the grain structure of the material allowing for further examination of the sample. This is a time dependant and time sensitive process. The exposure time on each sample was therefore very important. The time frame is usually between 3 and 10 seconds for Kroll's reagent, but differs for each material. The visibility of the grain structure becomes unclear if under- or over-etched. This greatly affects the outcome during SEM and microscope work. It was therefore important to etch each sample carefully.

3.4.2 Optical microscopy

The prepared samples were subsequently investigated with an optical microscope to analyse the grain structure at their machined edge. An Olympus BX-51M Optical Microscope with camera attached (see Figure 3.14) was used to measure and analyse the grain deformations. These included the deformation angles and depths. The magnification was set to 25X and 50X for the Grade 4 and Grade 5 samples respectively. This was due to the smaller grain size of the Grade 5 samples. Images were taken at different sections along the machined edge to minimise discrepancies. A minimum of 3 clear images were taken for each sample. Analytical software was then used to measure grain reorientation and grain deformation depth for each image set.

This is illustrated in Figure 3.15 where the angle between the reorientated grains and undisturbed grains was measured to obtain the deformation angle and the distance from the machined edge to the point in the material where the deformation reached was measured to find the deformation depth. Care was taken to ensure the measurements were done accurately. The slightest mistake could cause a large change in measurement due to the magnification used. The experimental matrix for the microstructural analysis is presented in Table 3.7.

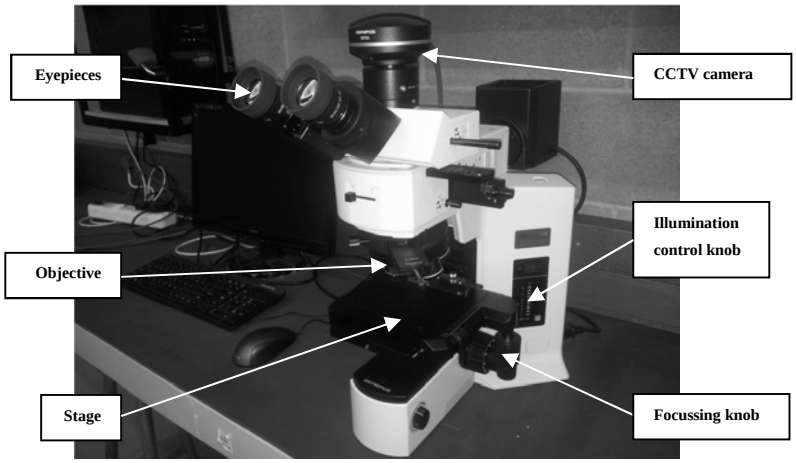

Figure 3.14 - Olympus BX-51M optical microscope

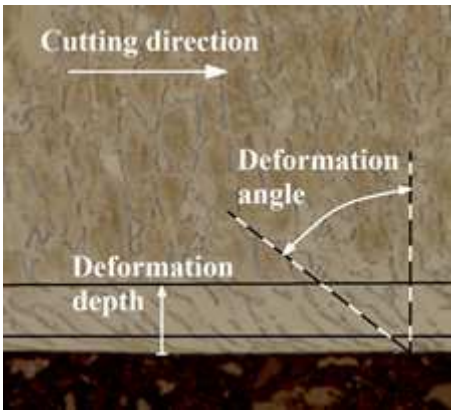

Figure 3.15 - Schematic illustrating deformation angle and depth

Table 3.7 - Microstructural analysis experimental matrix

Grade 4				Grade 5		
Cutting speed (m/min)	**Depth of cut (mm)**			**Cutting speed (m/min)**	**Depth of cut (mm)**	
	0.25	**1.00**			**0.25**	**1.00**
100	Micro Test 1	Micro Test 2		**100**	Micro Test 13	Micro Test 14
150	Micro Test 3	Micro Test 4		**150**	Micro Test 15	Micro Test 16
70	Micro Test 5	Micro Test 6		**70**	Micro Test 17	Micro Test 18
300	Micro Test 7	Micro Test 8		**175**	Micro Test 19	Micro Test 20
200	Micro Test 9	Micro Test 10		**200**	Micro Test 21	Micro Test 22
250	Micro Test 11	Micro Test 12		**125**	Micro Test 23	Micro Test 24

3.4.3 Scanning electron microscopy

A JEOL Scanning Electron Microscope (SEM) (see Figure 3.16) was used to examine the grain structure of the machined alloy samples at higher magnification. The sample preparation for SEM was the same as that for optical microscopy. Magnifications of up to 5000X were used to produce images of the grain structure. Care was taken to obtain the highest levels of focus, contrast and brightness. Contrast is the principal determinate of SEM image quality, in that a higher contrast produces a better field depth. However, if the contrast is too high, a grainy image is produced. The interaction between these contrast effects and surface texture may result in unexpected images such as excessive shadows. The polyfast mounting resin used in this study is one means of reducing these effects. Other methods include carbon tape or carbon-coating.

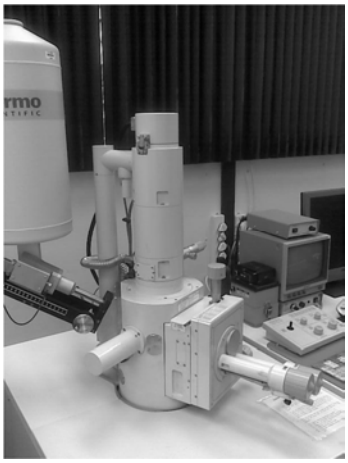

Figure 3.16 - JEOL Scanning Electron Microscope

Upon completion of the experimental program, the results were documented and discussed in the following chapter.

Chapter 4. Results and Discussion

This section provides and discusses the main results and findings in the investigation. The results and discussion of the microhardness and compression tests can be found in Appendix A and Appendix B respectively as they do not form part of the main findings. Data for cutting force, residual stress state and microstructural changes are presented and discussed in this chapter. The raw data and additional graphs for each analysis parameter are presented in the appendices.

4.1 Cutting tool temperatures

Cutting tool temperature is measured as an aid to monitor for sudden changes in the cutting environment. These may include sudden temperature changes due to chip snarling, tool breakage and the onset of rapid tool failure due to excessive wear. The measurements do not represent the “true” cutting temperatures as they are measured a finite but constant distance from the cutting edge. The results and discussions are therefore presented in Appendix C only, with the raw data and graphs depicting each temperature profile illustrated in Appendix D.

4.2 Cutting forces

The cutting forces are monitored and measured for each cutting speed and depth of cut. The forces in the x- (thrust), y- (feed), and z- (main) axis directions are measured. These forces are monitored at a rate of 200 measurements per second. The force values reported in this section are obtained by evaluating the appropriate force at 50% of the total cut length. The raw data and individual force history graphs are presented in Appendix E.

The variation of cutting force as a function of cutting speed for Grade 4 and 5 at different depths of cut is presented in Figures 4.1 to 4.4. The graphs show that all the cutting forces are largely insensitive to cutting speed. The main (z-direction) cutting forces do however decrease by a small amount of approximately 15% over the cutting speed range for the 0.25 mm cut depths and 5% for the 1.00 mm cuts. This is consistent with the force measurements taken by Klocke *et al.* [71] where a similar decrease of approximately 8% is observed over the same cutting speed range for Ti-6Al-4V, albeit with a different feed rate (0.1 mm/rev) and cutting tool material (whisker-reiforced ceramic, CA+SiC). The decrease in main cutting force is largely the result of local workpiece softening that is more pronounced at the higher cutting speeds. This is consistent with traditional machining where an increase in cutting speed causes an increase in cutting temperature which in turn "softens" the material and therefore reduces the cutting forces [139]. A reduction in cutting force may also occur because of the effect of built-up edge that diminishes with increased cutting speed. Fang and Wu [139] also found a similar decrease in force with increasing cutting speed during a comparative study of the high speed machining of Ti-6Al-4V and Inconel 718. Their study however incorporated lower feed rates of between 0.075 mm/rev and 0.120 mm/rev and a cutting tool material of cemented carbide (KC 8050) with TiC/TiN/TiCN coating.

An increase in depth of cut results in substantially larger main cutting forces for both grades. The results are nearly linear (as a function of cut depth) with force increases of approximately 350% resulting from an increase of 400% in cut depth. This is directly related to the material removal rate increasing linearly with cut depth. A similar increase in force is observed by Wang *et al.* [140] however, their results were obtained during high speed milling of Ti-6Al-4V using binderless CBN tools. They demonstrated a 300% increase in main cutting force with only a 200% increase in depth of cut. Their results were however also obtained at a higher cutting speed range of between 300 m/min and 400 m/min and at a much lower feed rate of only 0.075 mm/rev.

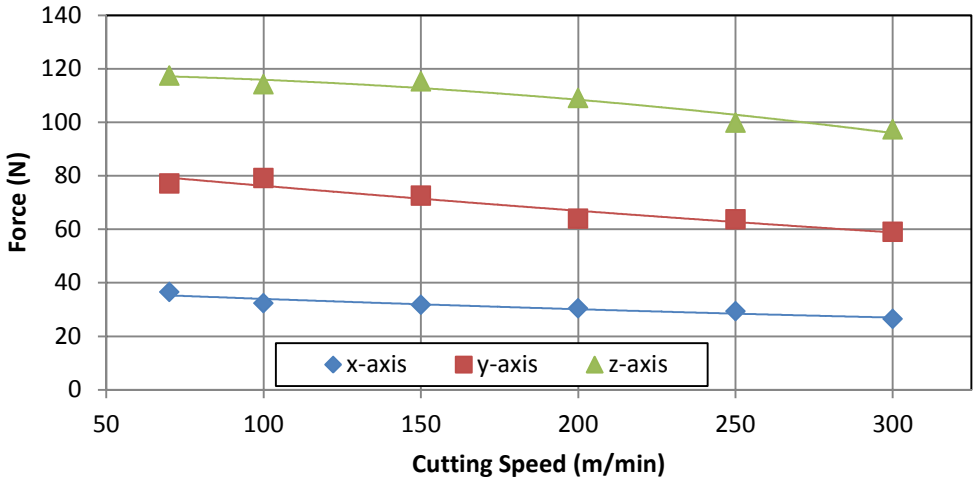

Figure 4.1 - Variation of cutting force for Grade 4 at 0.25 mm DOC

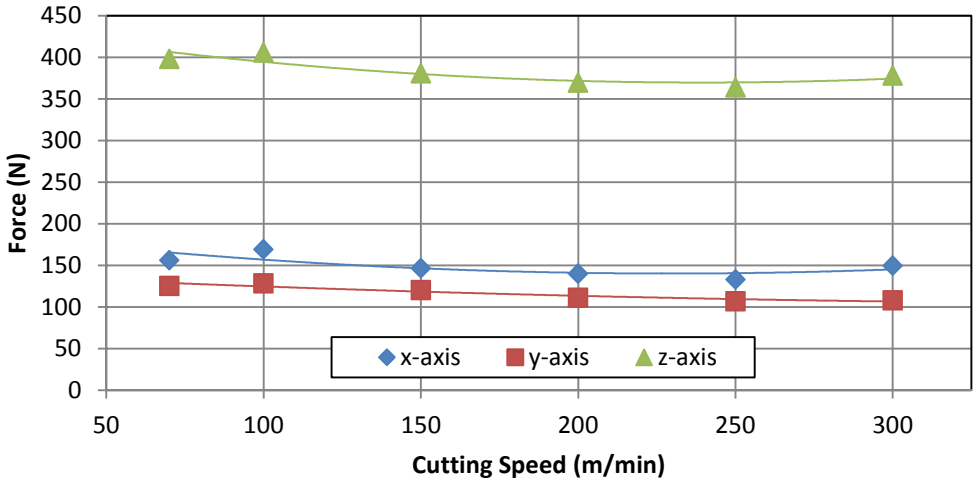

Figure 4.2 - Variation of cutting force for Grade 4 at 1.00 mm DOC

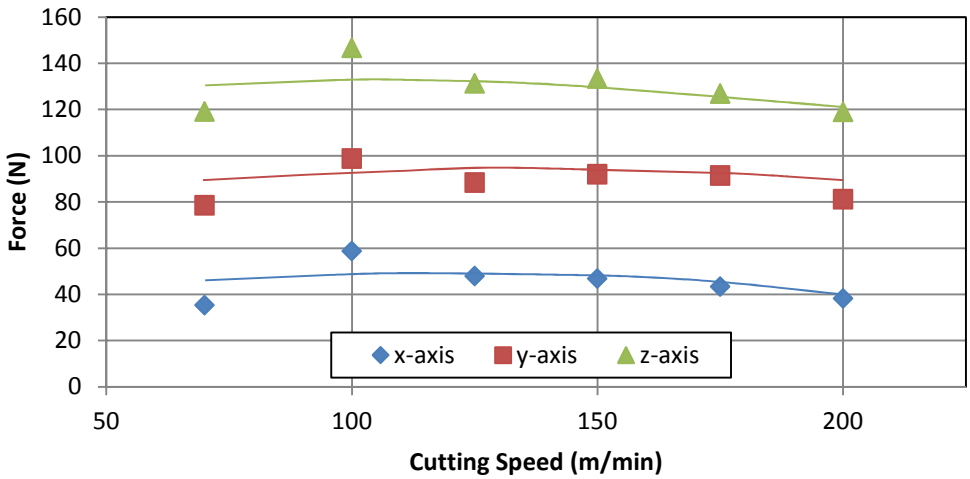

Figure 4.3 - Variation of cutting force for Grade 5 at 0.25 mm DOC

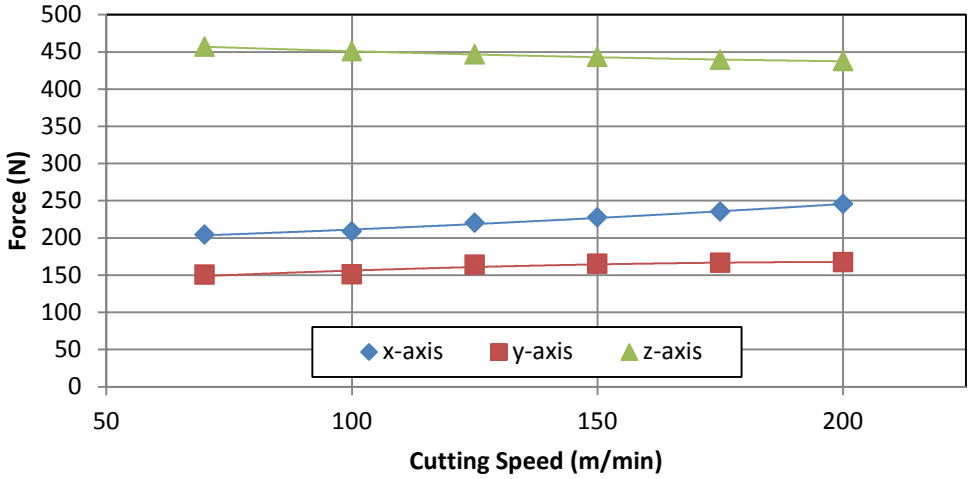

Figure 4.4 - Variation of cutting force for Grade 5 at 1.00 mm DOC

The force data as presented above was recorded after a constant cut length for all tests. The data does however show that the tool life may be severely restricted at high cutting speeds (larger than 150 m/min) for the larger depth of cut (1 mm) on Grade 5. A dramatic increase in temperature and cutting force started to manifest itself at extended cut lengths for cutting speeds above 150 m/min. This is presented in Figure 4.5 (a) to (c). These clearly show that at extended cut lengths rapid tool wear induces a dramatic temperature rise (see Figure D.22 to Figure D.24 of Appendix D) that leads to tool breakdown and localised welding between the tool and work piece. This in turn results in a dramatic increase of the cutting force.

These sudden increases manifest after an initial cutting distance where the cutting forces are comparable to those at the other cutting speeds. The extracted data, as displayed in Figure 4.4, is therefore not affected by these. The sudden increases are due to tool wear that progressively occurs up to a point where thermal “run away” then occurs. At this point the system loses its ability to conduct the heat at a significant rate away from the cutting interface. A sudden increase in cutting temperature then leads to an increased localised adhesion (welding) between the tool and workpiece, which dramatically increases the tool wear and causes a further increase in temperature. These temperature increases are displayed and discussed in Appendix C.

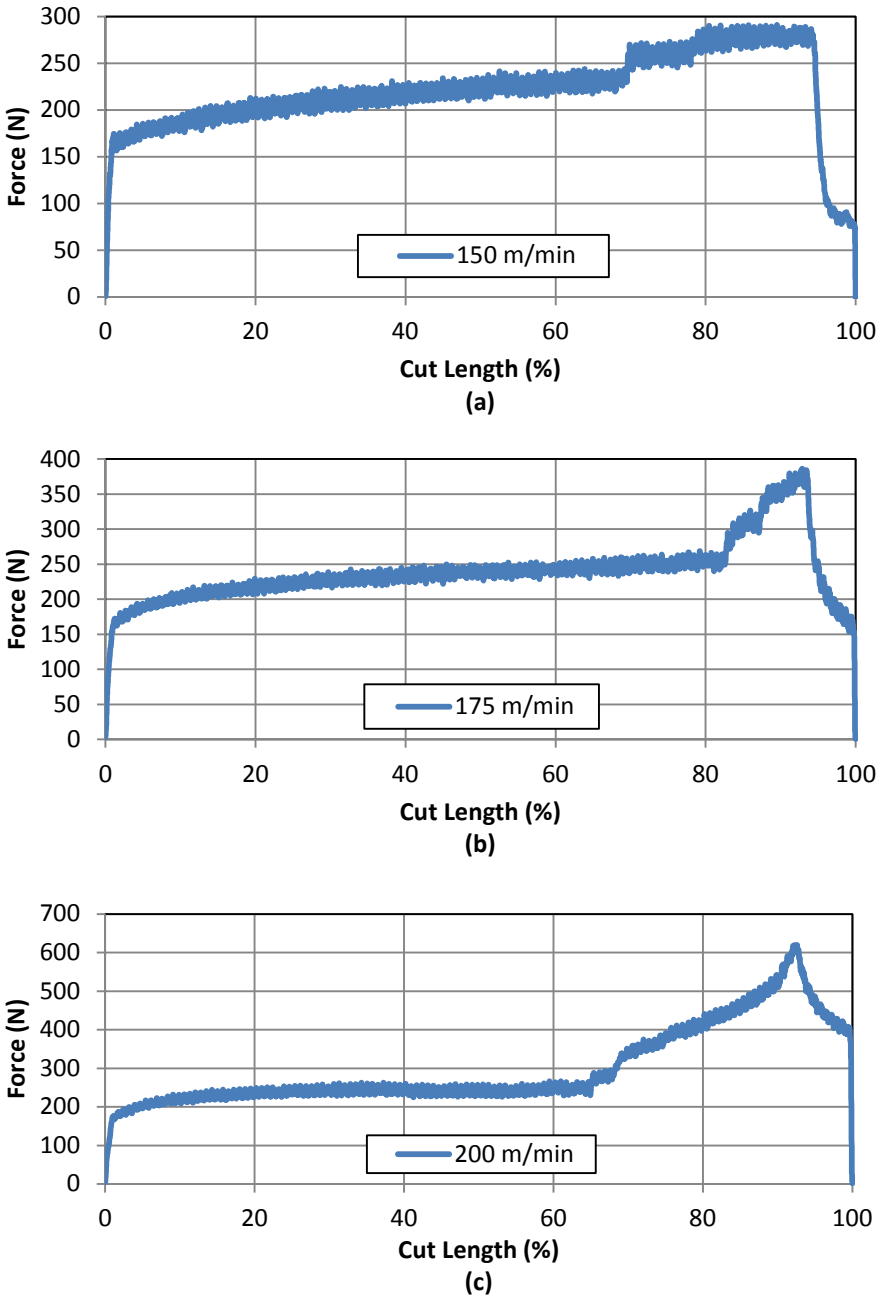

Figure 4.5 - X-axis force profiles for (a) 150 m/min, (b) 175 m/min and (c) 200 m/min cutting speeds on Gr 5 at 1.00 mm DOC

It is clear that rapid tool wear occurs when cutting Grade 5 at speeds in excess of 150 m/min. Although cutting may be possible at higher speeds it would only become viable and practical by utilising, for example, advanced cooling techniques. To understand the phenomenon more clearly, further investigation of the chip formation and tool wear etc. at these high cutting speeds is required.

A comparative graph illustrating the main cutting forces (z-axis forces) as a function of cutting speed for Grade 4 and 5 at different depths of cut is presented in Figure 4.6. No substantial difference between the two grades occurs for the finish cut, with a small difference of only approximately 11% recorded for the 1.00 mm cut. This is substantially smaller than would be expected in light of their mechanical property differences. The increase is largely due to the higher strength and hardness of Grade 5, however describing the small scale increase requires further analysis of the chip morphology and cutting tool inserts. It also points to the fact that the cutting force is not just a function of the material properties, but that the chip morphology and friction may also play important roles.

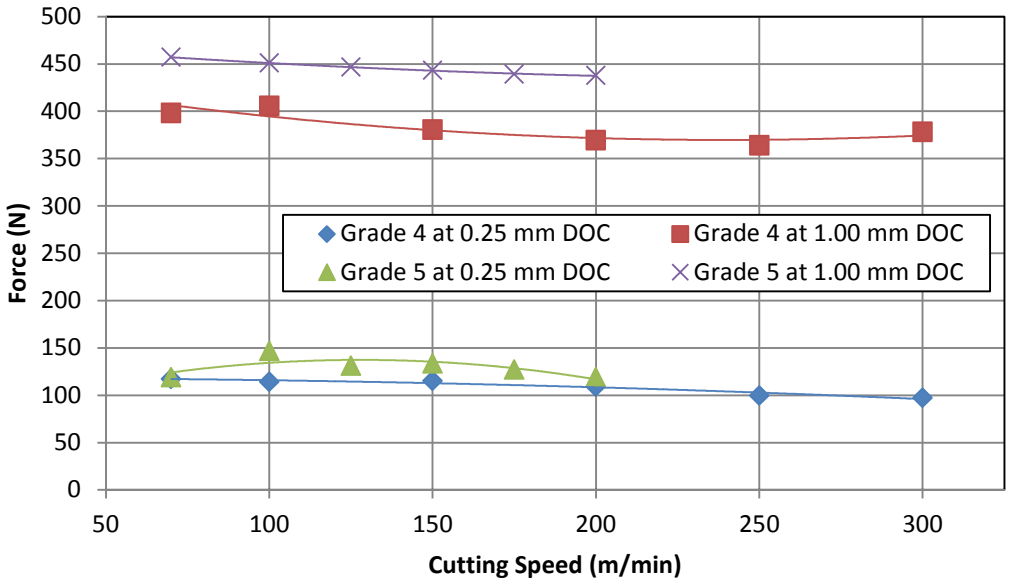

Figure 4.6 - Variation of main cutting forces for Grade 4 and 5

4.3 Residual Stresses

The residual stresses are measured at the centre of the machined surface of each sample (i.e. at 50% of the cut length). XRD software then produces full stress tensors for each measurement from which the longitudinal (σ_{11}), transverse (σ_{22}), and shear (σ_{12}) stresses are extracted. The full stress tensors are provided in Appendix F with the extracted stresses presented in Table F.1

and Table F.2. The graphs depicting these stresses are presented and discussed in the current section.

The variation of σ_{11}, σ_{22}, and σ_{12} as a function of cutting speed for Grade 4 and 5 at different depths of cut are presented in Figures 4.7 to 4.10. The graphs show that no appreciable change in shear stress occurs and their magnitudes are small in comparison to the longitudinal and transverse stresses. The σ_{11} and σ_{22} stresses are relatively high in compression at low cutting speeds and become more tensile as cutting speeds increase, before changing direction to compressive again at high cutting speeds. The same residual stress trends are observed during the high speed turning of Inconel 718, investigated by Pawade *et al.* [114]. Pawade explains the changes in residual stresses by describing the significance of heat dissipation during the machining of Inconel 718, a material with poor thermal conductivity, much the same as titanium alloys. At low cutting speeds, more heat is dissipated into the machined surface due to the low material removal rate. This causes thermally dominant machining deformation which introduces tensile residual stresses (hence the increase in the tensile direction). At high cutting speeds, less heat is dissipated into the machined surface due to the high material removal rate. This therefore reduces the amount of thermally dominant machining deformation and increases the mechanically dominant machining deformation which introduces compressive residual stresses (hence the increase in the compressive direction) [114].

Puerta Velasquez *et al.* [17] also found similar residual stresses, albeit during the utilisation of a different carbide tool insert consisting of a diamond build-up edge (polycrystalline diamond from Oerlikon) and dry cut at a different feed rate (0.12 mm/rev), rake angle (0°) and clearance angle (7°). Their results also produced largely compressive residual stresses at low cutting speeds that tended towards tension with an increase in cutting speed. They found that the longitudinal residual stress component became tensile at a cutting speed of ±90 m/min. The current data shows that Grade 4 becomes tensile at ±110 m/min and Grade 5 at ±145 m/min for 0.25 mm depth of cut only. The

behaviour does not manifest itself at higher cut depths. The residual stress state for a 1.00 mm cut remains predominantly compressive for the cutting speed range investigated here.

The substantially lower tensile transition temperature as obtained by Puerta Velasquez is the result of their dry cutting process. The data then suggests that this tensile transition temperature is fundamentally a function of the on-going heat transfer process during machining. The tensile transition temperature is therefore a function of the cooling rate (cooling techniques employed), the heat production (depth of cut) and the rate of heat production (cutting speed).

The 1.00 mm cuts reveal higher compressive residual stresses. The increased depth of cut affects the residual stresses in the same way as the increased cutting speed. An increase in depth of cut creates an increased material removal rate and therefore larger compressive stresses. This is again found to be similar for Inconel 718 investigated by Pawade *et al.* [114]. The increased compressive residual stresses also lowers, if not removes, the presence of tensile residual stresses in the titanium alloy grades.

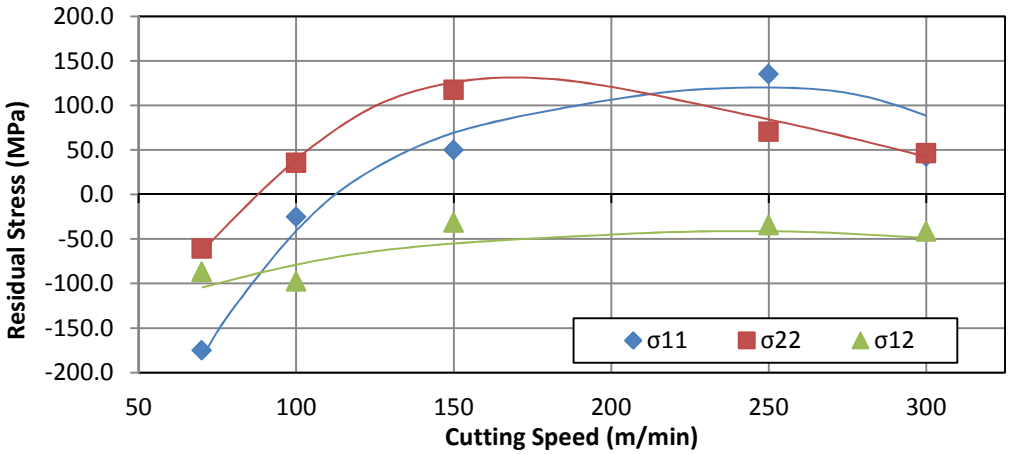

Figure 4.7 - Variation of residual stresses as a function of cutting speed for Grade 4 at 0.25 mm depth of cut

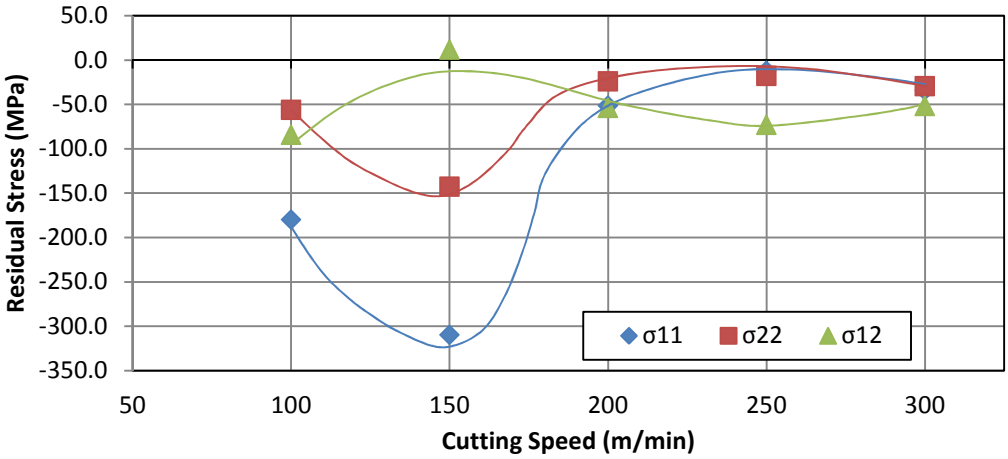

Figure 4.8 - Variation of residual stresses as a function of cutting speed for Grade 4 at 1.00 mm depth of cut

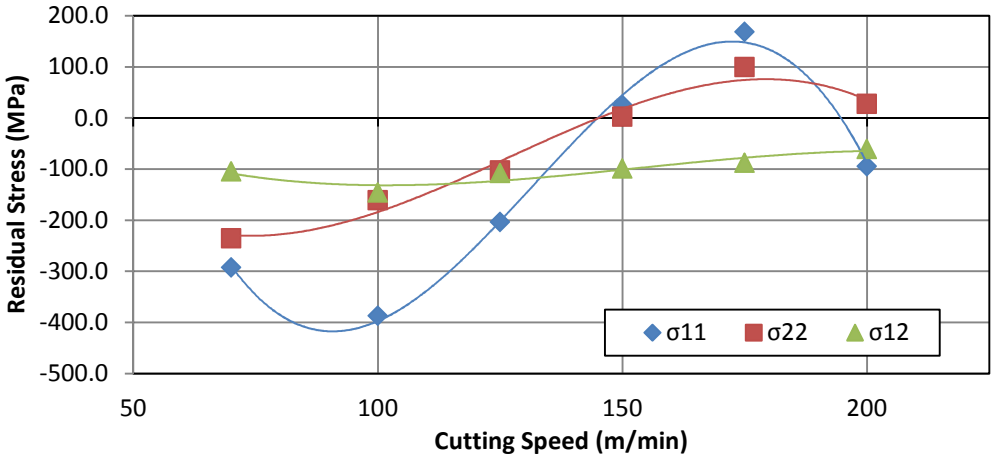

Figure 4.9 - Variation of residual stresses as a function of cutting speed for Grade 5 at 0.25 mm depth of cut

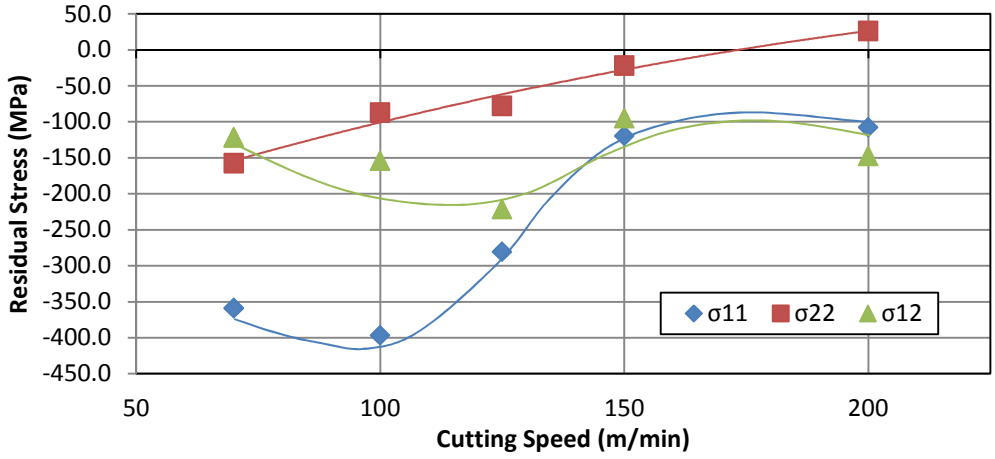

Figure 4.10 - Variation of residual stresses as a function of cutting speed for Grade 5 at 1.00 mm depth of cut

The residual stress measurements for Grade 5 are also more compressive than Grade 4. This is largely due to their physical properties. The higher strength and hardness of Grade 5, as well as its lower machinability, causes increased cutting forces and therefore increased compressive residual stresses. Further analysis of the chip morphology and cutting tool inserts however is required to fully describe the small scale increase.

4.4 Subsurface Microstructure

Two examinations are carried out for microstructural analysis. The deformed grain structure at the machined edge is analysed. The deformation angle and depth caused by the extent of the microstructural changes induced by machining are measured. The microstructural images, along with the raw extracted data are presented in Appendix G. The average deformation angles and depths are presented and discussed in the current section.

Puerta Velasquez *et al.* [17] identified three distinct regions near the surface of titanium alloys which exist as a result of machining. The P3 region is directly beneath the surface and may extend to depths of only a few microns (see Figure 4.11). This region is characterised by the grains undergoing severe deformation by extension and rotation. The P2 region is found beyond region P3 in depth and is characterised by the rotation and realignment of the grains only. It extends up to region P1 where no optically discernible difference in grain structure from the bulk material is observed. The extent of P2 is usually described by its maximum observable depth (onset of P1) and the grain deformation angle. The deformation angle is measured as the average realised angle of grains relative to the surface normal (see Figure 4.11). The extracted average angles and depths and presented in Table G.1 and G.2 of Appendix G respectively.

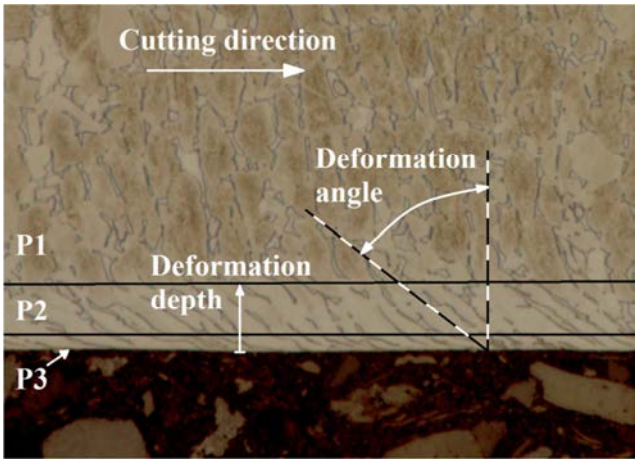

Figure 4.11 - Schematic illustrating distinct deformation zones and measurments

The variation of deformation angle and deformation depth as a function of cutting speed for Grade 4 and 5 at different depths of cut are presented in Figures 4.12 to 4.15 respectively. The graphs show a clear and nearly linear decrease in deformation angle and depth with increase in cutting speed. In effect this implies that higher cutting speeds lead to lower grain rotation and a smaller influence region. This seems to indicate the influence of strain rate sensitivity. Titanium alloys are known to be strain rate sensitive [141]. Strain rate sensitivity is especially predominant at higher cutting speeds associated with machining. An increase in cutting speed inevitably leads to an increase in strain rate which leads to a higher yield strength. The workpiece material effectively strengthens with an increase in cutting speed. This should lead to a lower deformation angle and deformation depth with increasing cutting speed. There is however a complicated interaction also occurring with the workpiece softening effect that increases with cutting speed because of the associated increase in cutting temperature. This increase in cutting temperature is however kept to a minimum due to cooling techniques employed and therefore the current data suggests that the strain rate sensitivity dominates this interaction for the processing parameters investigated here.

These results are however contrary to the findings of Puerta Velasquez *et al.* [17] who found an increase in deformation depth to occur with increase in cutting speed. Their results may be attributed to the softening effect being

more dominant over strain rate sensitivity as dry cutting techniques were employed. This therefore allowed for a greater increase in cutting temperature to occur with increase in cutting speed. The higher temperatures caused greater material softening which lead to an increase in deformation depth with increasing cutting speed.

The depth of cut also has an effect on the magnitude of deformation. For Grade 4, the 0.25 mm cut produces larger deformations than the 1.00 mm cut. This may be attributed to a tearing effect associated with a small cut depth. At small cut depths the material experiences more of a tearing effect where the chips are torn from the material instead of being cut or sheared off. The tearing affects a larger amount of grains, resulting in larger deformation angles and depths for the 0.25 mm cut. For Grade 5 however, the deformations observed are larger for the 1.00 mm cut than the 0.25 mm cut. This is opposite to the findings for Grade 4 and may be explained by material characteristic differences between the two grades. Due to the higher hardness of grade 5, less tearing occurs with an increase in cut depth as a larger cutting force is required to remove the material.

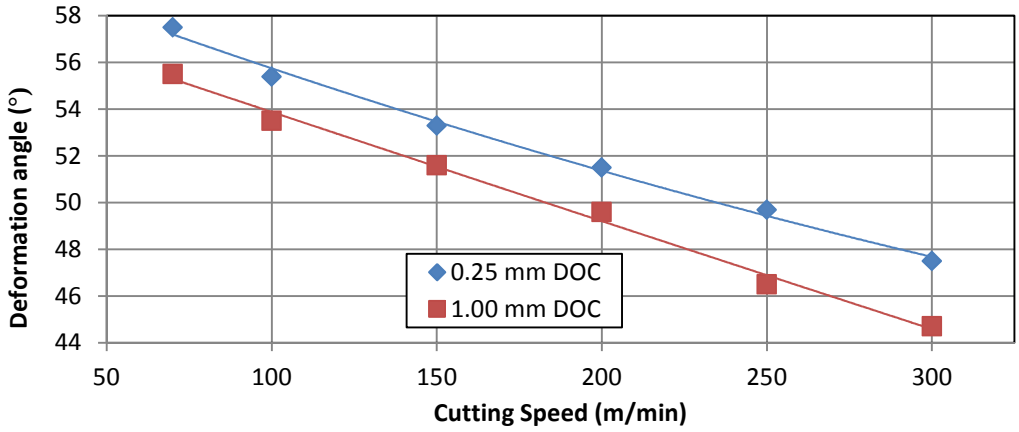

Figure 4.12 - Variation of deformation angle as a function of cutting speed for Grade 4

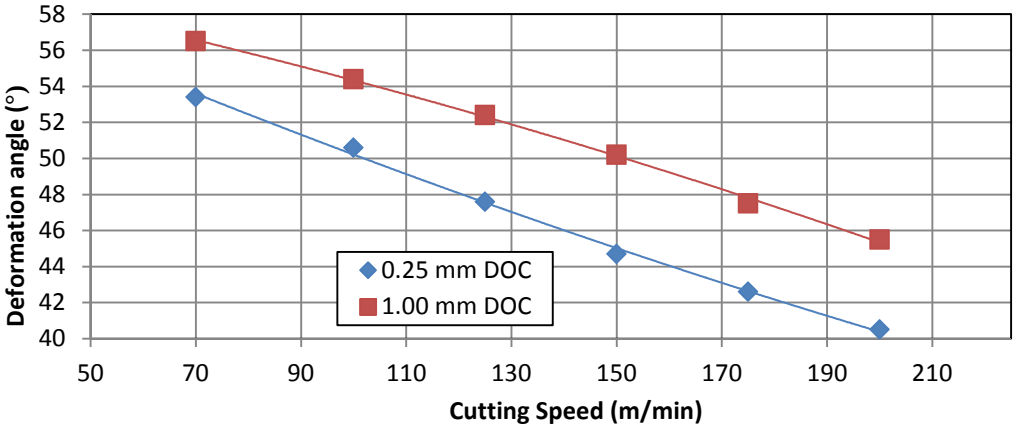

Figure 4.13 - Variation of deformation angle as a function of cutting speed for Grade 5

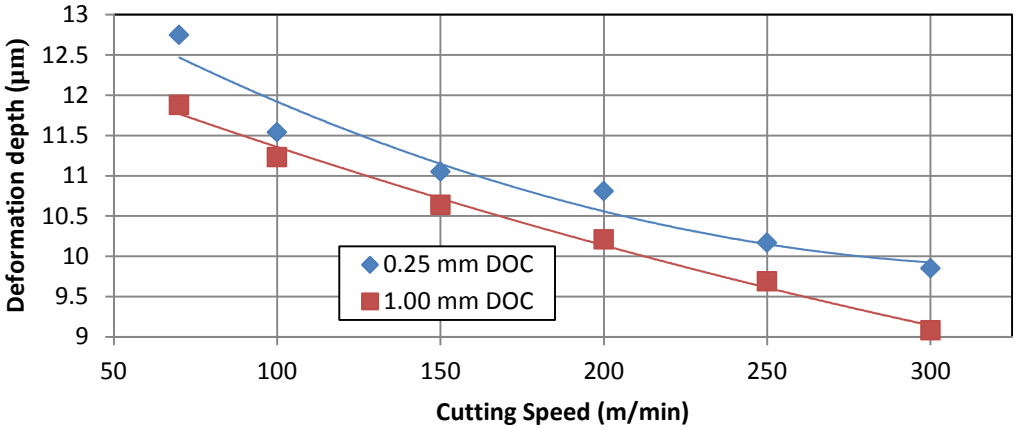

Figure 4.14 - Variation of deformation depth as a function of cutting speed for Grade 4

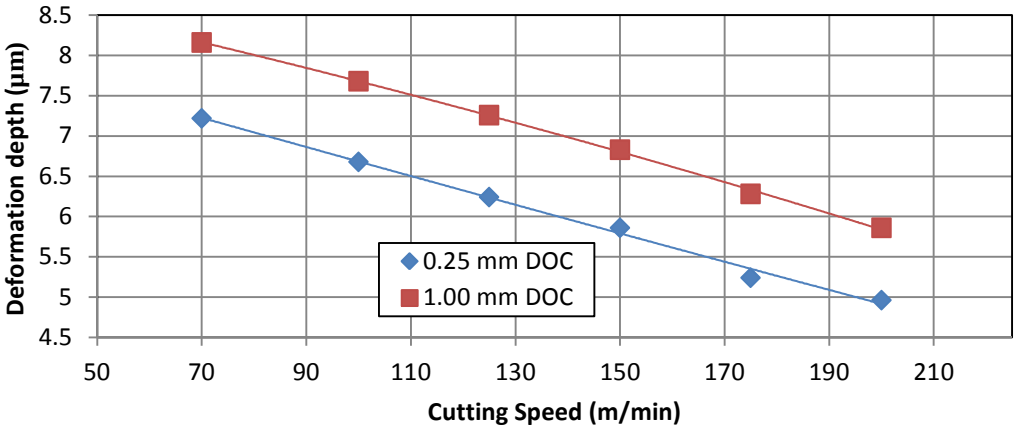

Figure 4.15 - Variation of deformation depth as a function of cutting speed for Grade 5

Comparative graphs illustrating the variation of deformation angle and deformation depth as a function of cutting speed for Grade 4 and 5 at different depths of cut are presented in Figures 4.16 and 4.17 respectively. The Grade 5 samples have smaller deformation angles and depths than the Grade 4 samples and also decrease more rapidly with increase in cutting speed. This may be described by the material characteristics of the two materials. Due to the "softer" material of Grade 4, less force is required to cut the material and therefore a greater tearing effect is observed, causing larger deformations. The harder and stronger material characteristics of Grade 5 entail larger cutting forces during machining which reduce the amount of tear and therefore the scale of deformation.

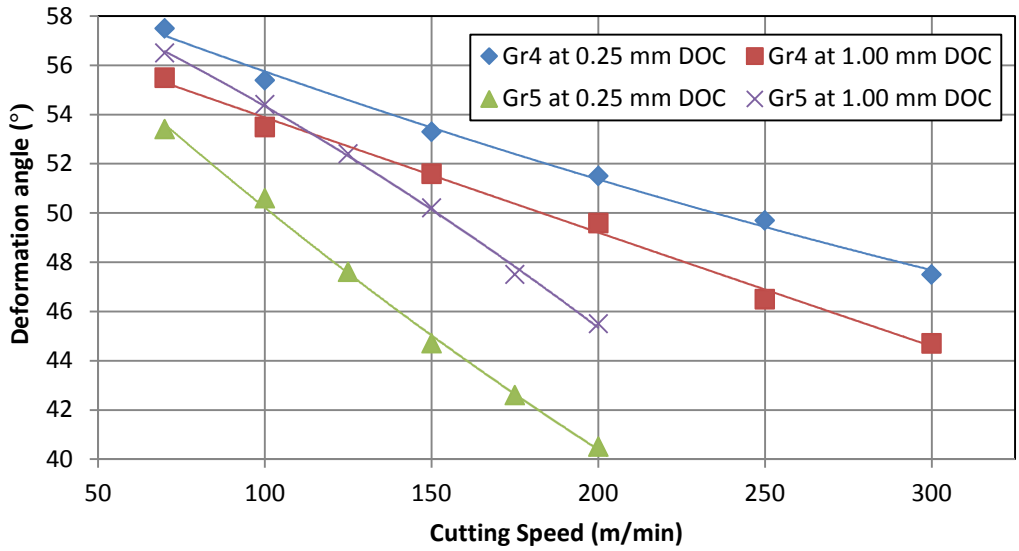

Figure 4.16 - Combined variation of deformation angle as a function of cutting speed for Grade 4 and 5

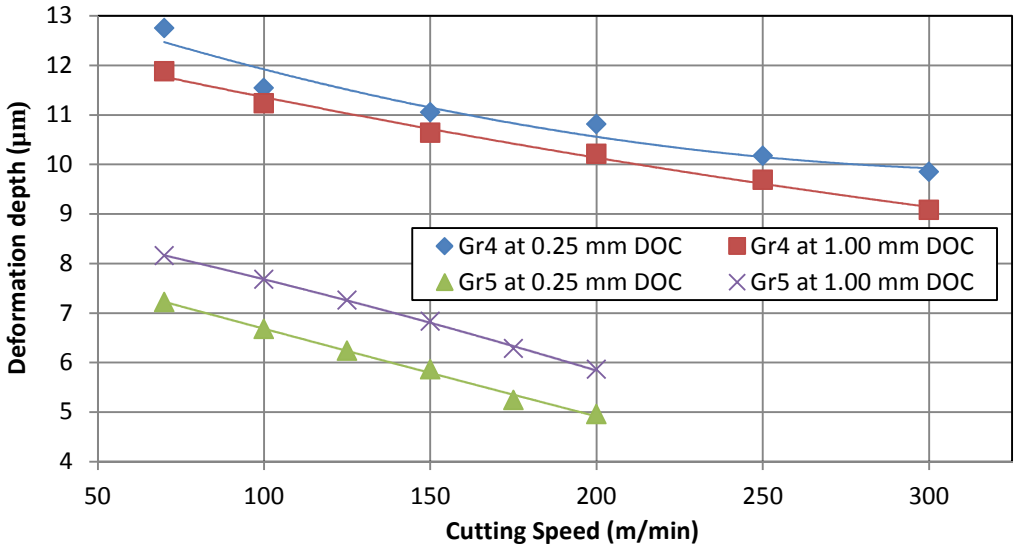

Figure 4.17 - Combined variation of deformation depth as a function of cutting speed for Grade 4 and 5

Chapter 5. Conclusion

This investigation demonstrates the effect that machining parameters have on the induced residual stresses and sub-surface microstructure of Grade 4 and 5 titanium alloys during high performance turning. The cutting speeds analysed range from 70 m/min to 300 m/min for Grade 4 and 70 m/min to 200 m/min for Grade 5. Depth of cut is between 0.25 mm and 1.00 mm.

The literature review clearly showed that there still exists a significant lack of good experimental data that reflects the effect of machining parameters on the induced residual stress field of titanium alloys. This is especially true for the commercially pure titanium alloy grades and specifically for Grade 4. The literature review also showed that surface integrity and more specifically machining induced surface integrity effects are currently a topical and important area of interest especially as regards to high performance materials such as titanium alloys.

Analysis of the cutting forces revealed inconsistent increases at cutting speeds of 150, 175 and 200 m/min for Grade 5 at a 1.00 mm depth of cut. Further analysis of the force profiles revealed sudden and dramatic increases in cutting force after an initial 50 % cutting distance. This may be due to tool wear that progressively occurred up to a point where thermal “run away” then followed. Therefore, additional investigation of chip formation and tool wear etc. at these high cutting speeds is required to obtain a greater understanding of the phenomenon.

The residual stress analysis revealed compressive stresses at low cutting speeds for each grade and depth of cut, becoming more tensile in nature with an increase in cutting speed. Larger stresses are recorded for Grade 5 as opposed to Grade 4 and an increase in depth of cut results in more compressive residual stresses. At cutting speeds of approximately 110 m/min

and 145 m/min for a 0.25 mm cut on Grade 4 and Grade 5 respectively, the compressive stresses change to tensile stresses and residual stresses at these points are close to zero. The significantly lower tensile transition temperature obtained by Puerta Velasquez *et al.* [17] of ±90 m/min suggests that this transition temperature is fundamentally a function of the on-going heat transfer process during machining. The tensile transition temperature is therefore a function of the cooling rate (cooling techniques employed), the heat production (depth of cut) and the rate of heat production (cutting speed).

Sub-surface microstructural analysis revealed a change in grain deformation near the machined edge. The angle and depth at which the grains were deformed tend to decrease with an increase in cutting speed. The increase in depth of cut for Grade 4 results in decreased deformation angles and depths. The increased depth of cut for Grade 5 however reveals the opposite of increased deformation. Larger deformation angles and depths are also observed for Grade 4.

The decrease in deformation angle and region with increasing cutting speed indicates the influence of strain rate sensitivity which dominates the interaction during machining, including workpiece softening, for the process parameters investigated in this study. The strain rate increases with an increase in cutting speed which leads to a higher yield strength of the alloy. The workpiece material effectively strengthens with an increase in cutting speed and therefore leads to a lower deformation angle and deformation depth. The workpiece softening is limited by the cooling techniques employed allowing for the strain rate sensitivity to be dominant.

In conclusion, machining parameters of cutting speed and depth of cut have a significant effect on the induced residual stresses and sub-surface microstructure of Grade 4 and 5 titanium alloys. The changes in the parameters caused substantial changes in the results, allowing for the possibility of achieving certain material or property outcomes through specific

machining parameters. Further analysis is however still required. Recommendations could include the obtaining and investigating of the chips formed and cutting tools used during machining. Further intermediate cutting speeds and depths of cut could also be analysed to obtain a broader data spectrum and hopefully an enhanced understanding of the phenomenon that is occurring at high cutting speeds.

References

[1] S. J. Oosthuizen, "Titanium: the innovators' metal–Historical," *The Journal of The Southern African Institute of Mining and Metallurgy*, vol. 111, pp. 781-786, Nov. 2011.

[2] R. Motsie, "AN OVERVIEW OF SOUTH AFRICA'S TITANIUM MINERAL," Department of Minerals and Energy, Pretoria, Report R71 ISBN: 978-1-919927-86-2, 2008.

[3] S. NAIDOO, "Nationalisation taken off the table at mining indaba," *Mail & Guardian Online*, Feb. 2012.

[4] N. Odendaal, "Titanium could be a strategic economic driver for SA," *Mining Weekly*, Mar. 2011.

[5] E. O. Ezugwu, "Key improvements in the machining of difficult-to-cut aerospace superalloys," *International Journal of Machine Tools & Manufacture*, no. 45, p. 1353–1367, Mar. 2005.

[6] E. O. Ezugwu and Z. M. Wang, "Titanium alloys and their machinability - a review," *Journal of Materials Processing Technology*, no. 68, pp. 262-274, 1997.

[7] ©saetra Pty (Ltd). (2012) SAETRA Pty (Ltd), South Africa - Importers, Exporters and Distributors. [Online]. http://www.saetra.co.za/products/titanium.html

[8] J. R. Myers, H. B. Bomberger, and F. H. Froes, *Journal of Materials*, vol. 36, no. 10, pp. 50-60, 1984.

[9] F. H. Hayes, H. B. Bomberger, F. H. Froes, L. Kaufman, and H. M. Butte, *Journal of Materials*, vol. 36, no. 6, pp. 970-976, 1984.

[10] S. Lei and W. Liu, "High-speed machining of titanium alloys using the driven rotary tool," *International Journal of Machine Tools & Manufacture*, no. 42, p. 653–661, 2002.

[11] Z. Y. Wang and K. P. Rajurkar, "Cryogenic machining of hard-to-cut materials," *Wear*, no. 239, pp. 168-175, 2000.

[12] H. Hong, A. T. Riga, J. M. Cahoon, and C. G. Scott, *Wear*, no. 162, pp. 34-39, 1993.

[13] J. P. Davim, *Surface Integrity in Machining*, 1st ed. 2010, vol. XII.

[14] G. E. Dieter, *Mechanical Metallurgy, ,* SI Metric ed ed. Singapore: McGraw-Hill Book Company, 1988.

[15] J. W. H. John, W. H. Pricea, and e. al., "Comparison of experimental and theoretical residual stresses in welds: The issue of gauge volume," *International Journal of Mechanical Sciences*, vol. 50, pp. 513-521, Sep. 2008.

[16] A. Paradowska, J. W. H. Price, R. Ibrahim, and T. Finlayson, "A neutron diffraction study of residual stress due to welding," *Journal of Materials Processing Technology*, pp. 1099-1105, 2005.

[17] J. D. Puerta Velásquez, A. Tidu, B. Bolle, P. Chevrier, and J.-J. Fundenberger, "Sub-surface and surface analysis of high speed machined Ti–6Al–4V alloy," *Materials Science and Engineering*, vol. A, no. 527, p. 2572–2578, 2010.

[18] M. Freemantle, "Titanium Extracted Directly from TiO2," *Chemical and Engineering News*, Sep. 2000.

[19] W. M. Haynes, *Handbook of Chemistry and Physics*, 91st ed. Taylor and Francis Group, LLC, 2010.

[20] C. R. Dandekar, Y. C. Shin, and J. Barnes, "Machinability improvement of titanium alloy (Ti-6Al-4V) via LAM and hybrid machining," *International Journal of Machine Tools & Manufacture*, no. 50, pp. 174-182, 2010.

[21] D. Ulutan and T. Ozel, "Machining induced surface integrity in titanium and nickel alloys: A review," *International Journal of Machine Tools & Manufacture*, vol. 51, no. 3, pp. 250-280, Mar. 2011.

[22] M. Sima and T. Ozel, "Modified material constitutive models for serrated chip formation simulations and experimental validation in machining of titanium alloy Ti-6Al-4V," *International Journal of Machine Tools & Manufacture*, vol. 50, pp. 943-960, 2010.

[23] P. E. Markovskya and S. L. Semiatin, "Microstructure and mechanical properties of commercial-purity titanium after rapid (induction) heat treatment," *Journal of Materials Processing Technology*, no. 210, pp. 518-528, 2010.

[24] A. Elrefaey and W. Tillmann, "Correlation between microstructure, mechanical properties, and brazing temperature of steel to titanium joint," *Journal of Alloys and Compounds*, no. 487, pp. 639-645, 2009.

[25] J. ,. W. D. Callister, *Materials Science and Engineering an Introduction*, Seventh Edition ed. John Wiley & Sons, Inc., 2007.

[26] E. O. Ezugwu, J. Bonney, and Y. Yamane, "An Overview of the Machinability of Aeroengine Alloys," *Journal of Materials Processing Technology*, no. 134, pp. 233-253, 2002.

[27] Titanium Alloys – Alpha, Beta & Alpha-Beta Alloys. [Online]. http://www.azom.com/details.asp?ArticleID=915

[28] (2008) Titanium Alloy Properties. [Online]. http://www.roymech.co.uk/Useful_Tables/Matter/Titanium.html

[29] R. Boyer, G. Welsch, and E. W. Collings, *Materials Properties Handbook: Titanium Alloys*. ASM International, Materials Park, OH, 1994.

[30] N. Mitsuo, "Mechanical properties of biomedical titanium alloys," *Materials Science and Engineering*, no. A243, pp. 231-236, 1998.

[31] G. Purceka, G. G. Yapicib, I. Karaman, and H. J. Maier, "Effect of commercial purity levels on the mechanical properties of ultrafine-grained titanium," *Materials Science and Engineering A*, no. 528, pp. 2303-2308, 2011.

[32] Titanium Information Group. (2009) Titanium Alloys – Ti6Al4V Grade 5. [Online]. http://www.azom.com/details.asp?ArticleID=1547

[33] M. Vosough, "Effect of High-pressure Cooling on the Residual Stresses in Ti-alloys during Machining," Lulea University of Technology Doctoral Dissertation, 2005.

[34] ASM Handbook Committee, ASM-International, "Materials Characterization," in *Metals Handbook*, vol. 10.

[35] S. D. Suneel, "Characterization and tools," in *Nanotechnology*. .

[36] University of Dayton Research Institute. University of Dayton Research Institute. [Online]. http://www.udri.udayton.edu/StructuralIntegrity/IMMC/Pages/home.aspx

[37] ASTM International. ASTM International Standards Worldwide. [Online]. http://www.astm.org/Standards/E9.htm

[38] K. Bałdys. Instytut Nauki o Materialach. [Online]. http://www.inom.us.edu.pl/index.php?id=galeria&w=1

[39] Advanced Plastic and Material Testing, Inc. APM testing. [Online]. http://www.apmtesting.com/testing-services/test-methods/ASTM-E384.php

[40] Gordon England. Science Engineering Forum. [Online]. http://www.gordonengland.co.uk/hardness/microhardness.htm

[41] Newage Testing Instruments, Inc. Microhardness Testing (Vickers & Knoop). [Online]. http://www.newageinstruments.com/microhardness.htm

[42] J. Mackerle, "Finite-element analysis and simulation of machining: a bibliography (1976–1996)," *Journal of Materials Processing Technology*, no. 86, pp. 17-44, 1999.

[43] J. L. H. Talón, J. C. C. Ortega, C. L. Gómez, E. R. Sancho, and E. F. Olmos, "Manufacture of a spur tooth gear in T-6Al-4V alloy by

electrical discharge," *Computer-Aided Design*, no. 42, pp. 221-230, 2010.

[44] A. Ntasia, W. D. Mueller, G. Eliadesa, and S. Zinelis, "The effect of Electro Discharge Machining (EDM) on the corrosion resistance of dental alloys," *dental materials*, no. 26, pp. e237-e245, 2010.

[45] N. M. Abbas, D. G. Solomon, and M. F. Bahari, "A review on current research trends in electrical discharge machining (EDM)," *International Journal of Machine Tools & Manufacture*, no. 47, pp. 1214-1228, 2007.

[46] H. C. Tsai, B. H. Yan, and F. Y. Huang, "EDM performance of Cr/Cubased composite electrodes," *International Journal of Machining Tools Manufacture*, vol. 43, no. 3, pp. 245-252, 2003.

[47] C. J. Luis, I. Puertas, and G. Villa, "Material removal rate and electrode wear study on the EDM of silicon carbide," *Journal of Materials Processing Technology*, vol. 164-165, pp. 889-896, 2005.

[48] J. Marafona and J. A. G. Chousal, "A finite element model of EDM based on the Joule effect," *International Journal of Machine Tools & Manufacture*, vol. 46, pp. 1-8, 2005.

[49] B. Bojorquez, R. T. Marloth, and O. S. Es-Said, "Formation of a crater in the workpiece on an electrical discharge machine," *Engineering Failure Analysis*, vol. 9, pp. 93-97, 2002.

[50] E. I. Shobert, "What happens in EDM," *Electrical Discharge Machining: Tooling, Methods and Applications, Society of Manufacturing Engineers*, pp. 3-4, 1983.

[51] G. Boothroyd and A. K. Winston, "Non-conventional machining processes," in *Fundamentals of Machining and Machine Tools*. New York: Marcel Dekker, Inc, 1989, p. 491.

[52] J. A. McGeough, "Electrodischarge machining," in *Advanced Methods of Machining*. Chapman & Hall, 1988, p. 130.

[53] S. F. Krar and A. F. Check, "Electrical discharge machining," in

Technology of Machine Tools. New York: Glencoe/McGraw-Hill, 1997, p. 800.

[54] K. H. Ho and S. T. Newman, "State of the art electrical discharge machining (EDM)," *International Journal of Machine Tools & Manufacture*, vol. 43, p. 1287–1300, 2003.

[55] H. Ramasawmy and L. Blunt, "Effect of EDM process parameters on 3D surface topography," *Journal of Materials Processing Technology*, vol. 148, p. 155–164, 2004.

[56] R. H. Todd, D. K. Allen, and L. Alting, *Manufacturing Processes Reference Guide*. Industrial Press Inc., 1994.

[57] P. Byrne, *Turning, Milling and Grinding Processes, Technology Series*. Great Britain: Gray Publishing, 1996.

[58] C. F. Wyen and K. Wegener, "Influence of cutting edge radius on cutting forces in machining titanium," *CIRP Annals - Manufacturing Technology*, no. 59, pp. 93-96, 2010.

[59] C. C. Chen, *Journal of Materials*, vol. 34, no. 11, pp. 30-35, 1982.

[60] D. Eylon, F. H. Froes, and R. W. Gardiner, *Journal of Materials*, vol. 35, no. 2, pp. 35-47, 1983.

[61] F. H. Froes and I. R. Pickens, *Journal of Materials*, vol. 36, no. 1, pp. 14-28, 1984.

[62] P. A. Coulon, *ASME*, pp. 57-63, 1993.

[63] G. Abouelmaged, H. P. Buchkremer, E. EI-Magd, and D. Stover, *Journal of Materials Processing Technology*, no. 37, pp. 583-597, 1993.

[64] H. van Kann, *Titanium and Titanium Alloys*. New York, USA: Plenum Press, 1982, vol. I.

[65] J. F. Kahles, M. Field, D. Eylon, and F. H. Froes, *Journal of Materials*, vol. 37, no. 4, pp. 27-35, 1985.

[66] D. A. Stephenson and J. S. Agapiou, *Metal cutting theory and practice*,

2nd ed. New York: Taylor & Francis Group, 2006.

[67] E. O. Ezugwu, R. B. Da Silva, J. Bonney, and A. R. Machado, "The effects of argon-enriched environment in high speed machining of titanium alloy," *Tribology Transactions*, vol. 1, no. 48, pp. 18-23, 2005.

[68] S. Sun, M. Brandt, and M. S. Dargusch, "Thermally enhanced machining of hard-to-machinematerials - A review," *International Journal of Machine Tools & Manufacture*, vol. 50, pp. 663-680, 2010.

[69] S. Basturk, et al., "Titanium machining with new plasma boronized cutting tools," *CIRP Annals - Manufacturing Technology*, no. 59, pp. 101-104, 2010.

[70] A. I. S. Antonialli, A. E. Diniz, and R. Pederiva, "Vibration analysis of cutting force in titanium alloy milling," *International Journal of Machine Tools & Manufacture*, no. 50, pp. 65-74, 2010.

[71] F. Klocke, et al., "Approaches to High-Speed Cutting of Titanium-Based Materials," in *Sixth International Conference on HIGH SPEED MACHINING*, 2007.

[72] P. A. Dearnley and A. N. Grearson, *Materials Science Technology*, no. 2, pp. 47-58, 1986.

[73] S. Motonishi, et al., *Kobelco Tech Rev.*, no. 2, pp. 28-31, 1987.

[74] R. M. Freeman, PhD Thesis, University of Birmingham, UK, 1974.

[75] N. Narutaki, A. Murakoshi, and S. Motonishi, "Ann. CIRP," vol. 32, no. 1, pp. 65-69, 1983.

[76] E. F. Smart and E. M. Trent, "Int. J. Prod. Res.," vol. 13, no. 3, pp. 265-290, 1975.

[77] N. Zlatin, *Modern Math. Shop*, vol. 42, no. 12, pp. 139-144, 1970.

[78] J. F. Kahles, M. Field, D. Eylon, and F. H. Froes, *J. Met.* , vol. 37, no. 4, pp. 27-35, 1985.

[79] W. Konig, "Proc. 47th Meeting of AGARD Structural and Materials

Panel," in *AGARD, CP256*, Florence, 1979, pp. 11-110.

[80] D. C. Kirk, "Tools and dies for industry," in *Proc. Conf. 76/77. Met. Soc.*, London, 1976-7, pp. 77-98.

[81] B. B. Johnson, *Tips on Milling Titanium - and Tools to Do the Job*.

[82] R. Komanduri, "Wear," no. 76, pp. 15-34, 1982.

[83] B. F. von Turkovich and D. R. Durham, "Advanced Processing Methods for Titanium," no. 18, pp. 257-274, 1982.

[84] R. Komanduri and B. F. von Turkovich, "Wear," vol. 62, no. 2, pp. 179-188, 1981.

[85] R. Komanduri and R. H. Brown, *J. Eng. Ind.*, no. 103, pp. 33-51, 1981.

[86] N. H. Cook, *Proc. Symp. Machining and Grinding of Titanium*, pp. 1-7, 1953.

[87] M. C. Shaw, et al.Massachusetts Institute of Technology, MIT report, 1954.

[88] J. L. Waiter, D. W. Skelly, and W. P. Minnear, *Wear*, no. 170, pp. 79-92, 1993.

[89] P. D. Hartung and B. M. Kramer, "Ann. CIRP," vol. 31, no. 1, pp. 75-80, 1982.

[90] H. E. Chandler, *Metals Handbook*. 1978.

[91] J. Kertesz, R. J. Pryor, D. W. Richerson, and R. A. Cutler, "J. Met.," vol. 40, no. 5, pp. 50-51, 1988.

[92] M. Lee, *Adv. Process. Meth. Titanium*, no. 18, pp. 275-287, 1982.

[93] P. L. N. L. de Lacalle, "High Performance Machining," University of the Basque Country, Faculty of Engineering of Bilbao, Spain, 2008.

[94] (2007) High Speed Machining Tutorials. [Online]. http://highspeedmachining.mae.ufl.edu/htmlsite/tutorial_files

[95] R. Sonnekus, Z. Katz, and R. F. Laubscher, "Studies on High Speed Machining of Titanium Alloys," in *6th CIRP International Conference on Intelligent Computation in Manufacturing Engineering - CIRP ICME'08*, Naples, Italy, 2008.

[96] R. C. Dewes, E. Ng, K. S. Chua, P. G. Newton, and D. K. Aspinwall, "Temperature measurement when high speed machining hardened mould/die steel," *Journal of Materials Processing Technology*, vol. 92-93, pp. 293-301, 1999.

[97] H. Schulz and T. Moriwaki, "High-Speed Machining," *Annals of the CIRP*, vol. 41, no. 2, pp. 637-643, 1992.

[98] M. Rahman, Z. Wang, and Y. Wong, "A Review on High-speed Machining of Titanium Alloys," *JSME International Journal*, vol. 49, no. 1, pp. 11-20, 2006.

[99] R. Pasko, L. Przybylski, and B. Slodki. (2002) High Speed Machining (HSM) – The Effective Way of Modern Cutting. International Workshop CA Systems and Technologies.

[100] T. Kitagawa, A. Kubo, and K. Maekawa, "Temperature and Wear of Cutting tools in High-speed Machining of Inconel 718 and Ti-6Al-6V-2Sn," *Wear*, no. 202, pp. 142-148, 1997.

[101] G. E. Dieter, *Mechanical Metallurgy*, SI Metric ed. Singapore: McGraw-Hill Book Company, 1988.

[102] TWI Ltd. (2000) Residual Stresses (Knowledge Summary). [Online]. http://www.twi.co.uk/content/weldasearch.html

[103] P. J. Withers, "Mapping Residual and Internal Stress in Materials by Neutron Diffraction," *Neutron scattering/Diffusion de neutrons*, no. 8, pp. 806-820, Nov. 2007.

[104] Metallurgical Consultants. (2007, Sep.) Residual Stresses. [Online]. http://www.materialsengineer.com/residual-stresses.htm

[105] G. A. Webster and R. C. Wimpory, "Residual stress in weldments,"

Journal of Neutron Research, vol. 9, p. 281–287, 2001.

[106] E. Brinksmeiera, et al., "Measurement and Causes in Machining Processes," *CIRP Annals - Manufacturing Technology*, vol. 31, no. 2, pp. 491-510, 1982.

[107] Z. Barsoum and A. Lundbäck, "Simplified FE welding simulation of fillet welds – 3D effects on the formation residual stresses," *Engineering Failure Analysis*, no. 16, p. 2281–2289, Mar. 2009.

[108] P. J. Withers and H. K. D. H. Bhadeshia, *Materials Science and Technology*. Maney Publishing, 2001, vol. 17.

[109] H. Alberg and D. Berglund, "Comparison of plastic, viscoplastic, and creep models when modeling welding and stress relief heat treatment," *Comp. Meth. Appl. Mech. Eng.*, vol. 192, pp. 5189-5208, 2003.

[110] A. G. Olabi and M. S. J. Hashmi, "Effects of the stress-relief conditions on a martensite stainless-steel welded component," *J. Mater. Process. Technol.*, vol. 77, pp. 216-225, 1998.

[111] P. Sedek, J. Brozda, L. Wang, and P. J. Withers, "Residual stress relief in MAG welded joints of dissimilar steels," *Int. J. Pressure Vessels Piping*, vol. 80, pp. 705-713, 2003.

[112] X. Cheng, J. W. Fisher, H. J. Prask, T. Gnäupel-Herold, and B. T. Yen, "Residual stress modification by post-weld treatment and its beneficial effect on fatigue strength of welded structures," *Int. J. Fatigue*, vol. 25, pp. 1259-1269, 2003.

[113] Joomla Nation. Residual Stress. [Online]. http://www.residualstress.org/pages/home

[114] R. S. Pawade, S. S. Joshi, and P. K. Brahmankar, "Effect of machining parameters and cutting edge geometry on surface integrity of high-speed turned Inconel 718," *International Journal of Machine Tools & Manufacture*, vol. 48, p. 15–28, 2008.

[115] J. Sun and Y. B. Guo, "A comprehensive experimental study on surface

integrity by end milling Ti-6Al-4V," *Journal of Materials Processing Technology*, vol. 209, pp. 4036-4042, 2009.

[116] A. L. Mantle and D. K. Aspinwall, "Surface Integrity of a High Speed Milled Gamma Titanium Aluminide," *Journal of Materials Processing Technology*, vol. 118, pp. 143-150, 2001.

[117] J. J. Klopper, "An investigation into the effect of weld induced residual stresses on the structural behaviour of built-up 3CR12 columns," University of Johannesburg Doctoral Thesis, 2009.

[118] S. Murugan, et al., "Temperature distribution and residual stresses due to multipass welding in type 304 stainless steel and low carbon steel weld pads," *International Journal of Pressure Vessels and Piping*, vol. 78, pp. 307-317, Feb. 2001.

[119] J. Lu, "Handbook of Measurement of Residual Stresses," *Society for Experimental Mechanics*, 1996.

[120] P. Withers and H. Bhadeshia, "Residual stress - measurement techniques," *Material Science and Technology*, vol. 17, pp. 355-365, 2001.

[121] V. Hauk, "Structural and Residual Stress Analysis by Nondestructive Methods," 1997.

[122] D. Walker, "Residual stress measurement techniques," *Advanced Materials and Processes*, pp. 30-33, 2001.

[123] M. Honner, P. Litos, and M. Svantner, "Thermography analyses of the hole-drilling residual stress measuring technique," *Infrared Physics & Technology*, vol. 45, p. 131–142, 2004.

[124] J. Mathar, "Determination of Initial Stresses by Measuring Deformation Around Drilled Holes," vol. 56, no. 4, pp. 249-254, 1934.

[125] G. Johnson, "Residual stress measurements using the contour method," Ph.D. Thesis, University of Manchester, 2008.

[126] G. S. Schajer, "Hole-drilling and Ring Core Methods," in *Handbook of Measurement of Residual Stresses*. Fairmount Press, 1996.

[127] Stresscraft Ltd. Stresscraft residual stress measurement and stress calculation services. [Online]. http://stresscraft.co.uk/residual_stress_determination.htm

[128] G. S. Schajer, "Measurement of non-uniform residual stresses using the hole-drilling method," *Journal of Engineering Materials and Technology*, vol. 110, pp. 338-343, 1988.

[129] M. A. Sutton, S. R. McNeil, J. D. Helm, and Y. J. Chao, "Advances in 2D and 3D computer vision for shape and deformation measurements," *Photomechanics*, 2000.

[130] C. Herbst and K. Splitthof, *Basics of 3D Digital Image Correlation*.

[131] T. Becker, K. Splitthof, T. Siebert, and P. Kletting, "Error Estimations of 3D Digital Image Correlation Measurements," in *The International Conference Speckle06*, Nimes, France, 2006.

[132] C. O. Ruud, "Residual Stress Measurement," in *Analytical Characterization of Aluminium, Steel, and Superalloys*, 2006.

[133] National Physical Library (2007) Technique Information. [Online]. http://www.npl.co.uk/materials/residualstress/technique_information.html

[134] M. Vosough, "Effect of High-pressure Cooling on the Residual Stresses in Ti-alloys during Machining," Lulea University of Technology Doctoral Dissertation, 2005.

[135] Ceram and Pepper Digital. (2011) Microstructural Analysis. [Online]. http://www.ceram.com/testing-analysis/microstructural-analysis/

[136] Optical Microscope. [Online]. http://www.sccs.swarthmore.edu/users/08/ajb/tmve/wiki100k/docs/Optical_microscope.html

[137] University of Sao Paulo. LFF Optical microscope. [Online]. http://fap.if.usp.br/~lff/moE.html

[138] S. Swapp. (2011, Jun.) University of Wyoming: Geochemical Instrumentation and Analysis. [Online]. http://serc.carleton.edu/research_education/geochemsheets/techniques/SEM.html

[139] N. Fang and Q. Wu, "A comparative study of the cutting forces in high speed machining of Ti–6Al–4V and Inconel 718 with a round cutting edge tool," *Journal of Materials Processing Technology*, no. 209, p. 4385–4389, 2009.

[140] Z. G. Wang, Y. S. Wong, and M. Rahman, "High-speed milling of titanium alloys using binderless CBN tools," *International Journal of Machine Tools & Manufacture*, no. 45, p. 105–114, 2005.

[141] M. Calamaz, D. Coupard, and F. Girot, "A new material model for 2D numerical simulation of serrated chip formation when machining titanium alloy Ti–6Al–4V," *International Journal of Machine Tools & Manufacture*, no. 48, pp. 275-288, 2008.

[142] J. Goodge. (2011, Jun.) University of Minnesota-Duluth, Energy-Dispersive X-Ray Spectroscopy (EDS). [Online]. http://serc.carleton.edu/research_education/geochemsheets/eds.html

Appendix A: Microhardness Test Results

A TIME MH-6 digital microhardness tester is used to test the microhardness of the investigated Grade 4 and 5 titanium alloys. Several measurements are taken for each sample as described in Section 3.2. The results are recorded in Tables A.1 and A.2. The Grade 4 hardness of 273.9 is substantially lower than Grade 5 with a hardness of 362.3. Grade 5 is therefore a harder and stronger material. The hardness values are also similar in magnitude to the material specification data of 280 and 376 for Grade 4 and 5 respectively.

Table A.1 - Grade 4 Vickers hardness results

Sample #1		**Sample #2**		**Sample #3**	
Reading no.	**Hardness value**	**Reading no.**	**Hardness value**	**Reading no.**	**Hardness value**
1	267.1	**1**	284.1	**1**	275.4
2	274.3	**2**	283.0	**2**	266.1
3	279.7	**3**	274.3	**3**	278.6
4	278.6	**4**	274.3	**4**	273.3
5	270.1	**5**	271.2	**5**	264.1
6	268.1	**6**	279.7	**6**	276.4
7	274.3	**7**	274.3	**7**	272.2
8	280.8	**8**	283.0	**8**	274.3
9	271.2	**9**	268.1	**9**	268.1
10	276.4	**10**	274.3	**10**	281.9
11	277.5	**11**	270.1	**11**	274.3
12	271.2	**12**	273.3	**12**	268.1
13	270.1	**13**	270.1	**13**	274.3
14	283.0	**14**	275.4	**14**	274.3
15	271.2	**15**	268.1	**15**	269.1
Average	274.2	**Average**	274.9	**Average**	272.7
	Final Hardness Value			273.9	

Table A.2 - Grade 5 Vickers hardness results

Sample #1		Sample #2		Sample #3	
Reading no.	**Hardness value**	**Reading no.**	**Hardness value**	**Reading no.**	**Hardness value**
1	355.2	**1**	356.7	**1**	358.3
2	361.5	**2**	366.3	**2**	355.2
3	363.1	**3**	363.1	**3**	358.3
4	361.5	**4**	366.3	**4**	358.3
5	361.5	**5**	358.5	**5**	359.9
6	356.7	**6**	358.3	**6**	366.3
7	356.7	**7**	366.3	**7**	366.3
8	363.1	**8**	366.3	**8**	367.9
9	367.9	**9**	369.6	**9**	372.9
10	356.7	**10**	355.2	**10**	367.9
11	363.1	**11**	361.5	**11**	358.3
12	372.9	**12**	356.7	**12**	367.9
13	366.3	**13**	359.9	**13**	363.1
14	364.7	**14**	367.9	**14**	371.2
15	355.2	**15**	355.2	**15**	358.3
Average	361.7	**Average**	361.9	**Average**	363.3
	Final Hardness Value			362.3	

Appendix B: Compression Test Results

An INSTRON 5500R compression test machine is used to obtain the physical properties of Grade 4 and 5 as described in Section 0. The relevant material properties are extracted and recorded in Tables B.1 and B.2. Stress-strain graphs are generated and presented in Figures B.1 through B.4. Grade 5 is found to be substantially harder and stronger than Grade 4, as depicted in their properties.

Table B.1 - Grade 4 compression test results

Physical properties of Grade 4			
	Sample #1	**Sample #2**	**Average**
Yield strength (Mpa)	565.0	560.0	562.5
Compressive strength (Mpa)	688.8	689.6	689.2
Young's modulus (Gpa)	125.3	126.3	125.8

Table B.2 - Grade 5 compression test results

Physical properties of Grade 5			
	Sample #1	**Sample #2**	**Average**
Yield strength (Mpa)	957.0	980.0	968.5
Compressive strength (Mpa)	1112.2	1110.2	1111.2
Young's modulus (Gpa)	132.7	133.2	133.0

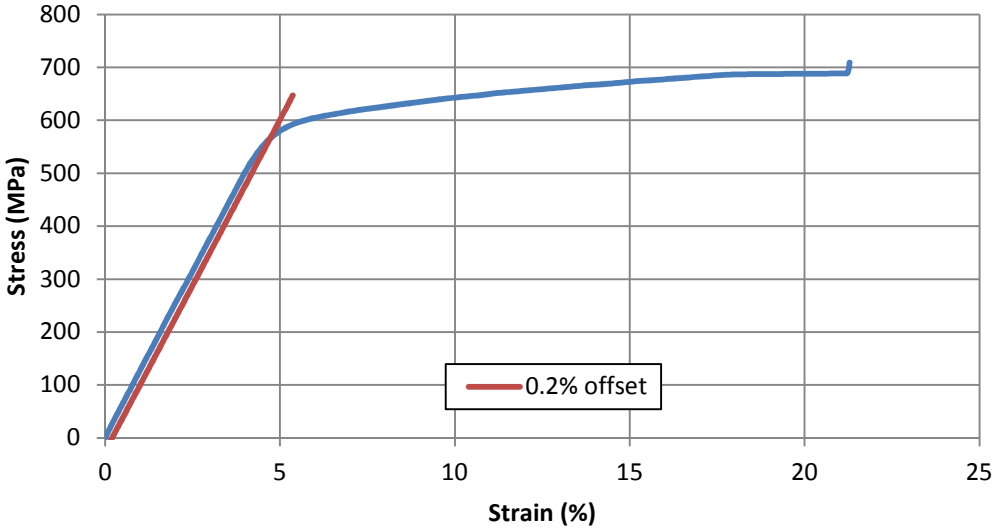

Figure B.1 - Grade 4 stress-strain curve for sample 1

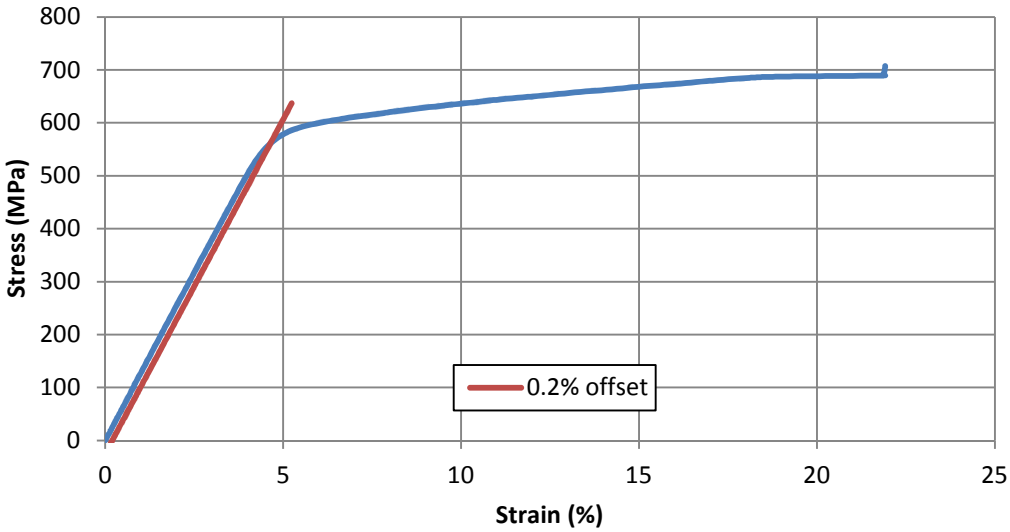

Figure B.2 - Grade 4 stress-strain curve for sample 2

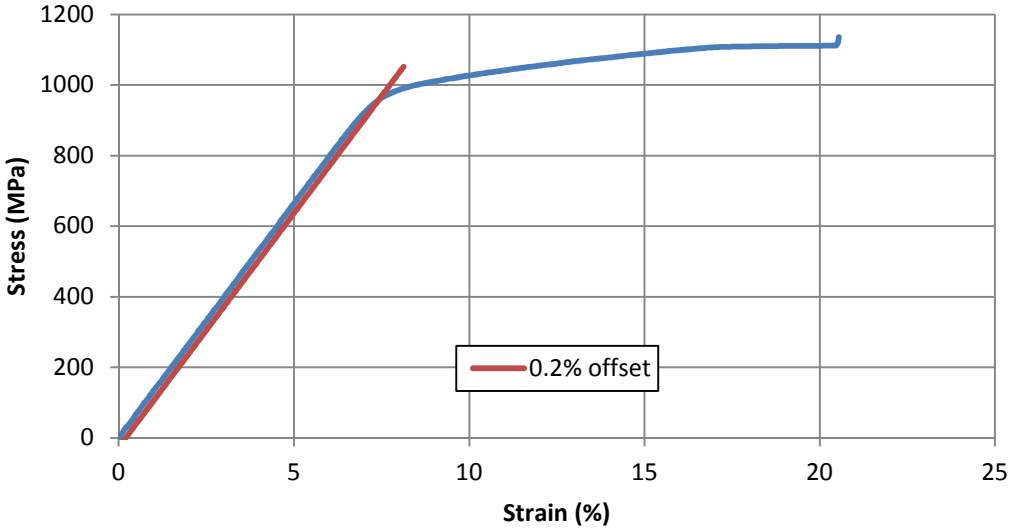

Figure B.3 - Grade 5 stress-strain curve for sample 1

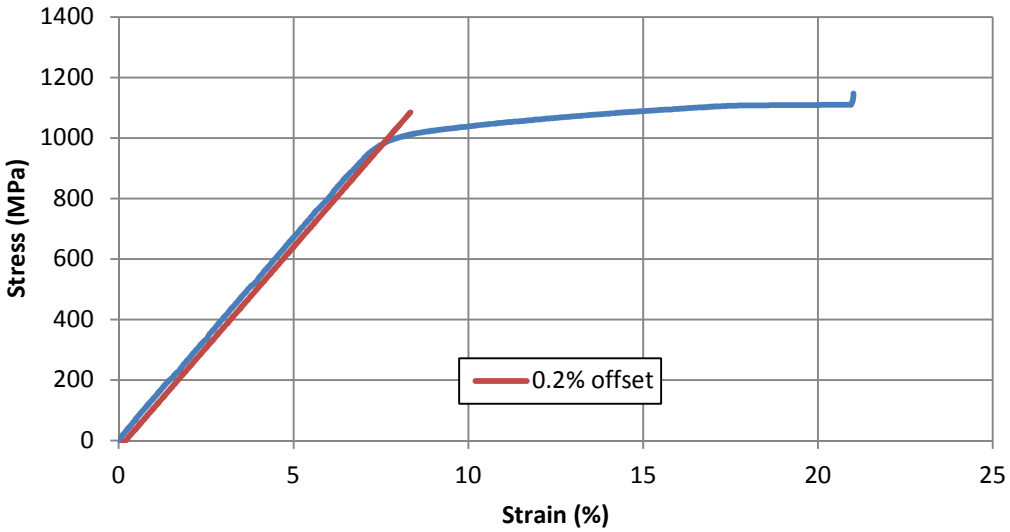

Figure B.4 - Grade 5 stress-strain curve for sample 2

Appendix C: Cutting Tool Temperature Analysis

The temperature at two points on the cutting tool are measured and recorded for each cutting speed and depth of cut. The two points are situated approximately 1 mm and 2 mm from the tool tip edge. From the measurement of these temperature points, the tool tip temperature can be calculated if further analysis of certain samples is required. These temperatures are recorded at a rate of 200 measurements per second. The temperature values reported in this section illustrate the maximum temperatures recorded over the total cut length. The raw data and individual temperature profile graphs are presented in Appendix D.

The variation of cutting temperature as a function of cutting speed for Grade 4 and 5 at different depths of cut is presented in Figures C.1 to C.4. The temperatures remain fairly constant throughout the cutting speed range with no substantial changes observed for most cuts. The temperatures recorded during the 1.00 mm cut on Grade 5 however, display significant rises at the cutting speeds of 150, 175 and 200 m/min. Analysis of the individual temperature profiles for these cuts reveals sudden and dramatic rises in temperature that differ from the other profiles. These increases are due to thermal “run away” as further described in Section 4.2. These temperature profiles are illustrated in Figures D.22 through D.24 of Appendix D.

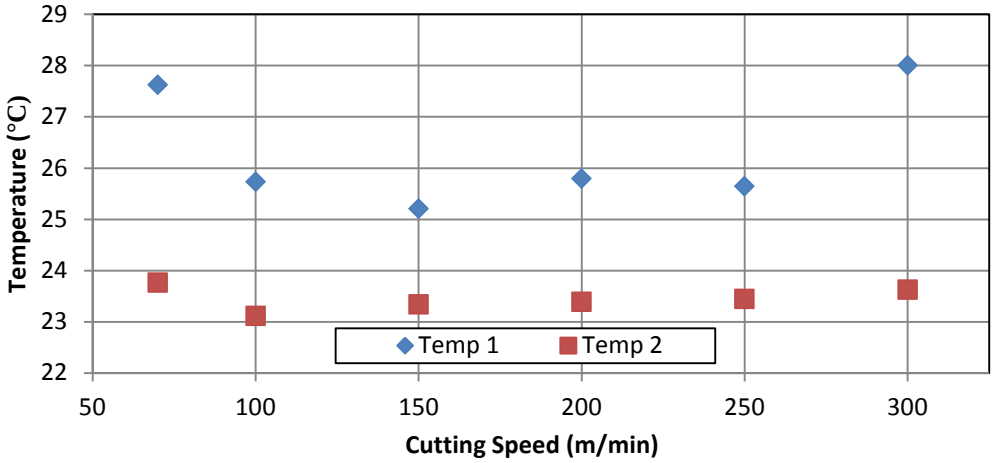

Figure C.1 - Variation of cutting temperature for Grade 4 at 0.25 mm depth of cut

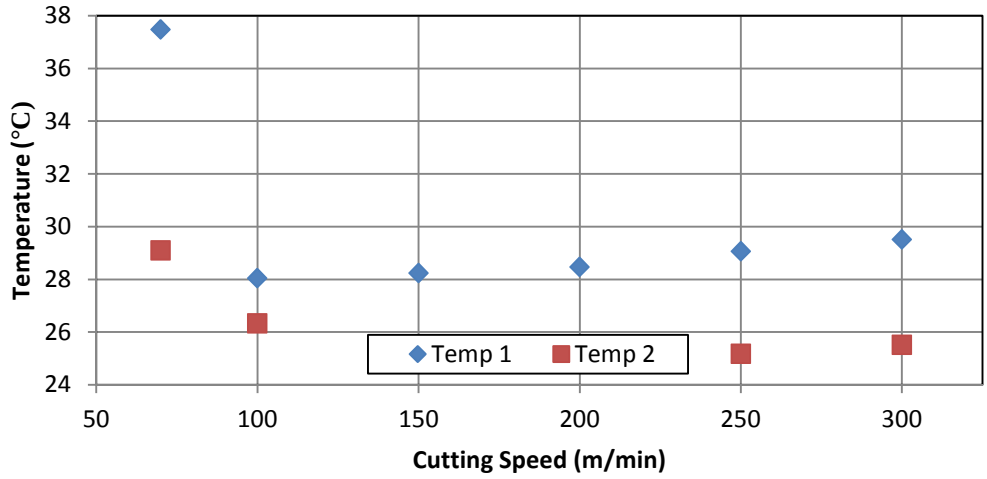

Figure C.2 - Variation of cutting temperature for Grade 4 at 1.00 mm depth of cut

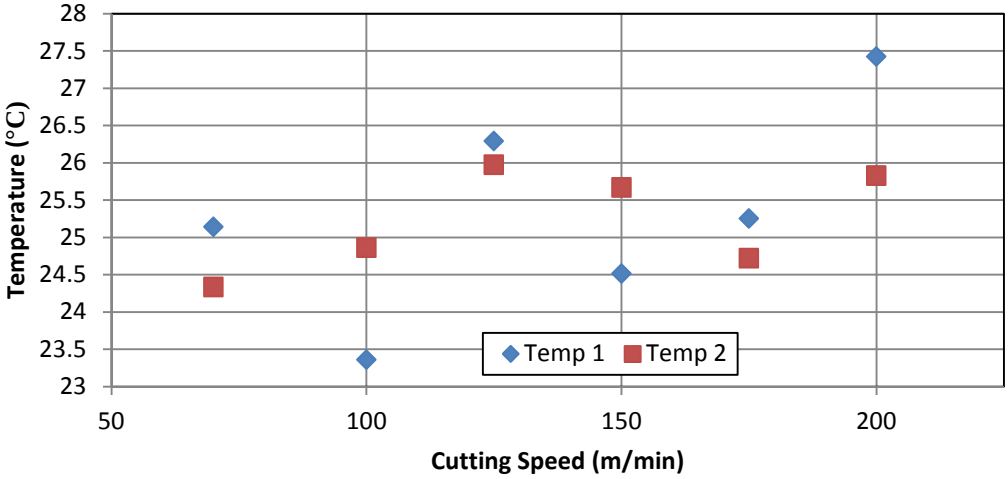

Figure C.3 - Variation of cutting temperature for Grade 5 at 0.25 mm depth of cut

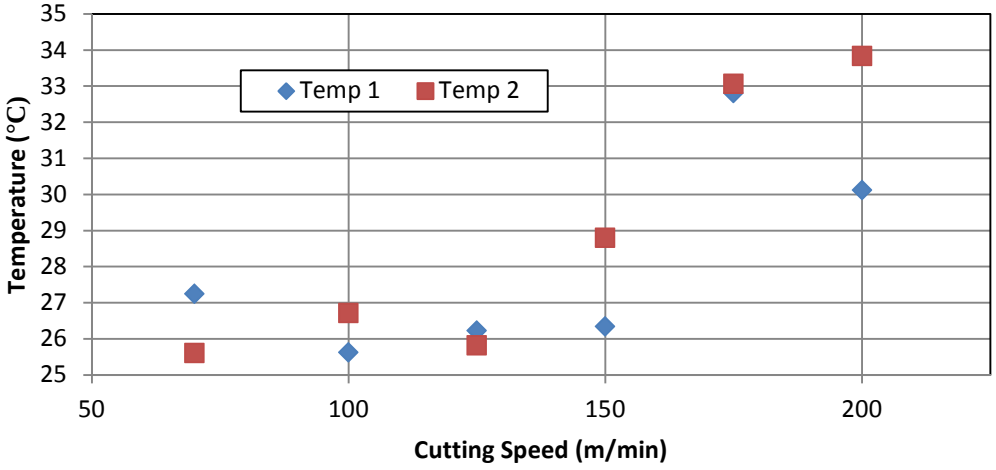

Figure C.4 - Variation of cutting temperature for Grade 5 at 1.00 mm depth of cut

Appendix D: Individual Cutting Tool Temperature Profiles and Extracted Maximum Temperature Data

D.1 Cutting temperature profiles for Grade 4 at 0.25 mm DOC

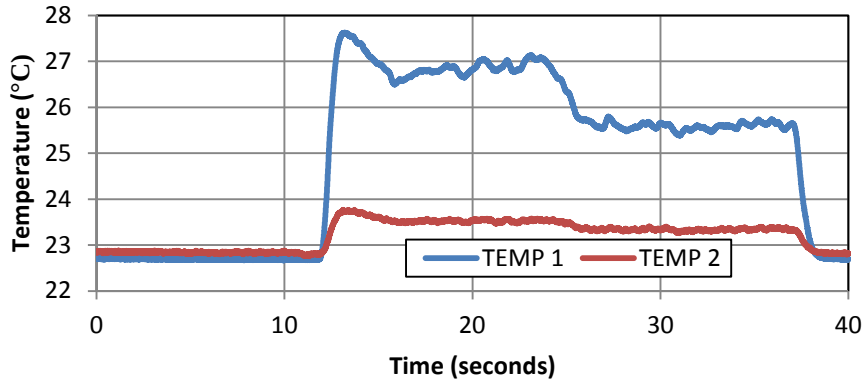

Figure D.1 - Grade 4 cutting temperature profile at 0.25 mm DOC and 70 m/min

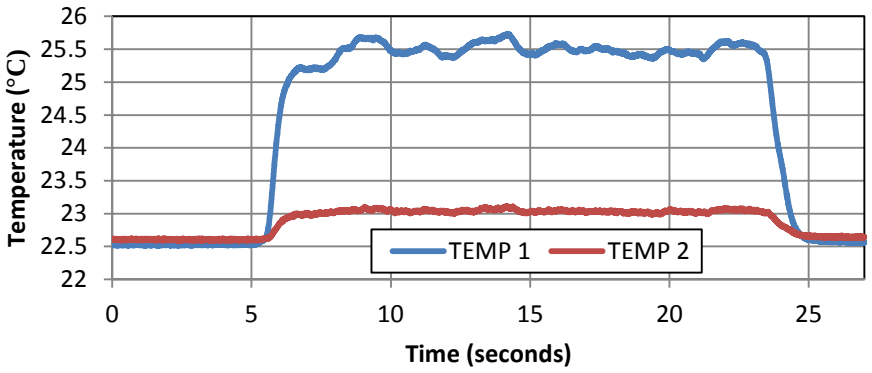

Figure D.2 - Grade 4 cutting temperature profile at 0.25 mm DOC and 100 m/min

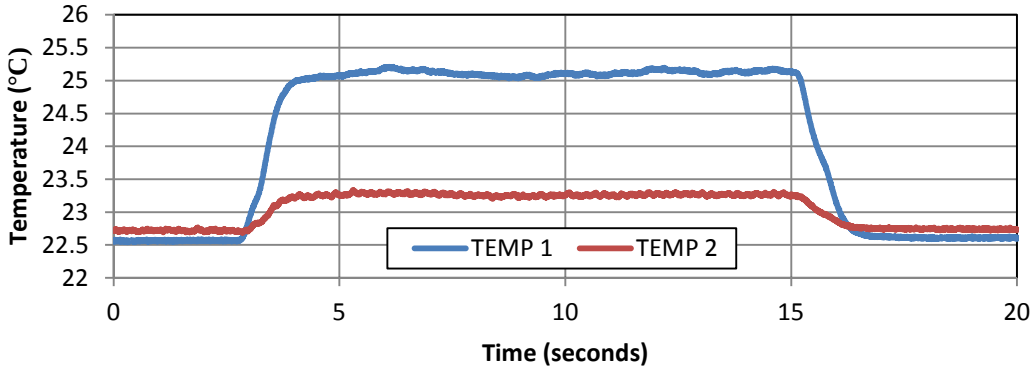

Figure D.3 - Grade 4 cutting temperature profile at 0.25 mm DOC and 150 m/min

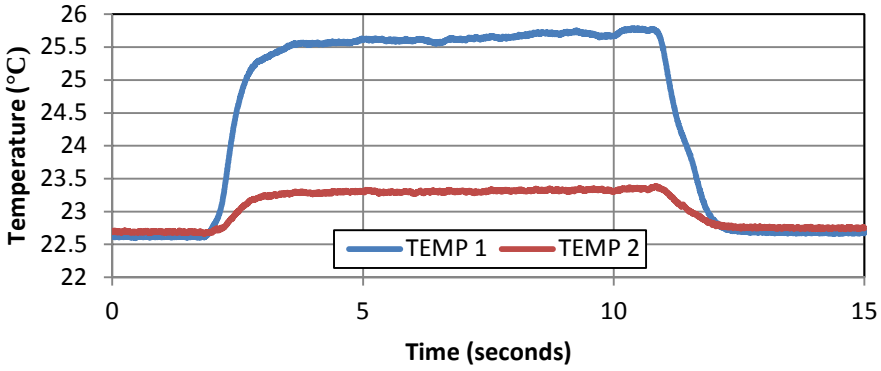

Figure D.4 - Grade 4 cutting temperature profile at 0.25 mm DOC and 200 m/min

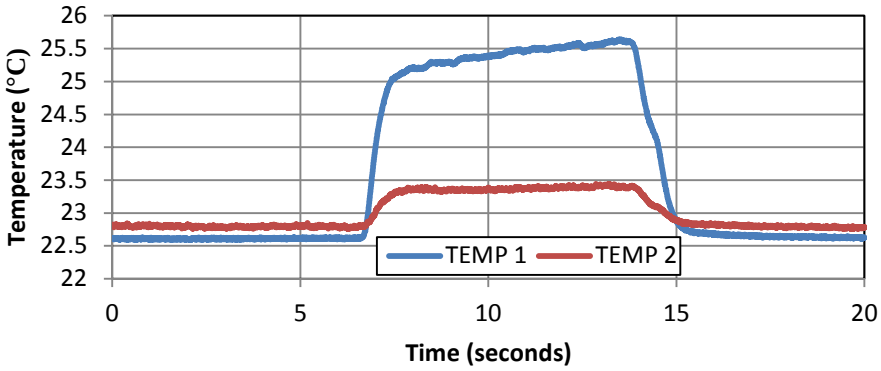

Figure D.5 - Grade 4 cutting temperature profile at 0.25 mm DOC and 250 m/min

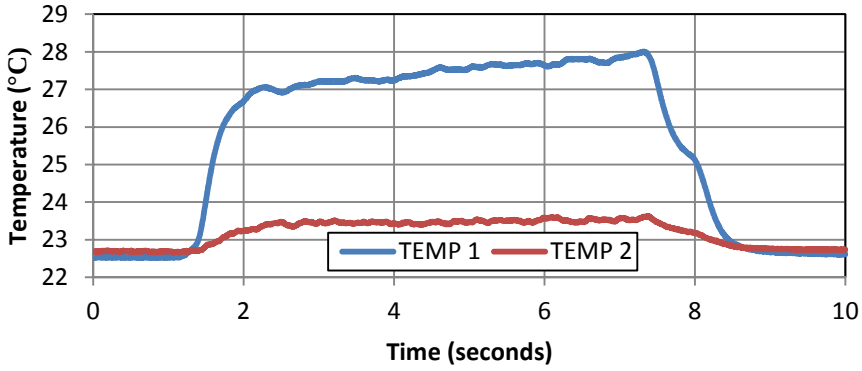

Figure D.6 - Grade 4 cutting temperature profile at 0.25 mm DOC and 300 m/min

D.2 Cutting temperature profiles for Grade 4 at 1.00 mm DOC

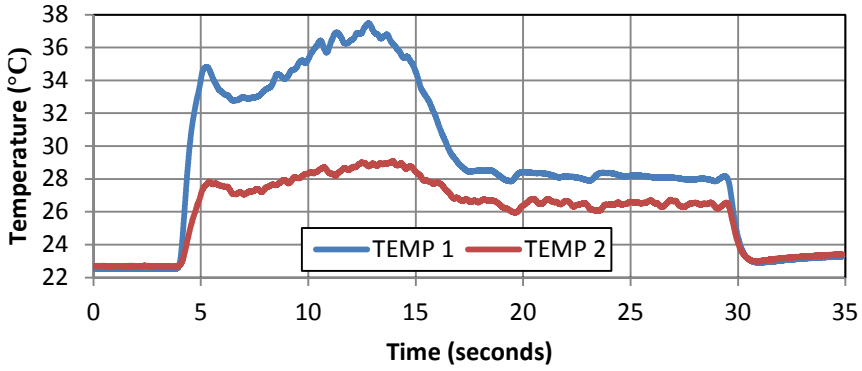

Figure D.7 - Grade 4 cutting temperature profile at 1.00 mm DOC and 70 m/min

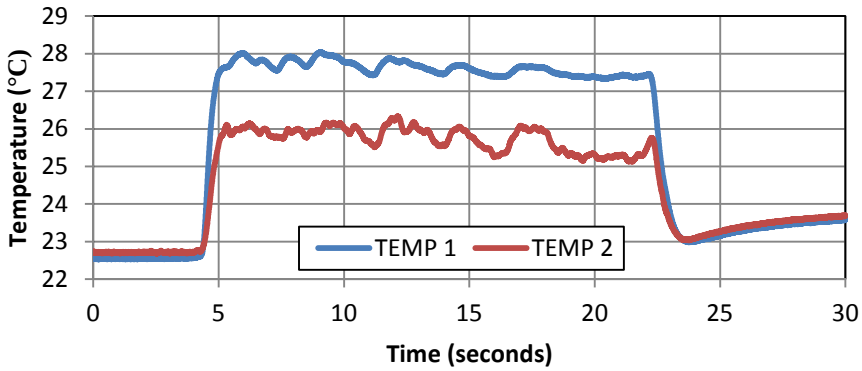

Figure D.8 - Grade 4 cutting temperature profile at 1.00 mm DOC and 100 m/min

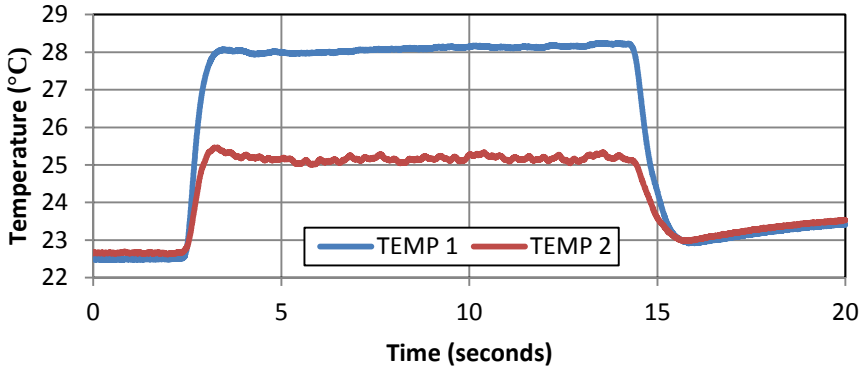

Figure D.9 - Grade 4 cutting temperature profile at 1.00 mm DOC and 150 m/min

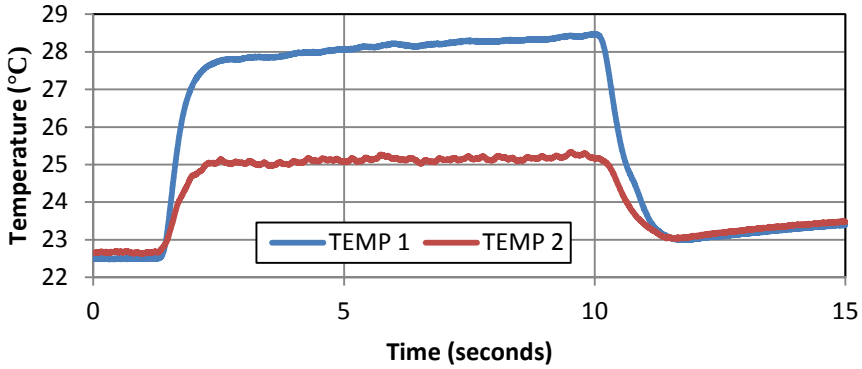

Figure D.10 - Grade 4 cutting temperature profile at 1.00 mm DOC and 200 m/min

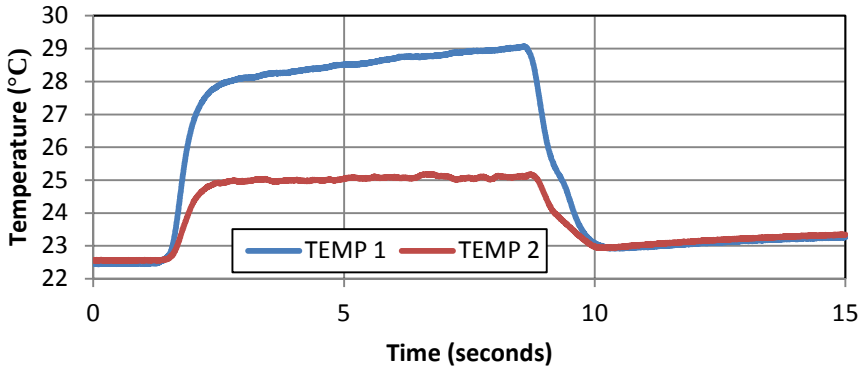

Figure D.11 - Grade 4 cutting temperature profile at 1.00 mm DOC and 250 m/min

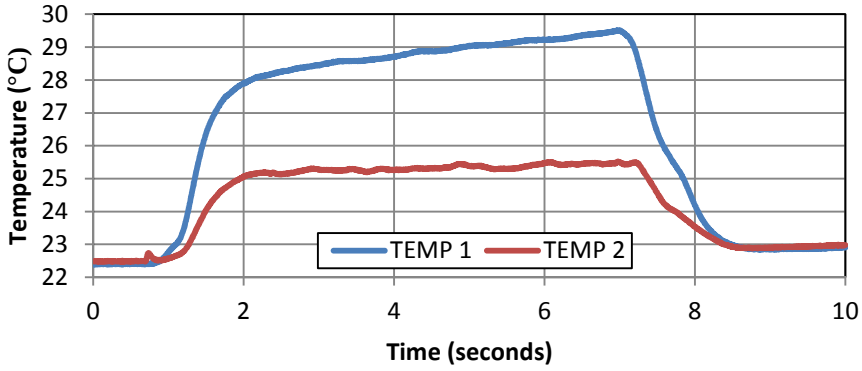

Figure D.12 - Grade 4 cutting temperature profile at 1.00 mm DOC and 300 m/min

D.3 Cutting temperature profiles for Grade 5 at 0.25 mm DOC

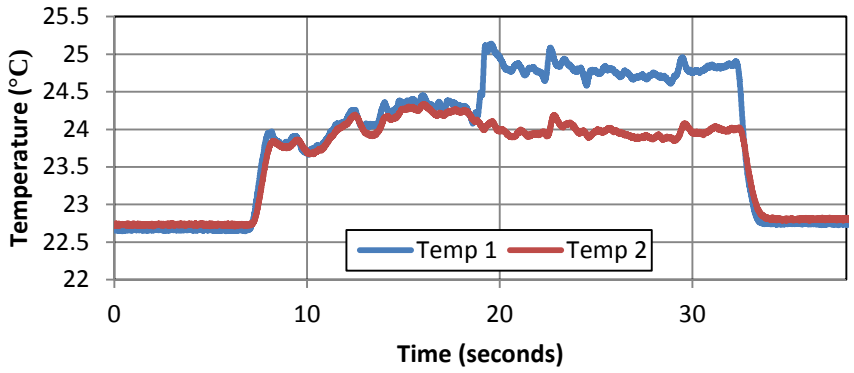

Figure D.13 - Grade 5 cutting temperature profile at 0.25 mm DOC and 70 m/min

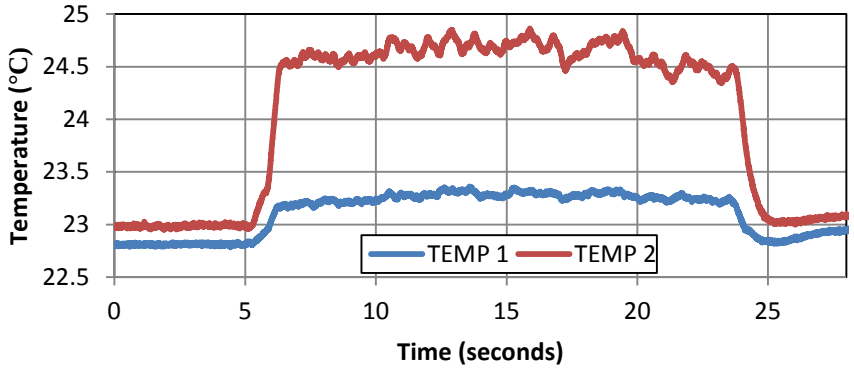

Figure D.14 - Grade 5 cutting temperature profile at 0.25 mm DOC and 100 m/min

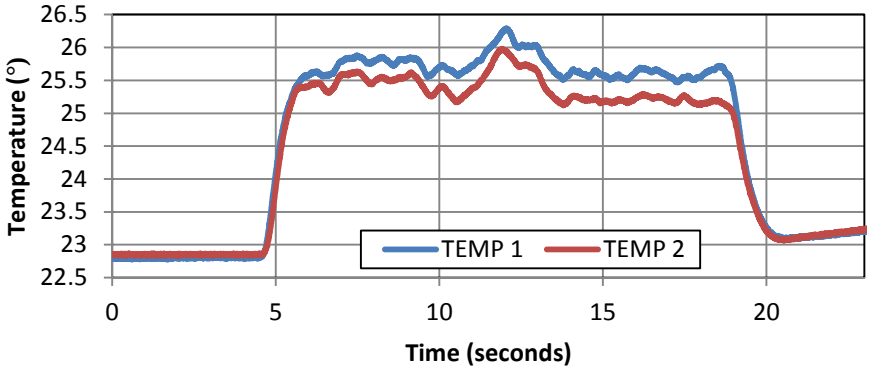

Figure D.15 - Grade 5 cutting temperature profile at 0.25 mm DOC and 125 m/min

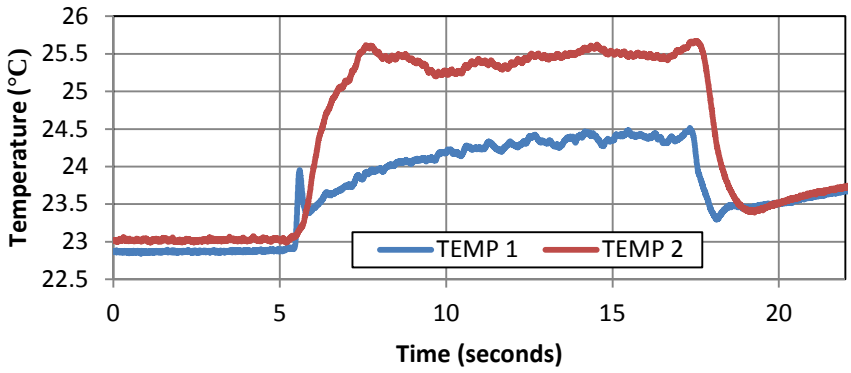

Figure D.16 - Grade 5 cutting temperature profile at 0.25 mm DOC and 150 m/min

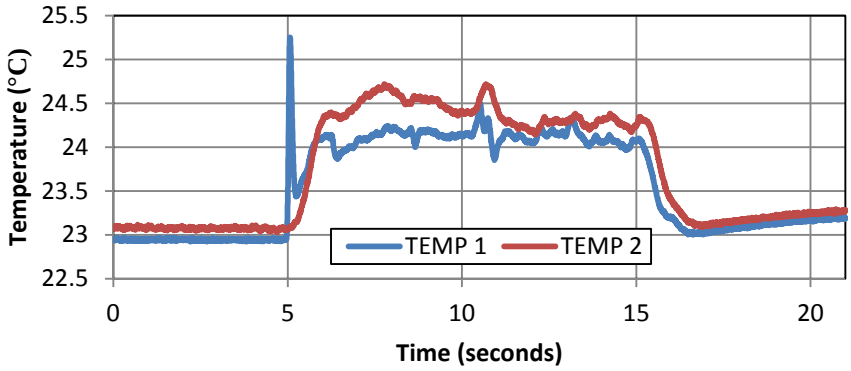

Figure D.17 - Grade 5 cutting temperature profile at 0.25 mm DOC and 175 m/min

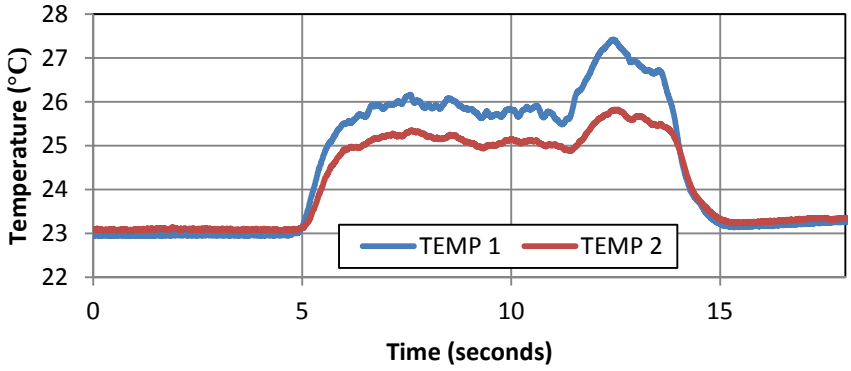

Figure D.18 - Grade 5 cutting temperature profile at 0.25 mm DOC and 200 m/min

D.4 Cutting temperature profiles for Grade 5 at 1.00 mm DOC

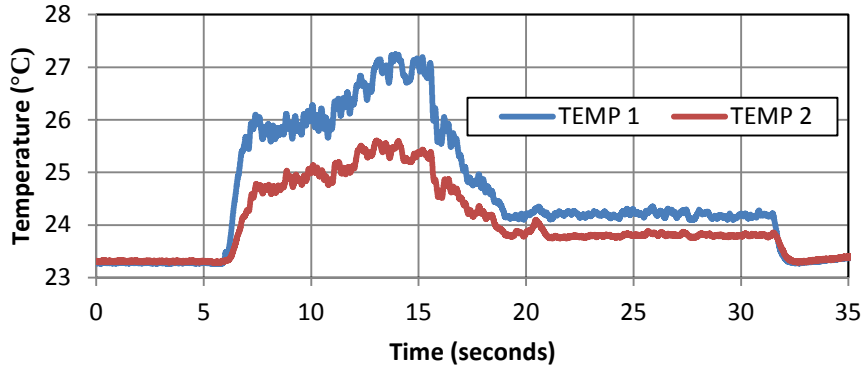

Figure D.19 - Grade 5 cutting temperature profile at 1.00 mm DOC and 70 m/min

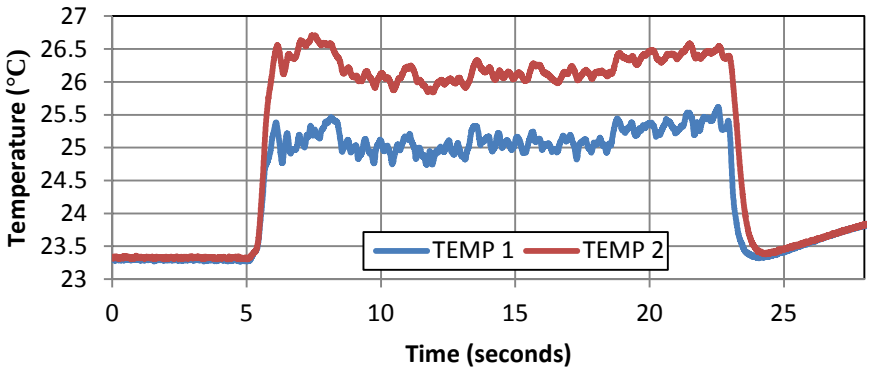

Figure D.20 - Grade 5 cutting temperature profile at 1.00 mm DOC and 100 m/min

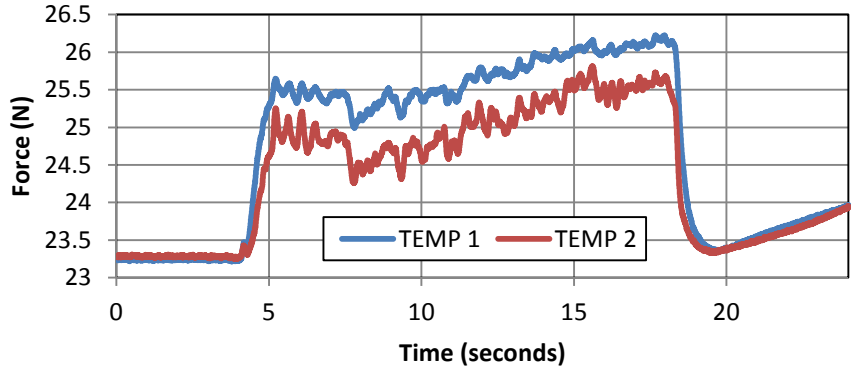

Figure D.21 - Grade 5 cutting temperature profile at 1.00 mm DOC and 125 m/min

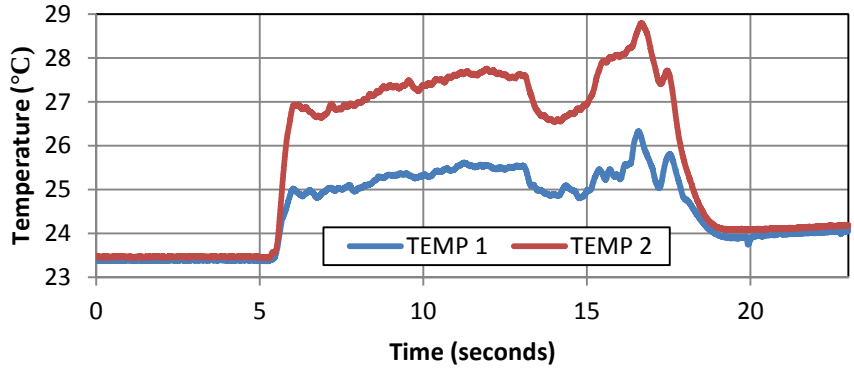

Figure D.22 - Grade 5 cutting temperature profile at 1.00 mm DOC and 150 m/min

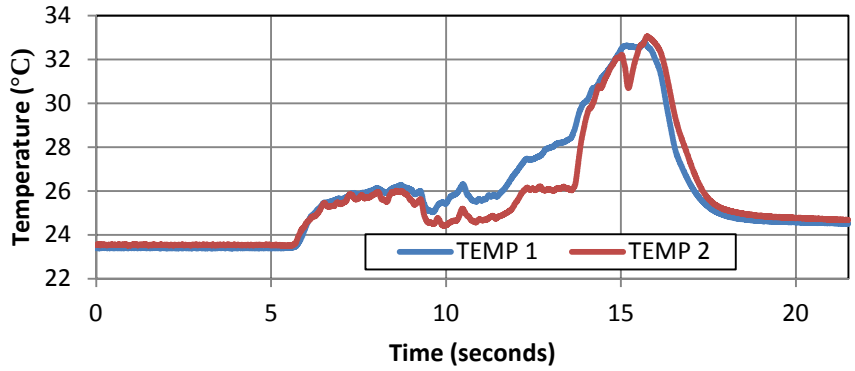

Figure D.23 - Grade 5 cutting temperature profile at 1.00 mm DOC and 175 m/min

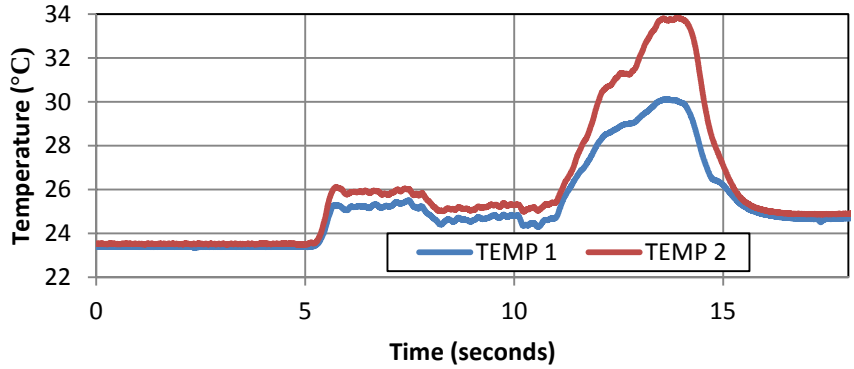

Figure D.24 - Grade 5 cutting temperature profile at 1.00 mm DOC and 200 m/min

D.5 Extracted Grade 4 and 5 maximum cutting temperatures

Table D.1 - Grade 4 maximum cutting temperatures

0.25 mm depth of cut					1.00 mm depth of cut			
		Temp 1 (°C)	Temp 2 (°C)				Temp 1 (°C)	Temp 2 (°C)
Cutting speed (m/min)	70	27.63	23.77		Cutting speed (m/min)	70	37.48	29.10
	100	25.73	23.12			100	28.05	26.33
	150	25.21	23.34			150	28.24	25.46
	200	25.79	23.39			200	28.47	25.34
	250	25.64	23.44			250	29.07	25.18
	300	28.01	23.63			300	29.52	25.52

Table D.2 - Grade 5 maximum cutting temperatures

0.25 mm depth of cut					1.00 mm depth of cut			
		Temp 1 (°C)	Temp 2 (°C)				Temp 1 (°C)	Temp 2 (°C)
Cutting speed (m/min)	70	25.14	24.34		Cutting speed (m/min)	70	27.25	25.61
	100	23.36	24.86			100	25.62	26.71
	150	26.29	25.97			125	26.22	25.81
	200	24.51	25.67			150	26.34	28.80
	250	25.25	24.72			175	32.80	33.06
	300	27.42	25.83			200	30.12	33.84

Appendix E: Individual Cutting Force Profiles and Extracted Cutting Force Data

E.1 Cutting force profiles for Grade 4 at 0.25 mm DOC

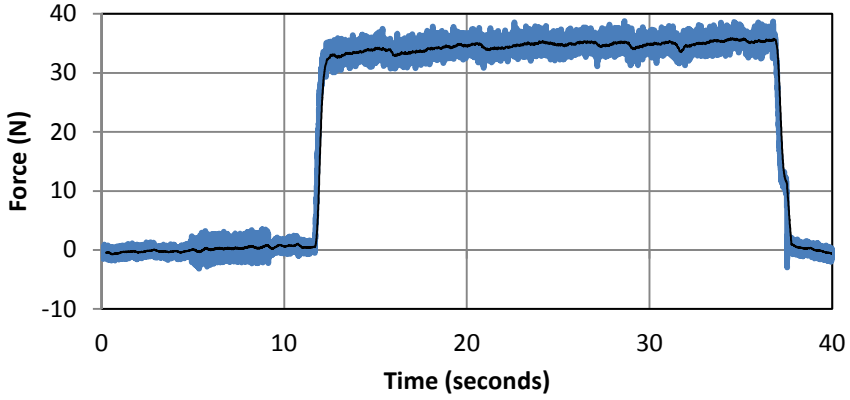

Figure E.1 - Grade 4 x-axis cutting force profile at 0.25 mm DOC and 70 m/min

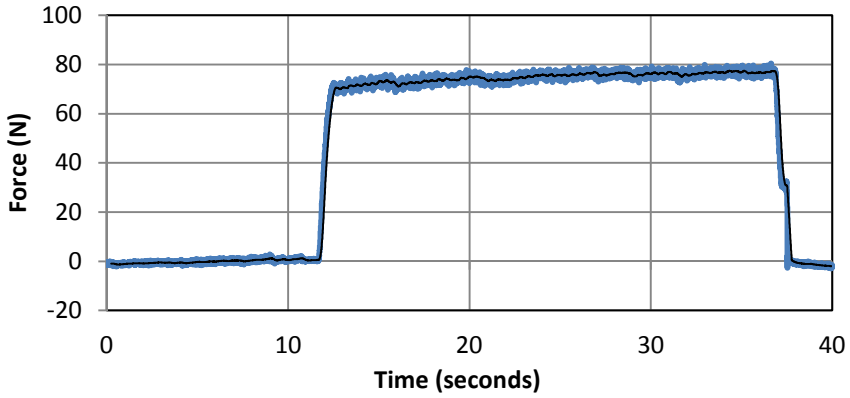

Figure E.2 - Grade 4 y-axis cutting force profile at 0.25 mm DOC and 70 m/min

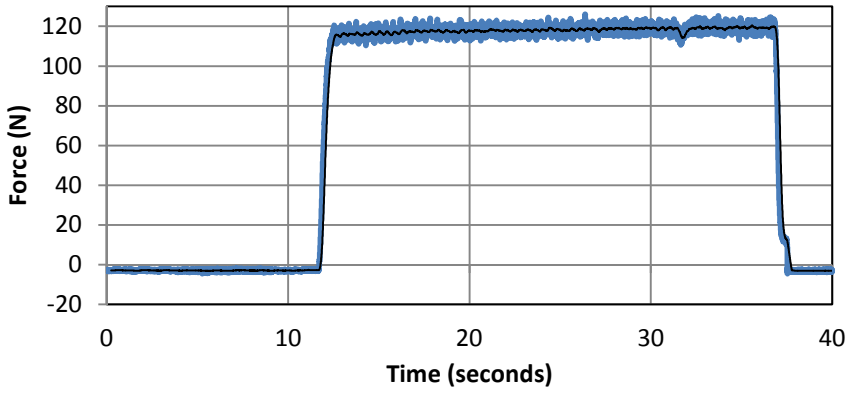

Figure E.3 - Grade 4 z-axis cutting force profile at 0.25 mm DOC and 70 m/min

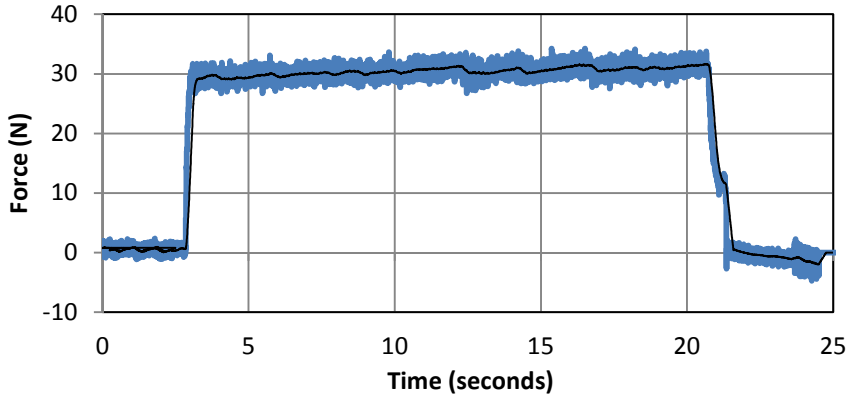

Figure E.4 - Grade 4 x-axis cutting force profile at 0.25 mm DOC and 100 m/min

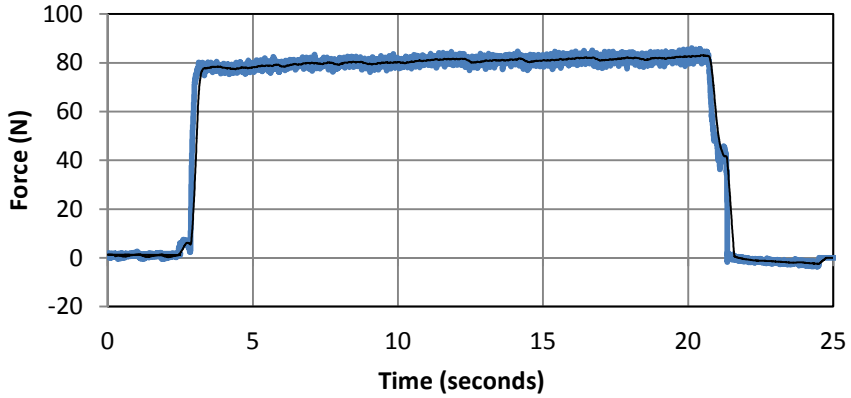

Figure E.5 - Grade 4 y-axis cutting force profile at 0.25 mm DOC and 100 m/min

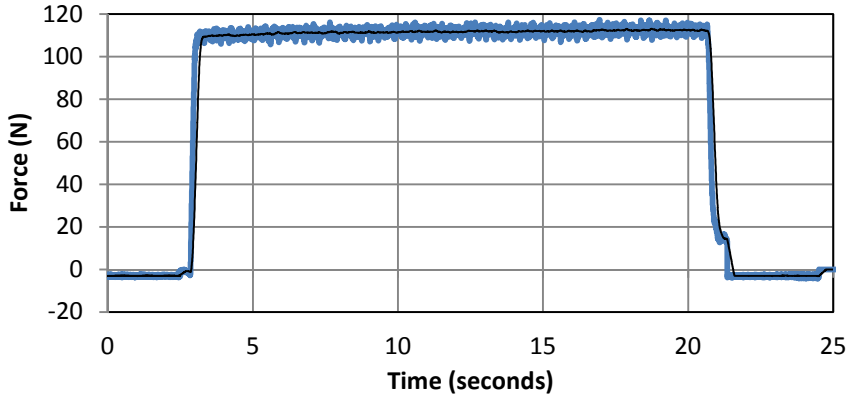

Figure E.6 - Grade 4 z-axis cutting force profile at 0.25 mm DOC and 100 m/min

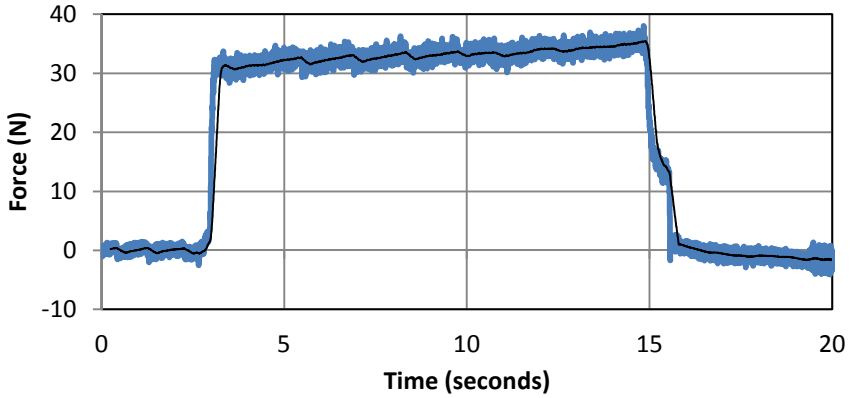

Figure E.7 - Grade 4 x-axis cutting force profile at 0.25 mm DOC and 150 m/min

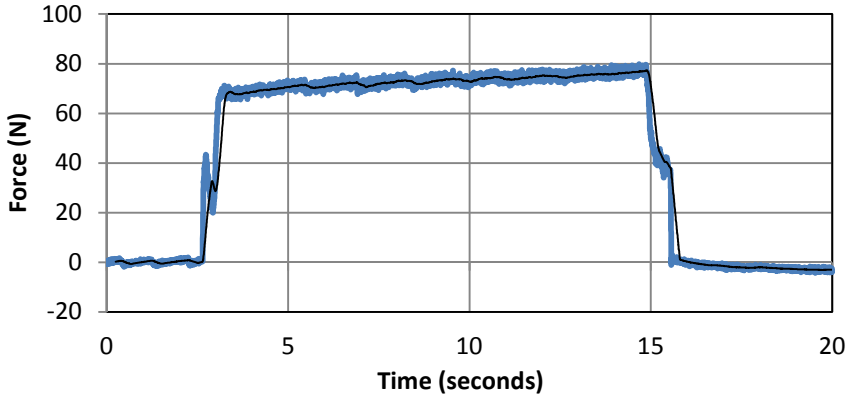

Figure E.8 - Grade 4 y-axis cutting force profile at 0.25 mm DOC and 150 m/min

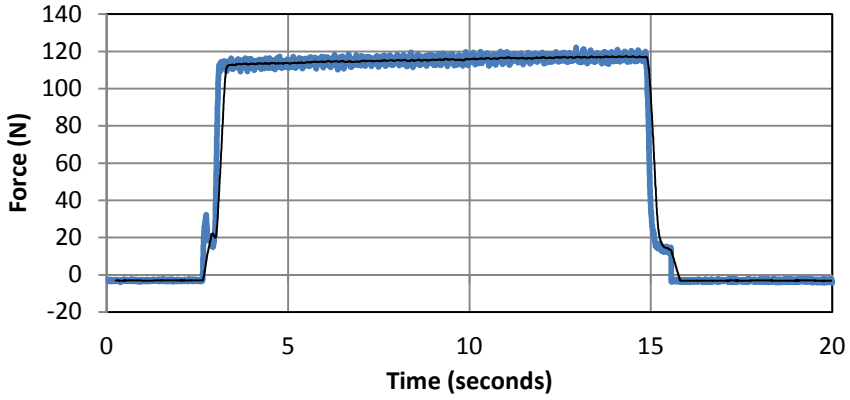

Figure E.9 - Grade 4 z-axis cutting force profile at 0.25 mm DOC and 150 m/min

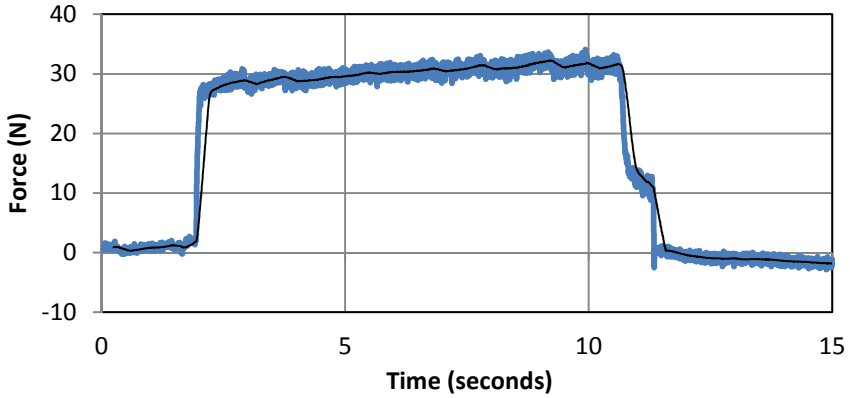

Figure E.10 - Grade 4 x-axis cutting force profile at 0.25 mm DOC and 200 m/min

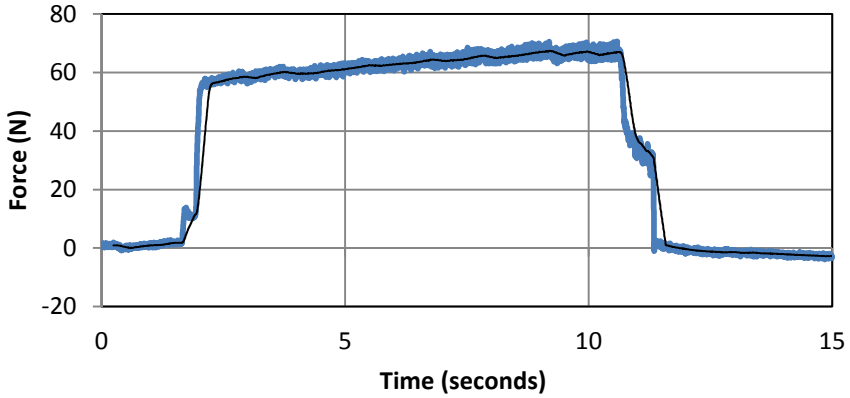

Figure E.11 - Grade 4 y-axis cutting force profile at 0.25 mm DOC and 200 m/min

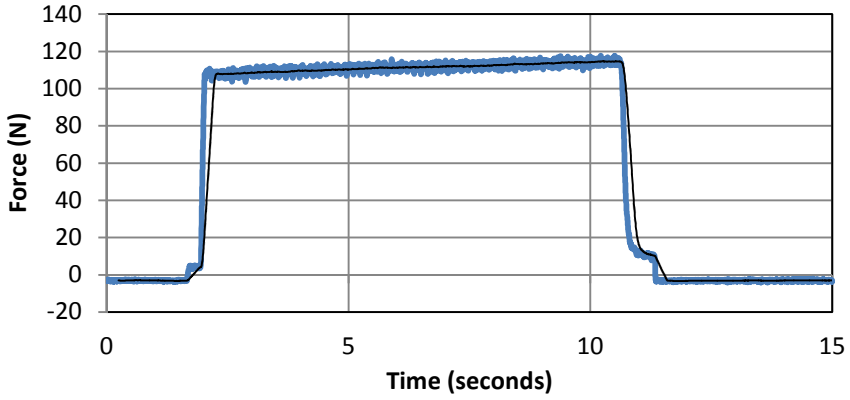

Figure E.12 - Grade 4 z-axis cutting force profile at 0.25 mm DOC and 200 m/min

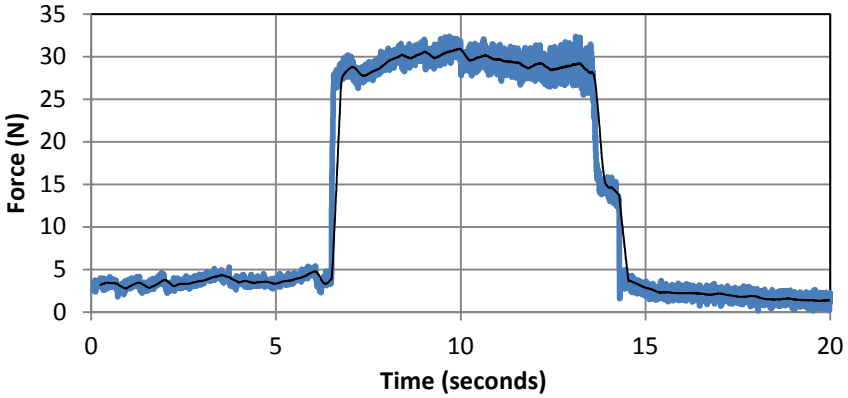

Figure E.13 - Grade 4 x-axis cutting force profile at 0.25 mm DOC and 250 m/min

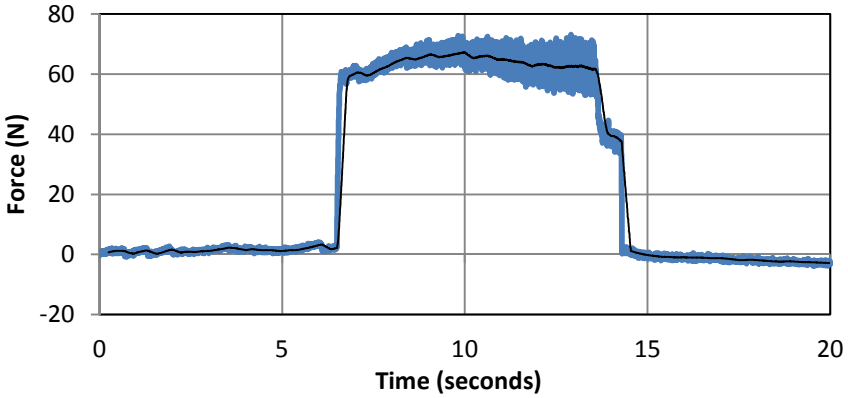

Figure E.14 - Grade 4 y-axis cutting force profile at 0.25 mm DOC and 250 m/min

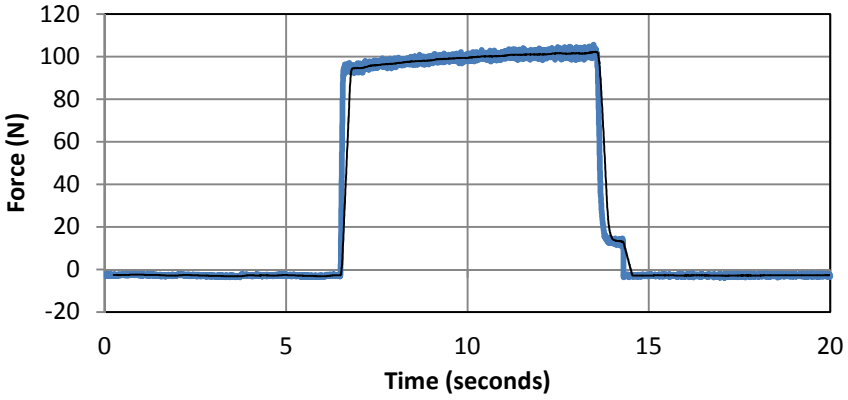

Figure E.15 - Grade 4 z-axis cutting force profile at 0.25 mm DOC and 250 m/min

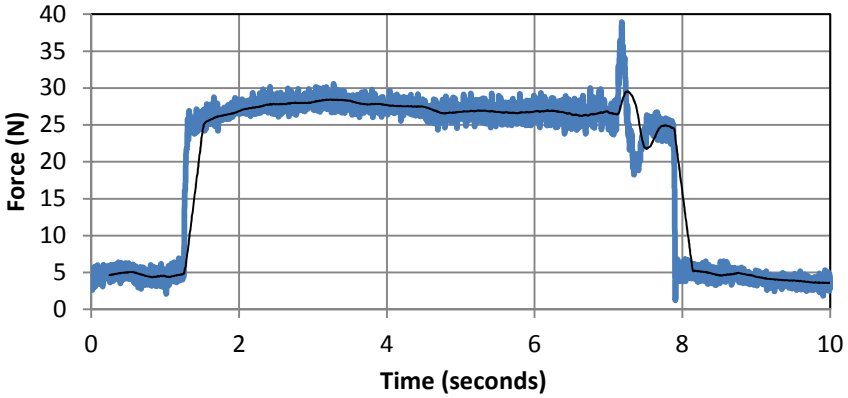

Figure E.16 - Grade 4 x-axis cutting force profile at 0.25 mm DOC and 300 m/min

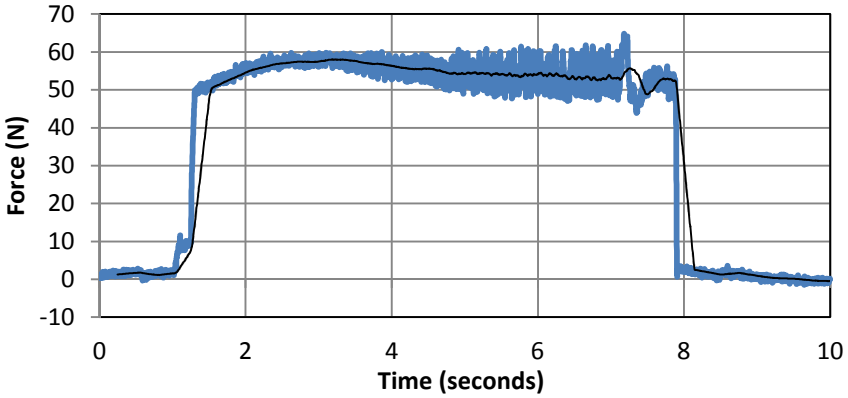

Figure E.17 - Grade 4 y-axis cutting force profile at 0.25 mm DOC and 300 m/min

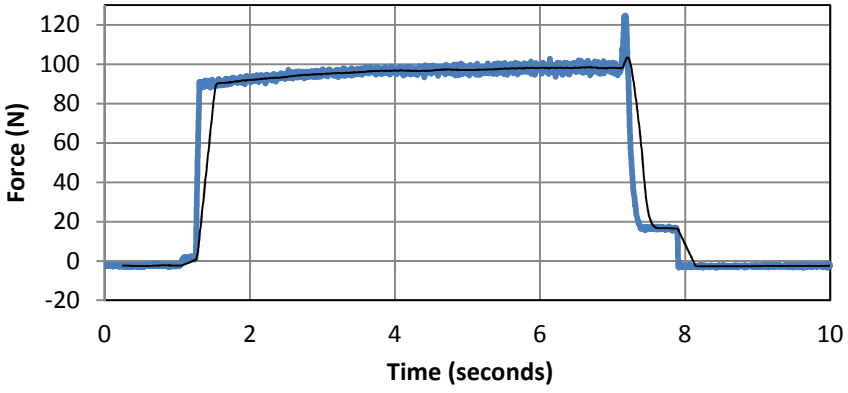

Figure E.18 - Grade 4 z-axis cutting force profile at 0.25 mm DOC and 300 m/min

E.2 Cutting force profiles for Grade 4 at 1.00 mm DOC

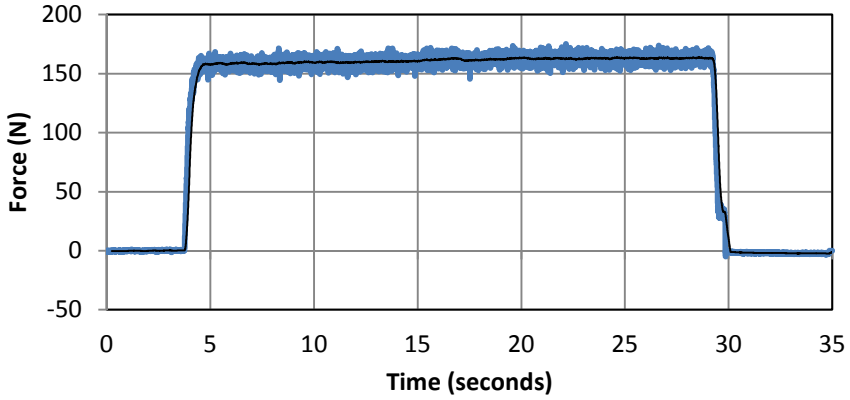

Figure E.19 - Grade 4 x-axis cutting force profile at 1.00 mm DOC and 70 m/min

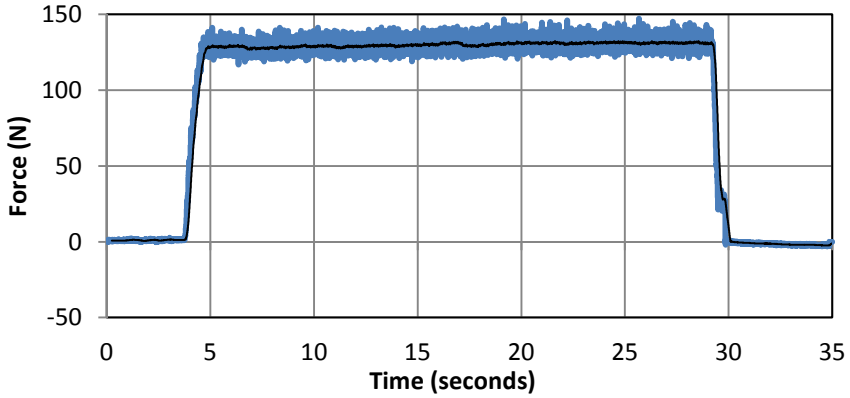

Figure E.20 - Grade 4 y-axis cutting force profile at 1.00 mm DOC and 70 m/min

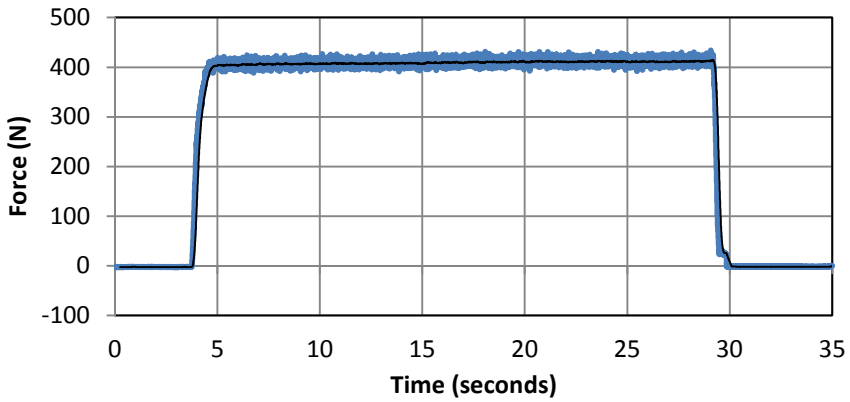

Figure E.21 - Grade 4 z-axis cutting force profile at 1.00 mm DOC and 70 m/min

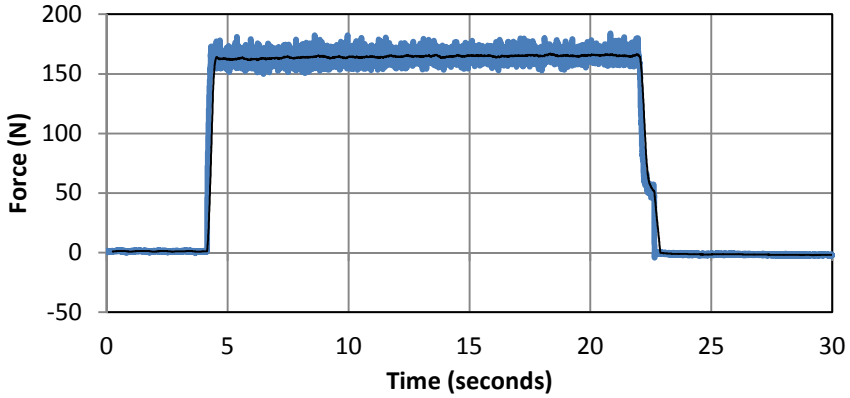

Figure E.22 - Grade 4 x-axis cutting force profile at 1.00 mm DOC and 100 m/min

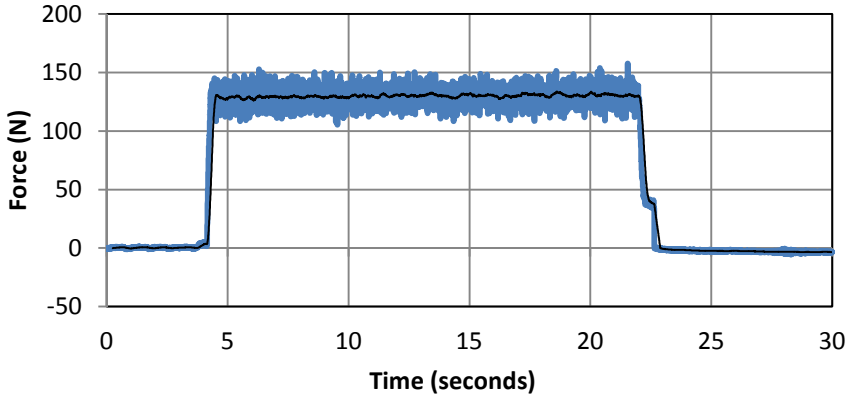

Figure E.23 - Grade 4 y-axis cutting force profile at 1.00 mm DOC and 100 m/min

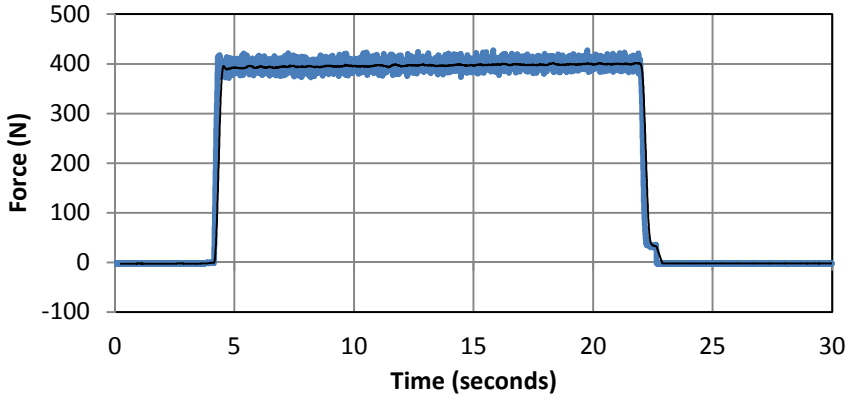

Figure E.24 - Grade 4 z-axis cutting force profile at 1.00 mm DOC and 100 m/min

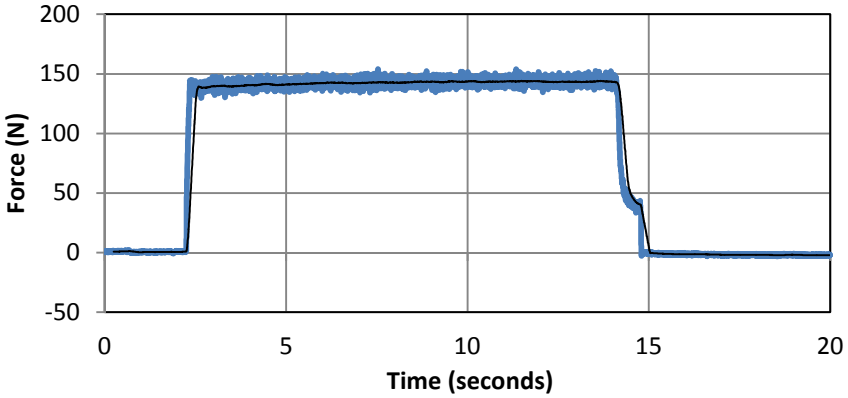

Figure E.25 - Grade 4 x-axis cutting force profile at 1.00 mm DOC and 150 m/min

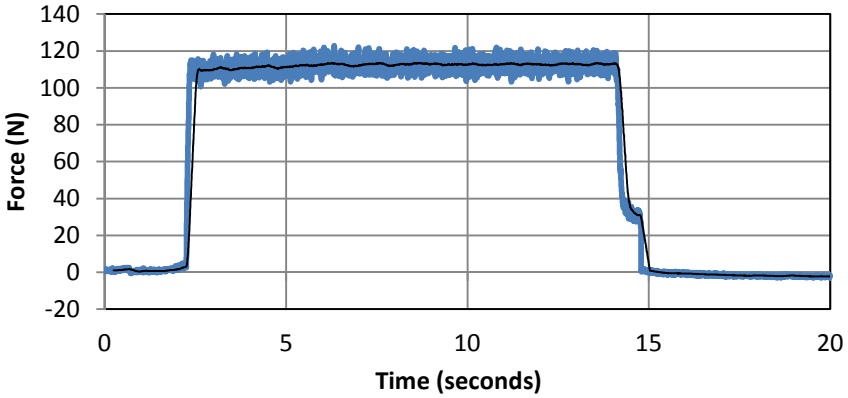

Figure E.26 - Grade 4 y-axis cutting force profile at 1.00 mm DOC and 150 m/min

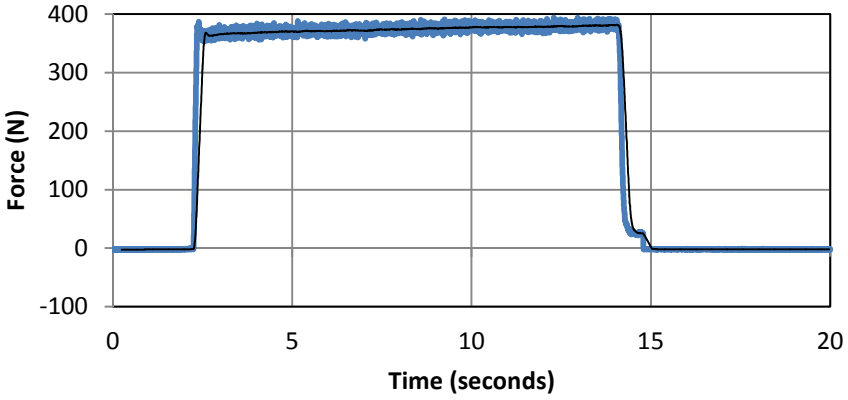

Figure E.27 - Grade 4 z-axis cutting force profile at 1.00 mm DOC and 150 m/min

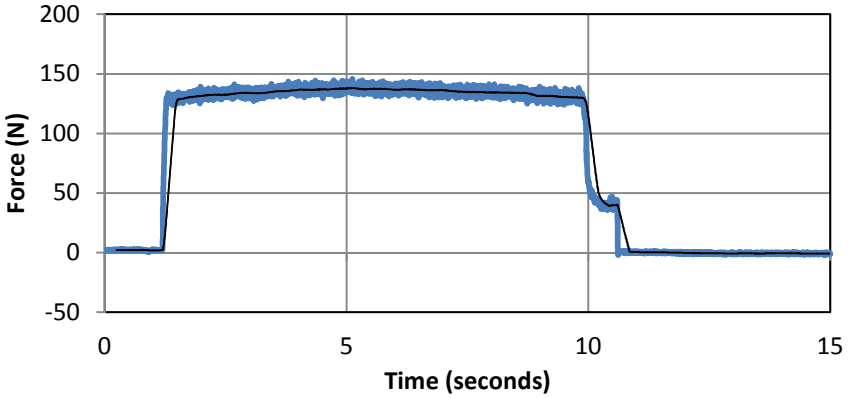

Figure E.28 - Grade 4 x-axis cutting force profile at 1.00 mm DOC and 200 m/min

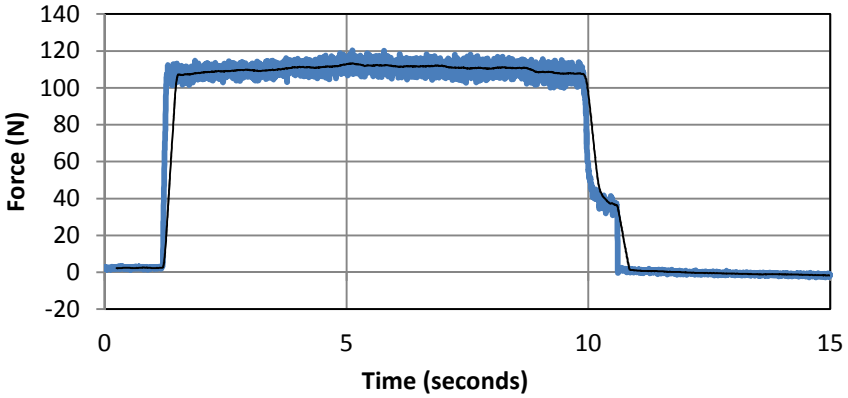

Figure E.29 - Grade 4 y-axis cutting force profile at 1.00 mm DOC and 200 m/min

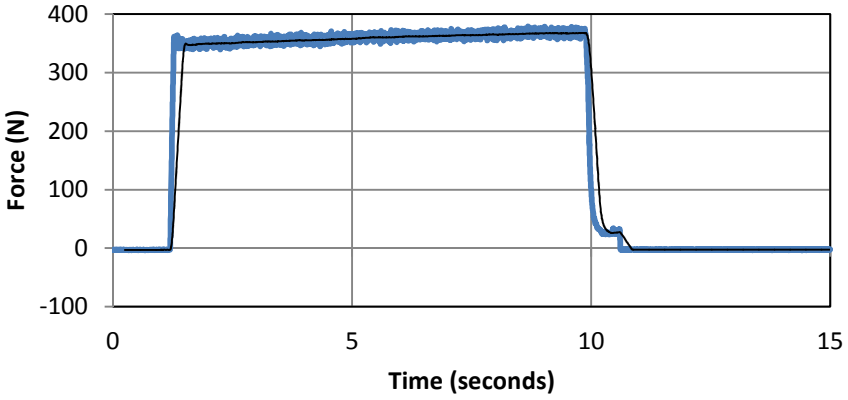

Figure E.30 - Grade 4 z-axis cutting force profile at 1.00 mm DOC and 200 m/min

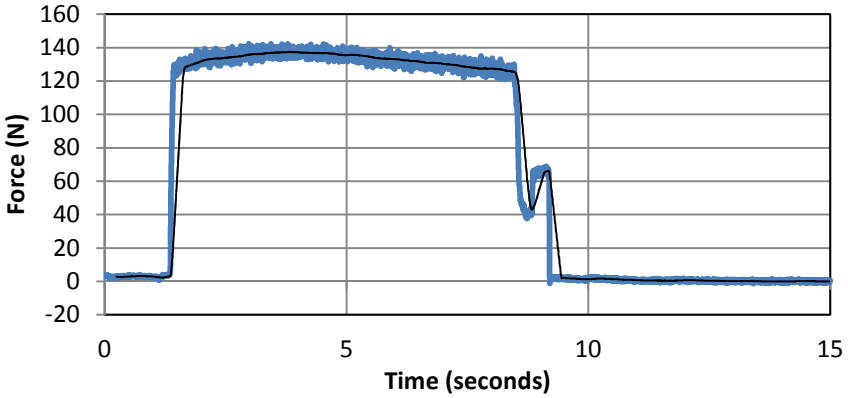

Figure E.31 - Grade 4 x-axis cutting force profile at 1.00 mm DOC and 250 m/min

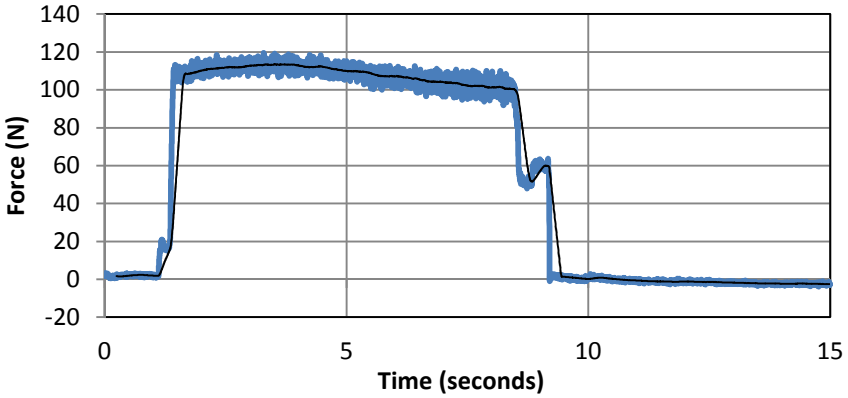

Figure E.32 - Grade 4 y-axis cutting force profile at 1.00 mm DOC and 250 m/min

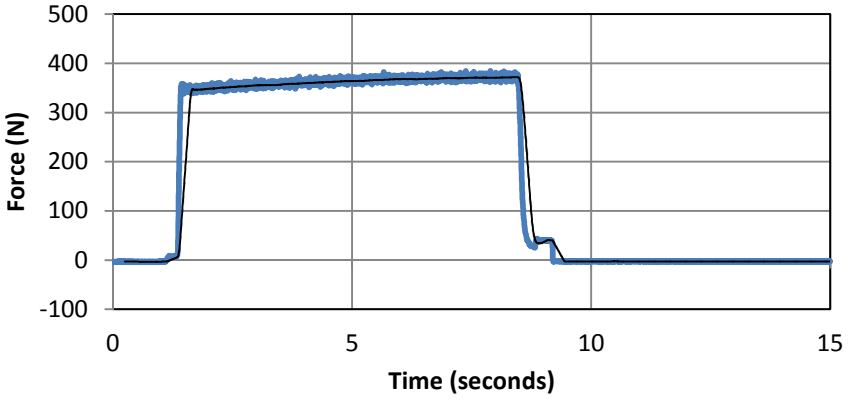

Figure E.33 - Grade 4 z-axis cutting force profile at 1.00 mm DOC and 250 m/min

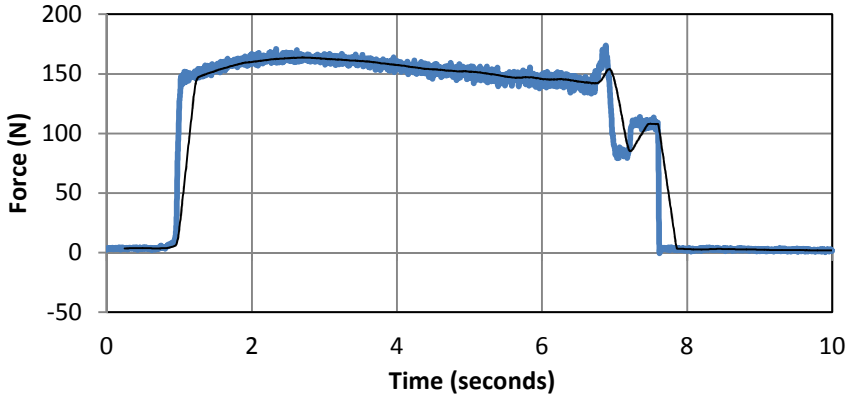

Figure E.34 - Grade 4 x-axis cutting force profile at 1.00 mm DOC and 300 m/min

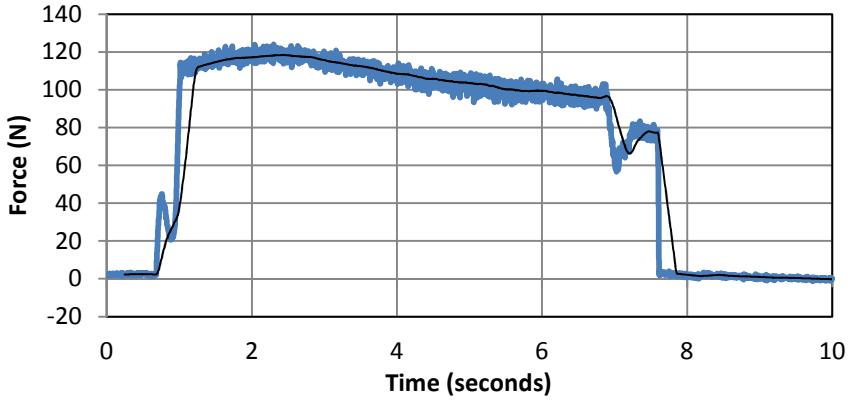

Figure E.35 - Grade 4 y-axis cutting force profile at 1.00 mm DOC and 300 m/min

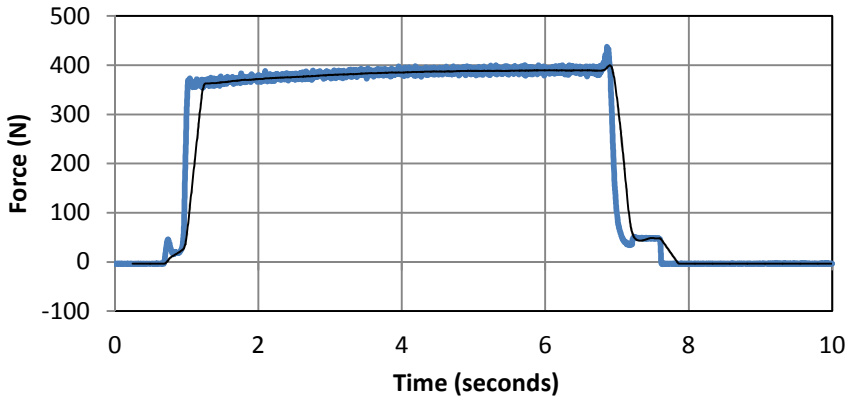

Figure E.36 - Grade 4 z-axis cutting force profile at 1.00 mm DOC and 300 m/min

E.3 Cutting force profiles for Grade 5 at 0.25 mm DOC

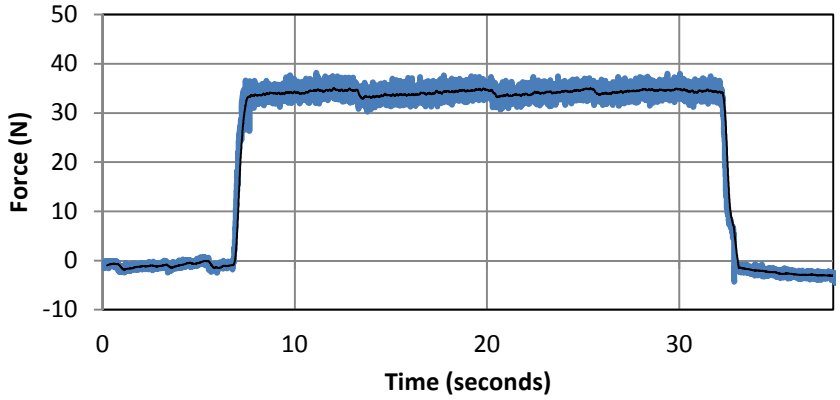

Figure E.37 - Grade 5 x-axis cutting force profile at 0.25 mm DOC and 70 m/min

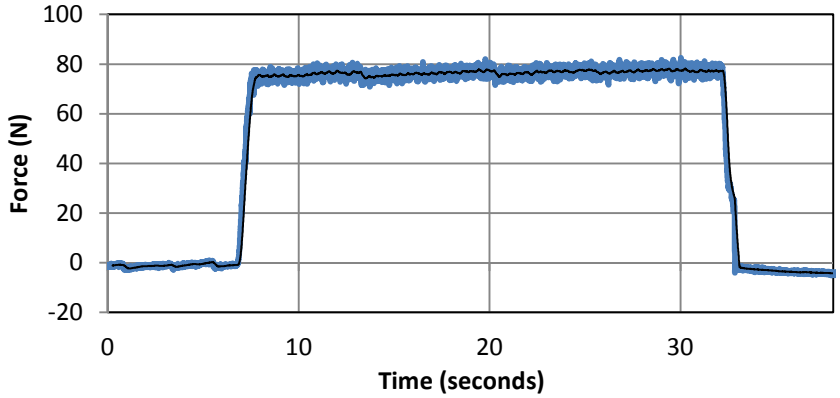

Figure E.38 - Grade 5 y-axis cutting force profile at 0.25 mm DOC and 70 m/min

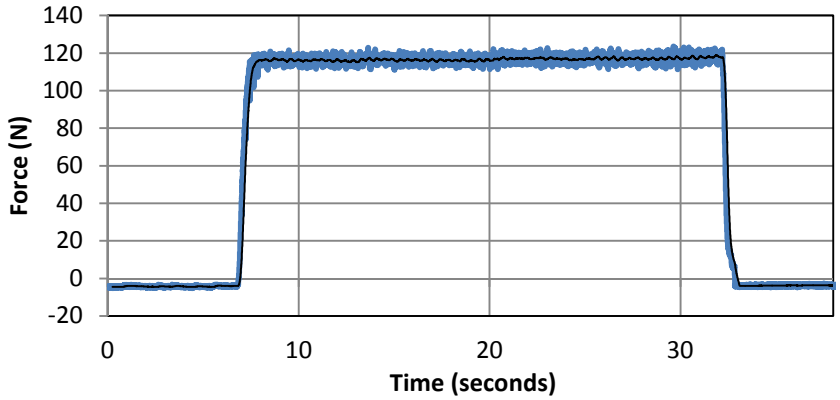

Figure E.39 - Grade 5 z-axis cutting force profile at 0.25 mm DOC and 70 m/min

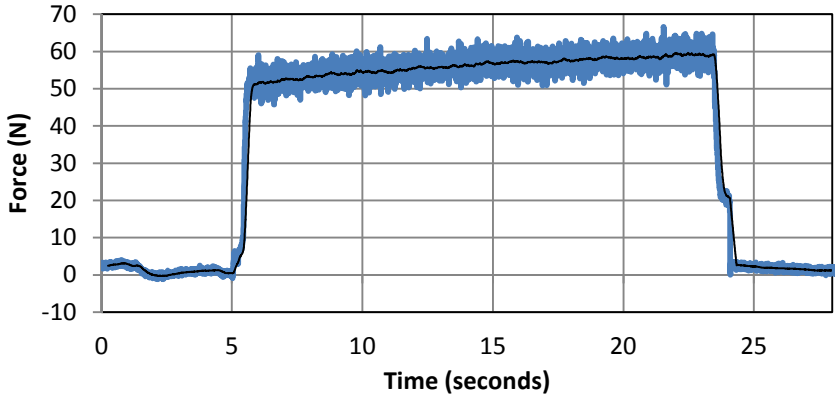

Figure E.40 - Grade 5 x-axis cutting force profile at 0.25 mm DOC and 100 m/min

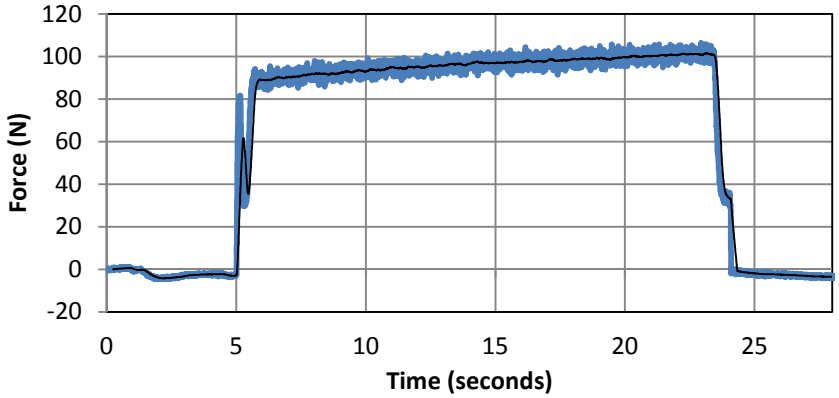

Figure E.41 - Grade 5 y-axis cutting force profile at 0.25 mm DOC and 100 m/min

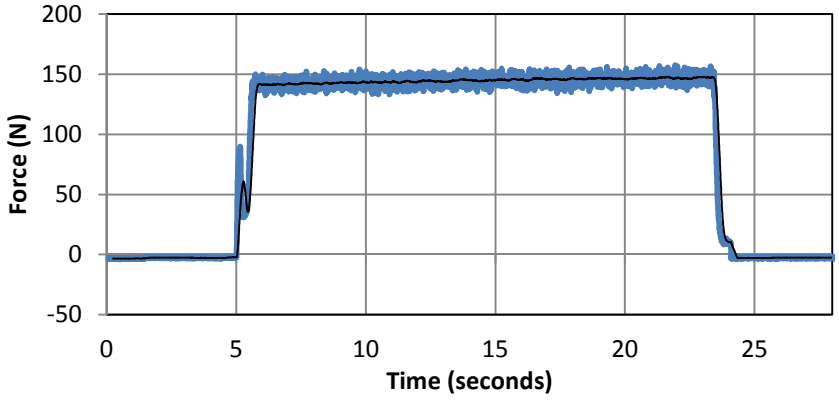

Figure E.42 - Grade 5 z-axis cutting force profile at 0.25 mm DOC and 100 m/min

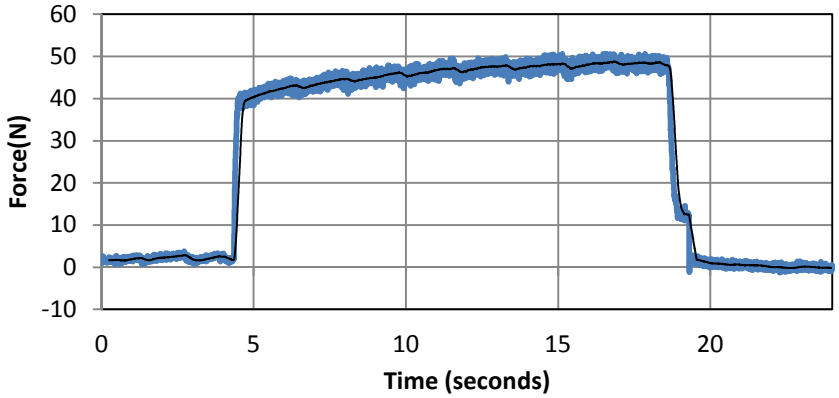

Figure E.43 - Grade 5 x-axis cutting force profile at 0.25 mm DOC and 125 m/min

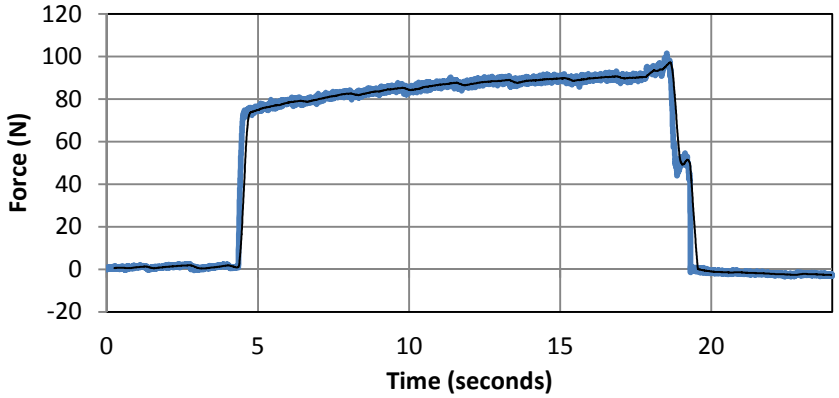

Figure E.44 - Grade 5 y-axis cutting force profile at 0.25 mm DOC and 125 m/min

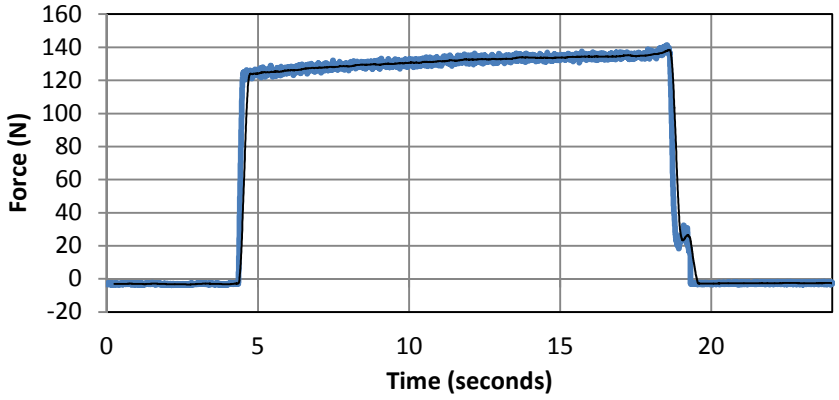

Figure E.45 - Grade 5 z-axis cutting force profile at 0.25 mm DOC and 125 m/min

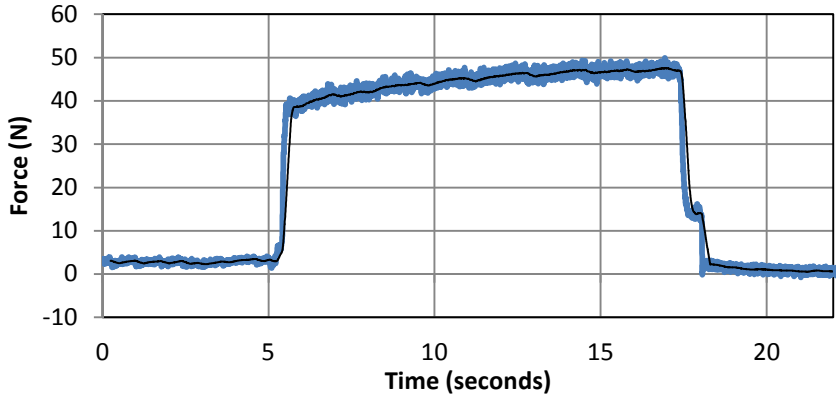

Figure E.46 - Grade 5 x-axis cutting force profile at 0.25 mm DOC and 150 m/min

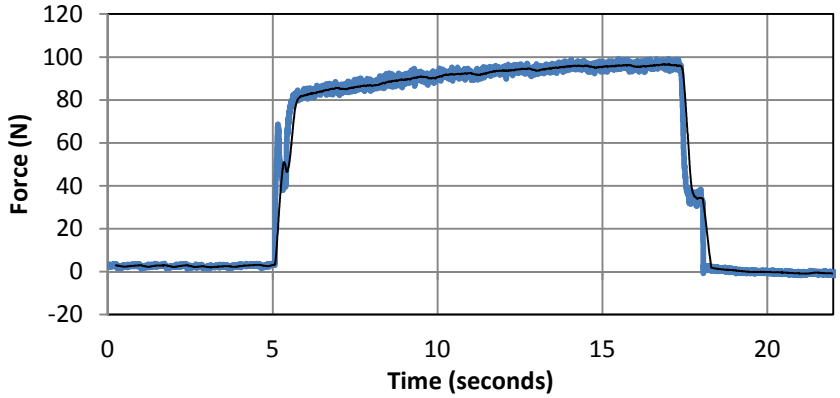

Figure E.47 - Grade 5 y-axis cutting force profile at 0.25 mm DOC and 150 m/min

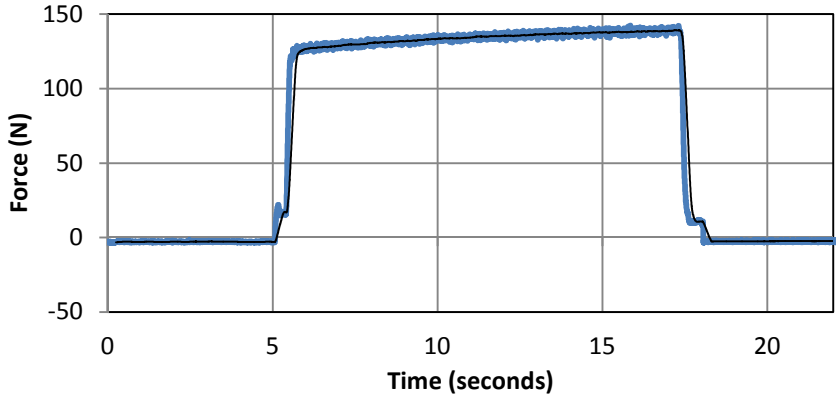

Figure E.48 - Grade 5 z-axis cutting force profile at 0.25 mm DOC and 150 m/min

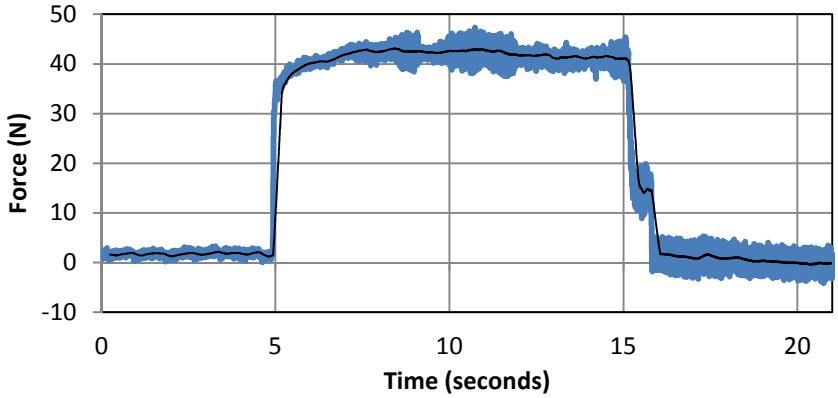

Figure E.49 - Grade 5 x-axis cutting force profile at 0.25 mm DOC and 175 m/min

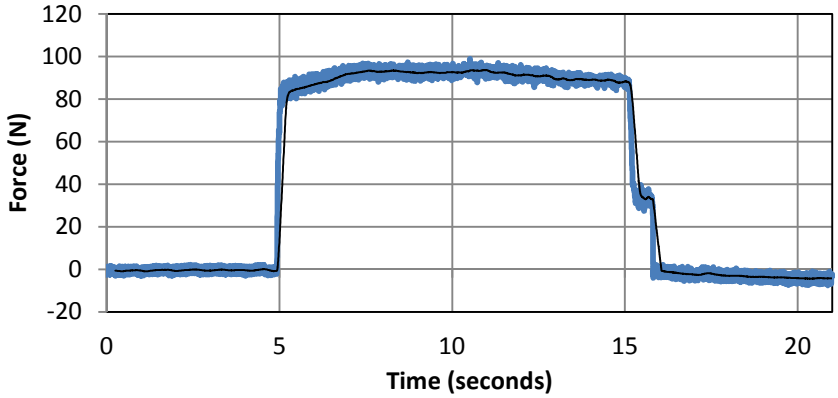

Figure E.50 - Grade 5 y-axis cutting force profile at 0.25 mm DOC and 175 m/min

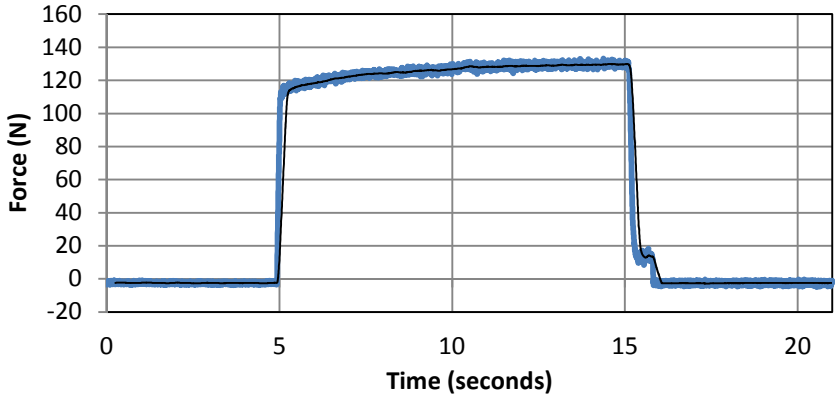

Figure E.51 - Grade 5 z-axis cutting force profile at 0.25 mm DOC and 175 m/min

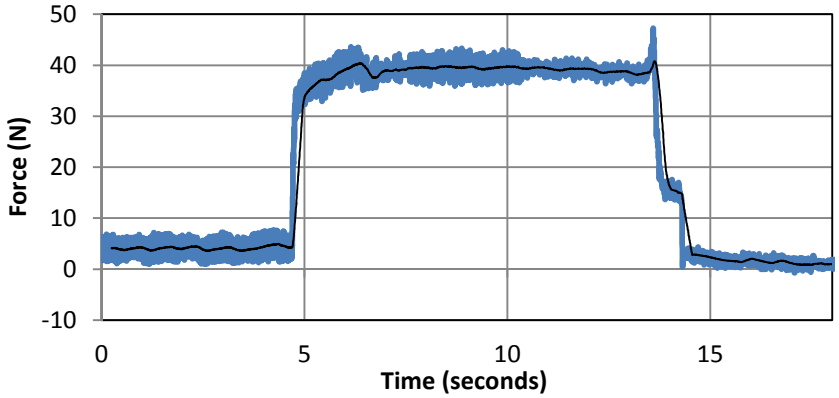

Figure E.52 - Grade 5 x-axis cutting force profile at 0.25 mm DOC and 200 m/min

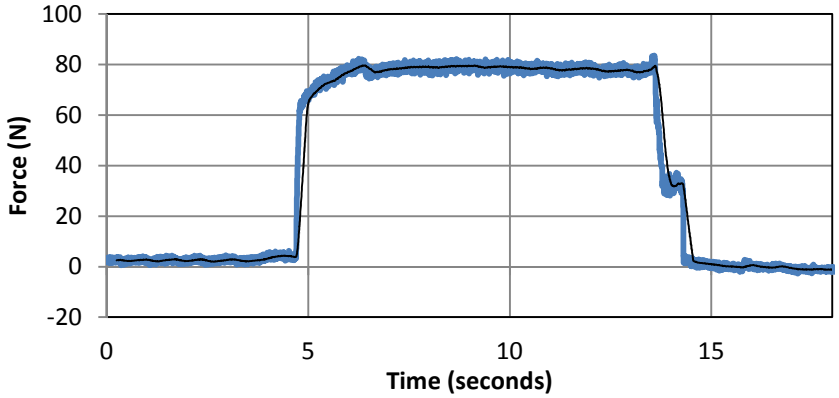

Figure E.53 - Grade 5 y-axis cutting force profile at 0.25 mm DOC and 200 m/min

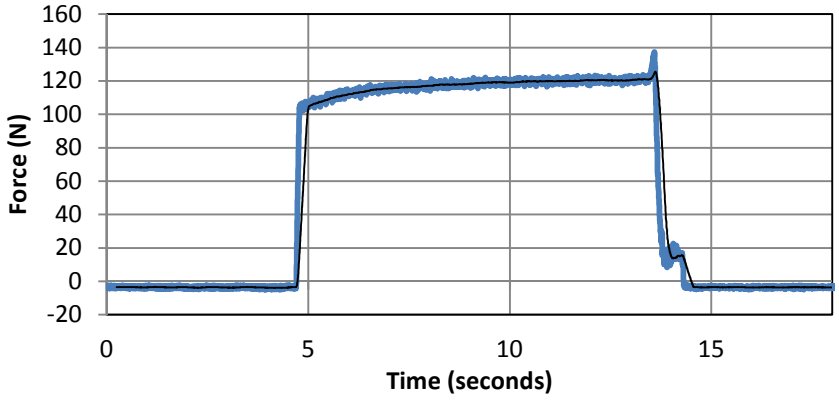

Figure E.54 - Grade 5 z-axis cutting force profile at 0.25 mm DOC and 200 m/min

E.4 Cutting force profiles for Grade 5 at 1.00 mm DOC

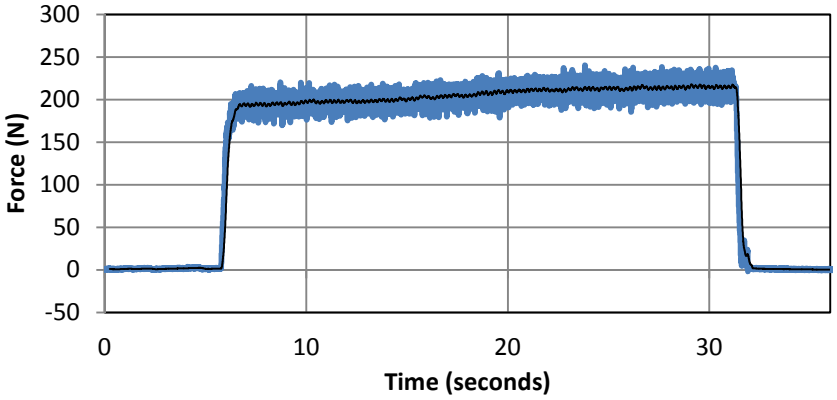

Figure E.55 - Grade 5 x-axis cutting force profile at 1.00 mm DOC and 70 m/min

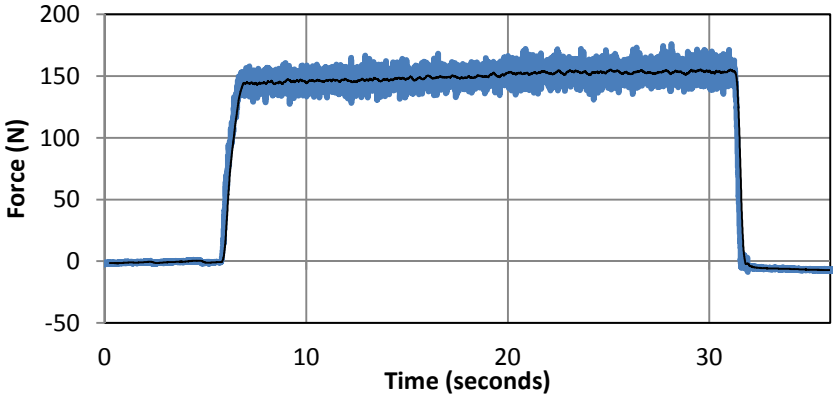

Figure E.56 - Grade 5 y-axis cutting force profile at 1.00 mm DOC and 70 m/min

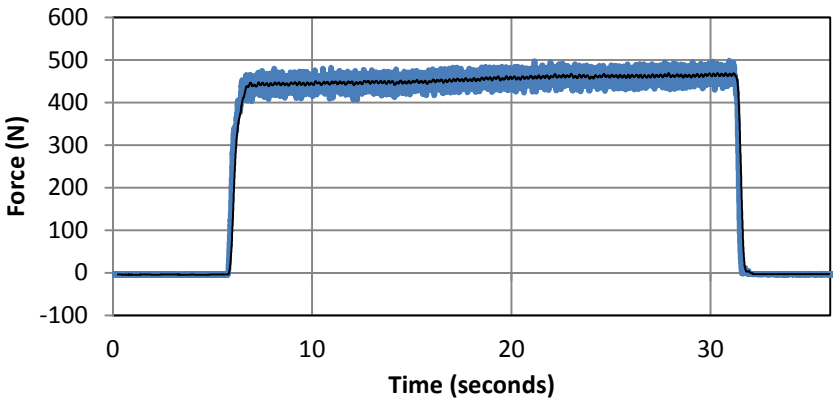

Figure E.57 - Grade 5 z-axis cutting force profile at 1.00 mm DOC and 70 m/min

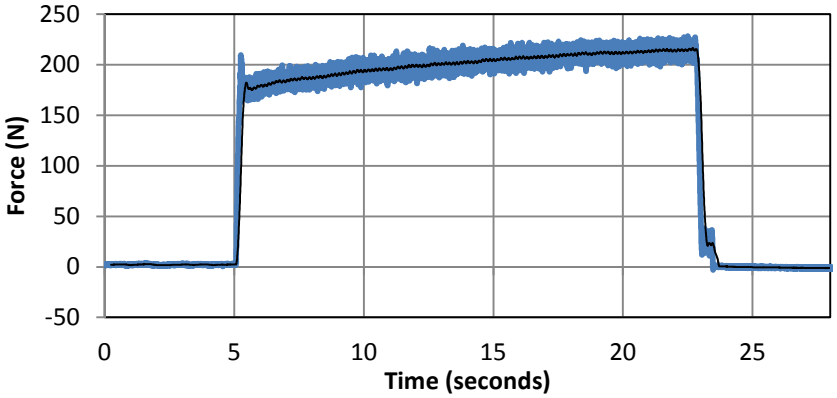

Figure E.58 - Grade 5 x-axis cutting force profile at 1.00 mm DOC and 100 m/min

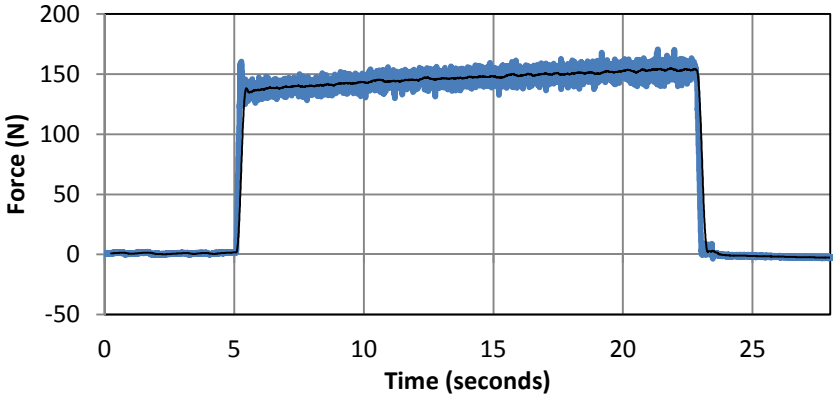

Figure E.59 - Grade 5 y-axis cutting force profile at 1.00 mm DOC and 100 m/min

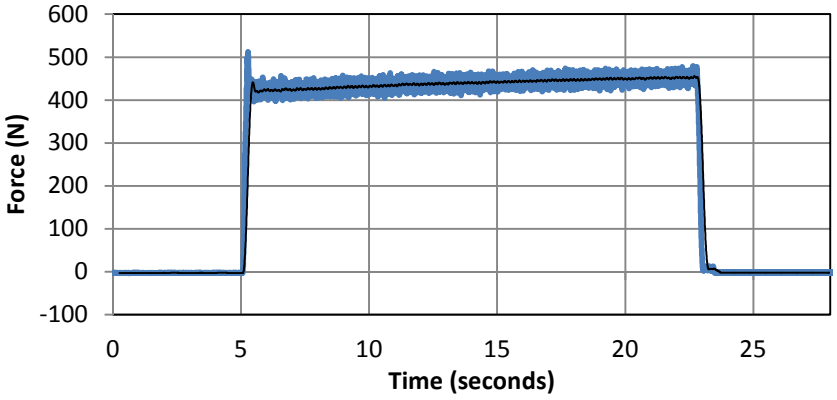

Figure E.60 - Grade 5 z-axis cutting force profile at 1.00 mm DOC and 100 m/min

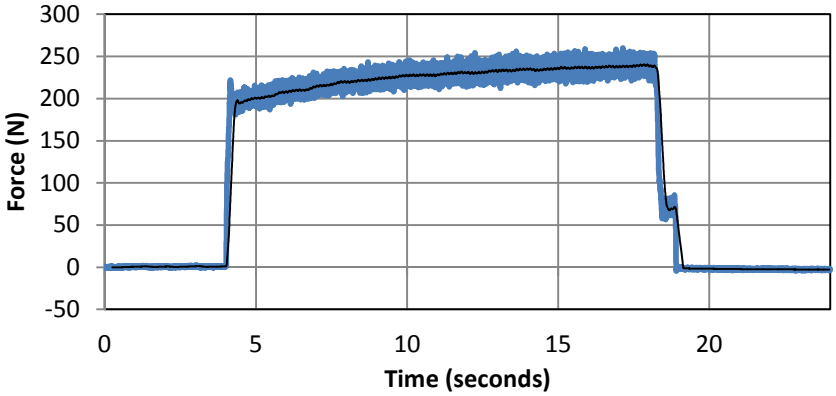

Figure E.61 - Grade 5 x-axis cutting force profile at 1.00 mm DOC and 125 m/min

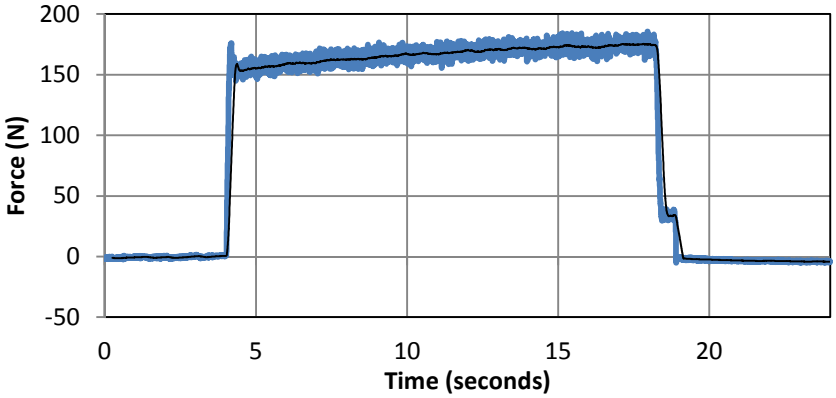

Figure E.62 - Grade 5 y-axis cutting force profile at 1.00 mm DOC and 125 m/min

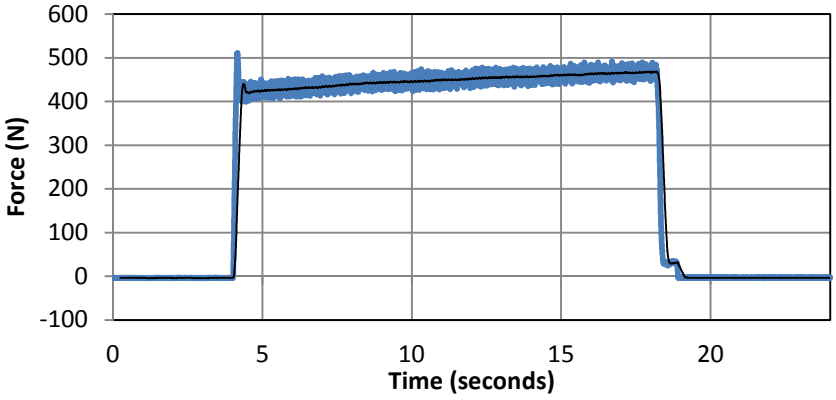

Figure E.63 - Grade 5 z-axis cutting force profile at 1.00 mm DOC and 125 m/min

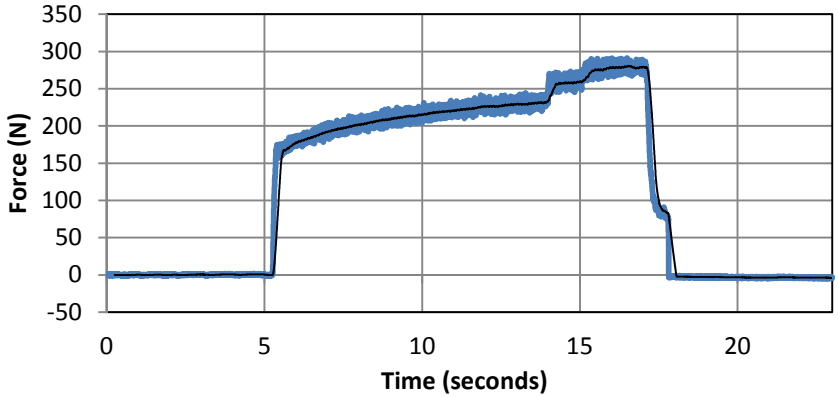

Figure E.64 - Grade 5 x-axis cutting force profile at 1.00 mm DOC and 150 m/min

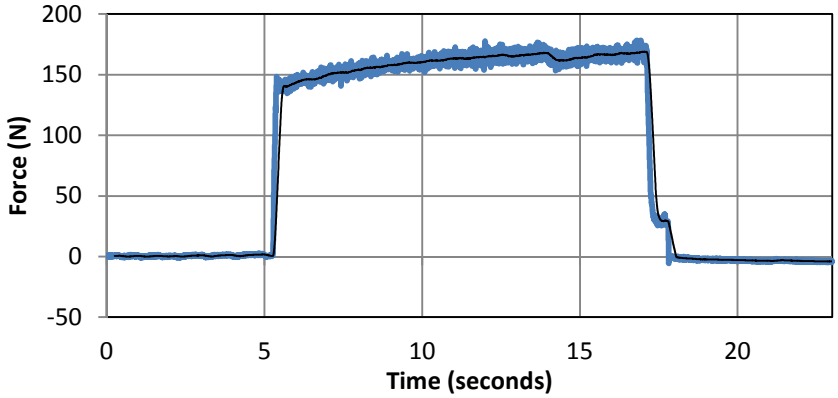

Figure E.65 - Grade 5 y-axis cutting force profile at 1.00 mm DOC and 150 m/min

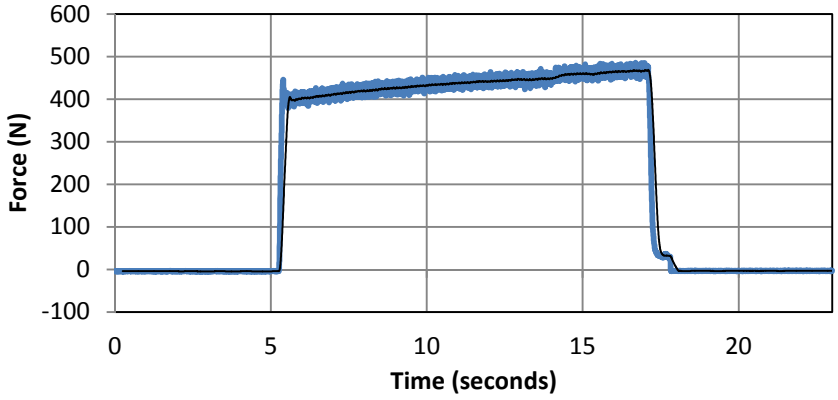

Figure E.66 - Grade 5 z-axis cutting force profile at 1.00 mm DOC and 150 m/min

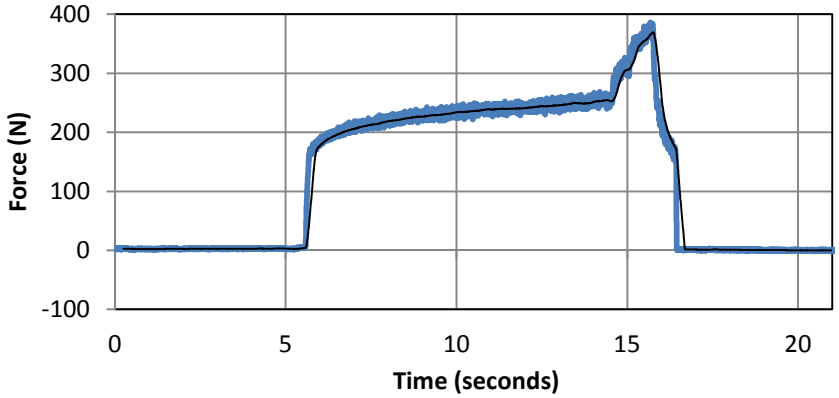

Figure E.67 - Grade 5 x-axis cutting force profile at 1.00 mm DOC and 175 m/min

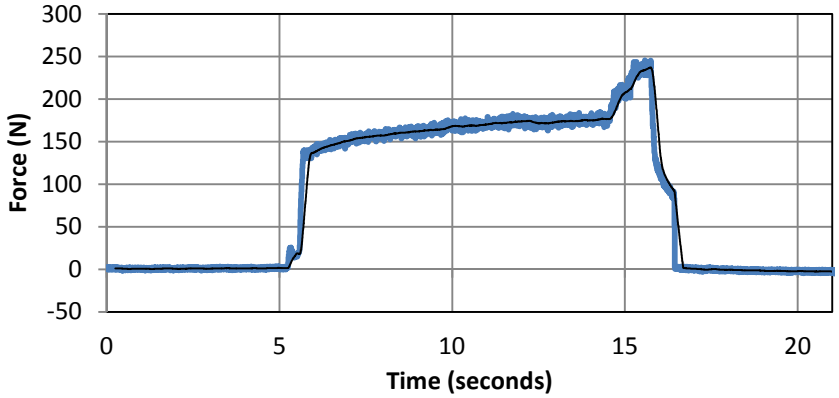

Figure E.68 - Grade 5 y-axis cutting force profile at 1.00 mm DOC and 175 m/min

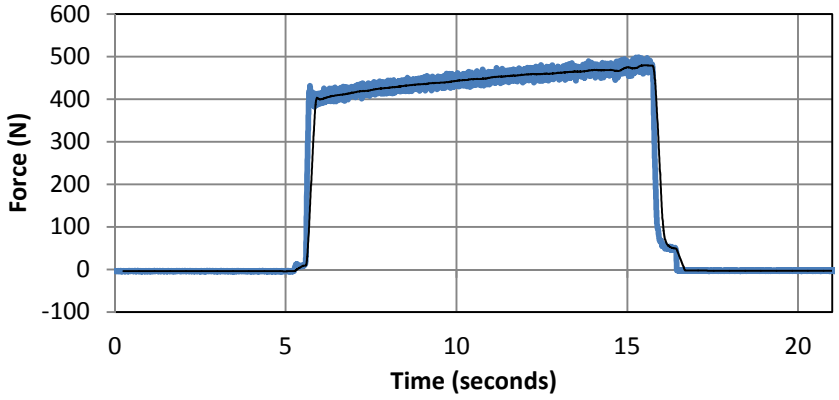

Figure E.69 - Grade 5 z-axis cutting force profile at 1.00 mm DOC and 175 m/min

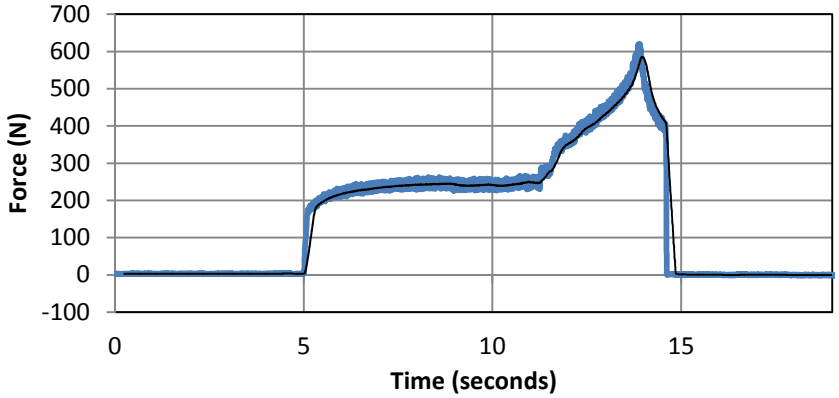

Figure E.70 - Grade 5 x-axis cutting force profile at 1.00 mm DOC and 200 m/min

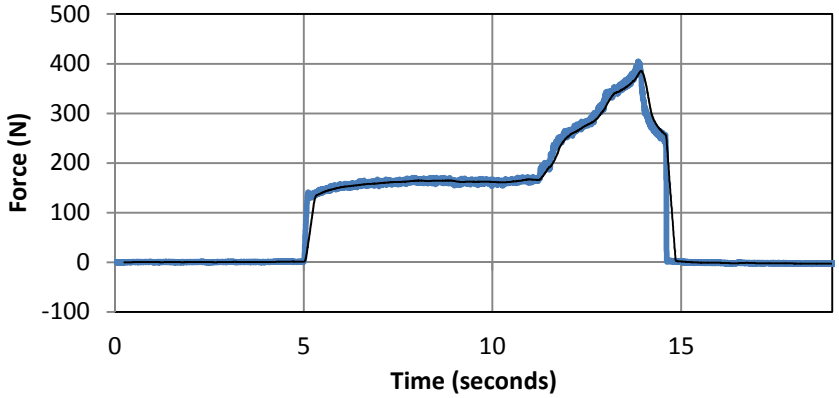

Figure E.71 - Grade 5 y-axis cutting force profile at 1.00 mm DOC and 200 m/min

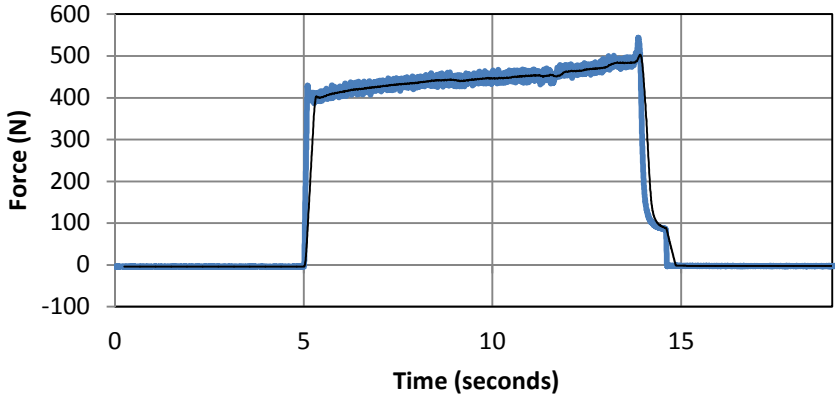

Figure E.72 - Grade 5 z-axis cutting force profile at 1.00 mm DOC and 200 m/min

E.5 Extracted Grade 4 and 5 cutting forces

Table E.1 - Grade 4 cutting forces

0.25 mm depth of cut					1.00 mm depth of cut				
Force direction		x (N)	y (N)	z (N)	Force direction		x (N)	y (N)	z (N)
Cutting speed (m/min)	70	36.49	77.14	117.43	Cutting speed (m/min)	70	156.42	125.45	398.25
	100	32.35	79.19	114.23		100	169.31	128.57	405.85
	150	31.79	72.61	115.29		150	146.80	120.44	380.84
	200	30.41	63.89	109.04		200	139.98	111.26	369.60
	250	29.35	63.66	99.82		250	133.25	107.07	364.21
	300	26.41	59.07	97.38		300	149.69	108.28	378.26

Table E.2 - Grade 5 cutting forces

0.25 mm depth of cut					1.00 mm depth of cut				
Force direction		x (N)	y (N)	z (N)	Force direction		x (N)	y (N)	z (N)
Cutting speed (m/min)	70	35.39	78.60	119.14	Cutting speed (m/min)	70	204.39	150.65	456.97
	100	58.71	98.79	146.75		100	208.73	151.25	450.86
	125	47.96	88.34	131.33		125	220.39	163.91	446.78
	150	46.82	91.96	133.43		150	227.46	165.11	443.15
	175	43.38	91.39	126.98		175	235.17	166.73	439.16
	200	38.21	81.21	119.06		200	245.69	167.35	437.67

Appendix F: Full Stress Tensor Reports and Extracted Residual Stress Data

Full stress tensor reports are obtained for all samples. The reports contain relevant information concerning the sample properties and setup, the type of x-rays and evaluation methods used, as well as the full stress tensor. The longitudinal residual stresses (σ_{11}), transverse residual stresses (σ_{22}), and shear residual stresses (σ_{12}) are extracted from these stress tensor reports. These stresses are presented in Table F.1 and Table F.2. Of the reports achieved for each data set, the first report represents the sample machined with only a finishing cut. The subsequent samples represent the samples machined at separate cutting speeds.

F.1 Full stress tensor report for Grade 4 at 0.25 mm DOC and finish cut

9/15/2011 11:24:16 AM
Project: Stress_2D
Operator: Bruker Instrument Administrator
Site: NECSA
Measured : 09/14/11 18:29:35

Sample

Material	HKL	Wavelength	2theta	Poisson	Young	s1	1/2s2	Arx
Ti	(2 1 3)	0.154055 (Cu)Ka1	139.32	0.32	112994.00	-2.832E-6	1.168E-5	1.00

Corrections : Absorption , Background (5) , Polarisation , Smooth , K alpha 2 (0.50)

Peak Evaluation Method : Pearson VII

Stresss Model : Biaxial + Shear

Normal : -279.5 ± 12.3 **Shear :** 1.4 ±4.5 (**Phi :** 0 **Psi :** 90)

Pseudo-Hydro : 153.4 ± 13.3

Stress Tensor :			
-145.9 ± 12.3	-9.4 ± 12.9	1.4 ± 4.5
-9.4 ± 12.9	-279.5 ± 12.3	27.3 ± 4.5
1.4 ± 4.5	27.3 ± 4.5	0.0 ± 0.0

F.2 Full stress tensor report for Grade 4 at 0.25 mm DOC and 70 m/min

9/15/2011 10:55:27 AM
Project: Stress_2D
Operator: Bruker Instrument Administrator
Site: NECSA
Measured : 09/13/11 11:51:32

Sample

Material	HKL	Wavelength	2theta	Poisson	Young	s1	1/2s2	Arx
Ti	(2 1 3)	0.154055 (Cu)Ka1	139.32	0.32	112994.00	-2.832E-6	1.168E-5	1.00

Corrections : Absorption , Background (5) , Polarisation , Smooth , K alpha 2 (0.50)

Peak Evaluation Method : Pearson VII

Stresss Model : Biaxial + Shear

Normal : -60.4 ± 12.9 **Shear :** -3.3 ± 4.8 (**Phi :** 0 **Psi :** 90)

Pseudo-Hydro : 194.9 ± 13.9

Stress Tensor :

-174.8 ± 12.9	-86.9 ± 13.6	-3.3 ± 4.8
-86.9 ± 13.6	-60.4 ± 12.9	-16.3 ± 4.8
-3.3 ± 4.8	-16.3 ± 4.8	0.0 ± 0.0

F.3 Full stress tensor report for Grade 4 at 0.25 mm DOC and 100 m/min

9/15/2011 10:58:58 AM
Project: Stress_2D
Operator: Bruker Instrument Administrator
Site: NECSA
Measured : 09/13/11 14:23:57

Sample

Material	HKL	Wavelength	2theta	Poisson	Young	s1	1/2s2	Arx
Ti	(2 1 3)	0.154055 (Cu)Ka1	139.32	0.32	112994.00	-2.832E-6	1.168E-5	1.00

Corrections : Absorption , Background (5) , Polarisation , Smooth , K alpha 2 (0.50)

Peak Evaluation Method : Gravity (30)

Stresss Model : Biaxial + Shear

Normal : 35.8 ± 19.6 **Shear :** 1.3 ± 7.2 (**Phi :** 0 **Psi :** 90)

Pseudo-Hydro : 231.6 ± 21.2

Stress Tensor :

-24.8 ± 19.7	-97.4 ± 20.7	1.3 ± 7.2
-97.4 ± 20.7	35.8 ± 19.6	-29.0 ± 7.3
1.3 ± 7.2	-29.0 ± 7.3	0.0 ± 0.0

F.4 Full stress tensor report for Grade 4 at 0.25 mm DOC and 150 m/min

9/15/2011 11:02:32 AM
Project: Stress_2D
Operator: Bruker Instrument Administrator
Site: NECSA
Measured : 09/13/11 16:43:28

Sample

Material	HKL	Wavelength	2theta	Poisson	Young	s1	1/2s2	Arx
Ti	(2 1 3)	0.154055 (Cu)Ka1	139.32	0.32	112994.00	-2.832E-6	1.168E-5	1.00

Corrections : Absorption , Background (5) , Polarisation , Smooth , K alpha 2 (0.50)

Peak Evaluation Method : Pearson VII

Stresss Model : Biaxial + Shear

Normal : 117.8 ± 18.1 **Shear :** -0.4 ±6.7 (**Phi :** 0 **Psi :** 90)

Pseudo-Hydro : 137.9 ± 19.5

Stress Tensor :

50.3 ± 18.2	-31.4 ± 19.0	-0.4 ± 6.7
-31.4 ± 19.0	117.8 ± 18.1	-35.8 ± 6.7
-0.4 ± 6.7	-35.8 ± 6.7	0.0 ± 0.0

F.5 Full stress tensor report for Grade 4 at 0.25 mm DOC and 200 m/min

9/15/2011 11:05:58 AM
Project: Stress_2D
Operator: Bruker Instrument Administrator
Site: NECSA
Measured : 09/14/11 08:04:28

Sample

Material	HKL	Wavelength	2theta	Poisson	Young	s1	1/2s2	Arx
Ti	(2 1 3)	0.154055 (Cu)Ka1	139.32	0.32	112994.00	-2.832E-6	1.168E-5	1.00

Corrections : Absorption , Background (5) , Polarisation , Smooth , K alpha 2 (0.50)

Peak Evaluation Method : Pearson VII

Stresss Model : Biaxial + Shear

Normal : -4.2 ± 18.1 **Shear :** 5.0 ±6.7 (**Phi :** 0 **Psi :** 90)

Pseudo-Hydro : 108.1 ± 19.5

Stress Tensor :

-82.7 ± 18.1	-73.9 ± 19.0	5.0 ± 6.7
-73.9 ± 19.0	-4.2 ± 18.1	-18.8 ± 6.7
5.0 ± 6.7	-18.8 ± 6.7	0.0 ± 0.0

F.6 Full stress tensor report for Grade 4 at 0.25 mm DOC and 250 m/min

9/15/2011 11:17:21 AM
Project: Stress_2D
Operator: Bruker Instrument Administrator
Site: NECSA
Measured : 09/14/11 10:32:57

Sample

Material	HKL	Wavelength	2theta	Poisson	Young	s1	1/2s2	Arx
Ti	(2 1 3)	0.154055 (Cu)Ka1	139.32	0.32	112994.00	-2.832E-6	1.168E-5	1.00

Corrections : Absorption , Background (5) , Polarisation , Smooth , K alpha 2 (0.50)

Peak Evaluation Method : Pearson VII

Stresss Model : Biaxial + Shear

Normal : 70.5 ± 18.5 **Shear :** 11.8 ±6.8 (**Phi :** 0 **Psi :** 90)

Pseudo-Hydro : 160.0 ± 20.1

Stress Tensor :

135.3 ± 18.6	-34.1 ± 19.5	11.8 ± 6.8
-34.1 ± 19.5	70.5 ± 18.5	-41.9 ± 6.8
11.8 ± 6.8	-41.9 ± 6.8	0.0 ± 0.0

F.7 Full stress tensor report for Grade 4 at 0.25 mm DOC and 300 m/min

9/15/2011 11:21:07 AM
Project: Stress_2D
Operator: Bruker Instrument Administrator
Site: NECSA
Measured : 09/14/11 13:03:03

Sample

Material	HKL	Wavelength	2theta	Poisson	Young	s1	1/2s2	Arx
Ti	(2 1 3)	0.154055 (Cu)Ka1	139.32	0.32	112994.00	-2.832E-6	1.168E-5	1.00

Corrections : Absorption , Background (5) , Polarisation , Smooth , K alpha 2 (0.50)

Peak Evaluation Method : Pearson VII

Stresss Model : Biaxial + Shear

Normal : 46.6 ± 17.9 **Shear :** 5.1 ±6.6 (**Phi :** 0 **Psi :** 90)

Pseudo-Hydro : 180.6 ± 19.3

Stress Tensor :

42.6 ± 18.0	-41.5 ± 18.8	5.1 ± 6.6
-41.5 ± 18.8	46.6 ± 17.9	-35.9 ± 6.6
5.1 ± 6.6	-35.9 ± 6.6	0.0 ± 0.0

F.8 Full stress tensor report for Grade 4 at 1.00 mm DOC and finish cut

9/15/2011 10:49:43 AM
Project: Stress_2D
Operator: Bruker Instrument Administrator
Site: NECSA
Measured : 09/13/11 09:29:11

Sample

Material	HKL	Wavelength	2theta	Poisson	Young	s1	1/2s2	Arx
Ti	(2 1 3)	0.154055 (Cu_)Ka1	139.32	0.32	112994.00	-2.832E-6	1.168E-5	1.00

Corrections : Absorption , Background (5) , Polarisation , Smooth , K alpha 2 (0.50)

Peak Evaluation Method : Pearson VII

Stresss Model : Biaxial + Shear

Normal : -254.9 ± 10.3 **Shear :** 4.1 ± 3.8 (**Phi :** 90 **Psi :** 90)

Pseudo-Hydro : 112.3 ± 11.1

Stress Tensor :

-254.9 ± 10.3	25.2 ± 10.8	-3.2 ± 3.8
25.2 ± 10.8	-527.8 ± 10.3	4.1 ± 3.8
-3.2 ± 3.8	4.1 ± 3.8	0.0 ± 0.0

F.9 Full stress tensor report for Grade 4 at 1.00 mm DOC and 70 m/min

9/15/2011 10:17:11 AM
Project: Stress_2D
Operator: Bruker Instrument Administrator
Site: NECSA
Measured : 09/09/11 10:41:46

Sample

Material	HKL	Wavelength	2theta	Poisson	Young	s1	1/2s2	Arx
Ti	(2 1 3)	0.154055 (Cu_)Ka1	139.32	0.32	112994.00	-2.832E-6	1.168E-5	1.00

Corrections : Absorption , Background (5) , Polarisation , Smooth , K alpha 2 (0.50)

Peak Evaluation Method : Pearson VII

Stresss Model : Biaxial + Shear

Normal : 1.8 ± 10.8 **Shear :** -13.1 ± 5.6 (**Phi :** 0 **Psi :** 90)

Pseudo-Hydro : 248.4 ± 12.1

Stress Tensor :

-149.3 ± 10.8	-71.2 ± 14.8	-13.1 ± 5.6
-71.2 ± 14.8	1.8 ± 10.8	-30.4 ± 5.6
-13.1 ± 5.6	-30.4 ± 5.6	0.0 ± 0.0

F.10 Full stress tensor report for Grade 4 at 1.00 mm DOC and 100 m/min

9/15/2011 10:24:54 AM
Project: Stress_2D
Operator: Bruker Instrument Administrator
Site: NECSA
Measured : 09/09/11 13:39:29

Sample

Material	HKL	Wavelength	2theta	Poisson	Young	s1	1/2s2	Arx
Ti	(2 1 3)	0.154055 (Cu_)Ka1	139.32	0.32	112994.00	-2.832E-6	1.168E-5	1.00

Corrections : Absorption , Background (5) , Polarisation , Smooth , K alpha 2 (0.50)

Peak Evaluation Method : Pearson VII

Stresss Model : Biaxial + Shear

Normal : -56.3 ± 10.0 **Shear :** -1.2 ±5.2 (**Phi :** 0 **Psi :** 90)

Pseudo-Hydro : 233.6 ± 13.4

Stress Tensor :

-179.8 ± 14.2	-84.4 ± 11.4	-1.2 ± 5.2
-84.4 ± 11.4	-56.3 ± 10.0	15.0 ± 5.2
-1.2 ± 5.2	15.0 ± 5.2	0.0 ± 0.0

F.11 Full stress tensor report for Grade 4 at 1.00 mm DOC and 150 m/min

9/15/2011 10:32:24 AM
Project: Stress_2D
Operator: Bruker Instrument Administrator
Site: NECSA
Measured : 09/09/11 16:09:13

Sample

Material	HKL	Wavelength	2theta	Poisson	Young	s1	1/2s2	Arx
Ti	(2 1 3)	0.154055 (Cu_)Ka1	139.32	0.32	112994.00	-2.832E-6	1.168E-5	1.00

Corrections : Absorption , Background (5) , Polarisation , Smooth , K alpha 2 (0.50)

Peak Evaluation Method : Pearson VII

Stresss Model : Biaxial + Shear

Normal : -142.7 ± 11.6 **Shear :** 0.9 ±4.3 (**Phi :** 0 **Psi :** 90)

Pseudo-Hydro : 150.1 ± 12.5

Stress Tensor :

-309.8 ± 11.6	-102.9 ± 12.1	0.9 ± 4.3
-102.9 ± 12.1	-142.7 ± 11.6	4.7 ± 4.3
0.9 ± 4.3	4.7 ± 4.3	0.0 ± 0.0

F.12 Full stress tensor report for Grade 4 at 1.00 mm DOC and 200 m/min

9/15/2011 10:36:09 AM
Project: Stress_2D
Operator: Bruker Instrument Administrator
Site: NECSA
Measured : 09/12/11 10:47:00

Sample

Material	HKL	Wavelength	2theta	Poisson	Young	s1	1/2s2	Arx
Ti	(2 1 3)	0.154055 (Cu)Ka1	139.32	0.32	112994.00	-2.832E-6	1.168E-5	1.00

Corrections : Absorption , Background (5) , Polarisation , Smooth , K alpha 2 (0.50)

Peak Evaluation Method : Pearson VII

Stresss Model : Biaxial + Shear

Normal : -24.0 ± 15.6 **Shear :** -5.7 ± 5.8 (**Phi :** 0 **Psi :** 90)

Pseudo-Hydro : 198.3 ± 16.9

Stress Tensor :

-51.6 ± 15.7	-54.0 ± 16.5	-5.7 ± 5.8
-54.0 ± 16.5	-24.0 ± 15.6	-29.7 ± 5.8
-5.7 ± 5.8	-29.7 ± 5.8	0.0 ± 0.0

F.13 Full stress tensor report for Grade 4 at 1.00 mm DOC and 250 m/min

9/15/2011 10:39:44 AM
Project: Stress_2D
Operator: Bruker Instrument Administrator
Site: NECSA
Measured : 09/12/11 13:44:28

Sample

Material	HKL	Wavelength	2theta	Poisson	Young	s1	1/2s2	Arx
Ti	(2 1 3)	0.154055 (Cu)Ka1	139.32	0.32	112994.00	-2.832E-6	1.168E-5	1.00

Corrections : Absorption , Background (5) , Polarisation , Smooth , K alpha 2 (0.50)

Peak Evaluation Method : Pearson VII

Stresss Model : Biaxial + Shear

Normal : -18.1 ± 18.1 **Shear :** 2.8 ± 6.7 (**Phi :** 0 **Psi :** 90)

Pseudo-Hydro : 115.9 ± 19.6

Stress Tensor :

-12.0 ± 18.2	-73.1 ± 19.1	2.8 ± 6.7
-73.1 ± 19.1	-18.1 ± 18.1	-23.0 ± 6.7
2.8 ± 6.7	-23.0 ± 6.7	0.0 ± 0.0

F.14 Full stress tensor report for Grade 4 at 1.00 mm DOC and 300 m/min

9/15/2011 10:43:23 AM
Project: Stress_2D
Operator: Bruker Instrument Administrator
Site: NECSA
Measured : 09/12/11 16:06:51

Sample

Material	HKL	Wavelength	2theta	Poisson	Young	s1	1/2s2	Arx
Ti	(2 1 3)	0.154055 (Cu)Ka1	139.32	0.32	112994.00	-2.832E-6	1.168E-5	1.00

Corrections : Absorption , Background (5) , Polarisation , Smooth , K alpha 2 (0.50)

Peak Evaluation Method : Pearson VII

Stresss Model : Biaxial + Shear

Normal : -29.6 ± 14.3 **Shear :** -3.0 ±5.3 (**Phi :** 0 **Psi :** 90)

Pseudo-Hydro : 160.2 ± 15.5

Stress Tensor :

-34.1 ± 14.4	-52.0 ± 15.1	-3.0 ± 5.3
-52.0 ± 15.1	-29.6 ± 14.3	-30.2 ± 5.3
-3.0 ± 5.3	-30.2 ± 5.3	0.0 ± 0.0

F.15 Full stress tensor report for Grade 5 at 0.25 mm DOC and finish cut

8/23/2011 4:26:57 PM
Project: Stress_2D
Operator: Bruker Instrument Administrator
Site: NECSA
Measured : 07/29/11 09:44:52

Sample

Material	HKL	Wavelength	2theta	Poisson	Young	s1	1/2s2	Arx
Ti	(2 1 3)	0.154055 (Cu)Ka1	139.32	0.32	112994.00	-2.832E-6	1.168E-5	1.00

Corrections : Absorption , Background (5) , Polarisation , Smooth , K alpha 2 (0.50)

Peak Evaluation Method : Pearson VII

Stresss Model : Biaxial + Shear

Normal : -245.8 ± 15.0 **Shear :** -38.2 ±7.2 (**Phi :** 90 **Psi :** 90)

Pseudo-Hydro : -1932.3 ± 16.5

Stress Tensor :

-245.8 ± 15.0	-4.2 ± 15.3	-1.4 ± 7.3
-4.2 ± 15.3	-269.4 ± 15.5	-38.2 ± 7.2
-1.4 ± 7.3	-38.2 ± 7.2	0.0 ± 0.0

F.16 Full stress tensor report for Grade 5 at 0.25 mm DOC and 70 m/min

8/23/2011 2:58:44 PM
Project: Stress_2D
Operator: Bruker Instrument Administrator
Site: NECSA
Measured : 07/27/11 14:38:33

Sample

Material	HKL	Wavelength	2theta	Poisson	Young	s1	1/2s2	Arx
Ti	(2 1 3)	0.154055 (Cu)Ka1	139.32	0.32	112994.00	-2.832E-6	1.168E-5	1.00

Corrections : Absorption , Background (5) , Polarisation , Smooth , K alpha 2 (0.50)

Peak Evaluation Method : Pearson VII

Stresss Model : Biaxial + Shear

Normal : -292.3 ± 11.8 **Shear :** 3.3 ±5.6 (**Phi :** 90 **Psi :** 90)

Pseudo-Hydro : -2014.8 ± 12.9

Stress Tensor :

-292.3 ± 11.8	-104.7 ± 12.0	2.9 ± 5.7
-104.7 ± 12.0	-235.5 ± 12.2	3.3 ± 5.6
2.9 ± 5.7	3.3 ± 5.6	0.0 ± 0.0

F.17 Full stress tensor report for Grade 5 at 0.25 mm DOC and 100 m/min

8/23/2011 3:05:22 PM
Project: Stress_2D
Operator: Bruker Instrument Administrator
Site: NECSA
Measured : 07/25/11 16:49:55

Sample

Material	HKL	Wavelength	2theta	Poisson	Young	s1	1/2s2	Arx
Ti	(2 1 3)	0.154055 (Cu)Ka1	139.32	0.32	112994.00	-2.832E-6	1.168E-5	1.00

Corrections : Absorption , Background (5) , Polarisation , Smooth , K alpha 2 (0.50)

Peak Evaluation Method : Pearson VII

Stresss Model : Biaxial + Shear

Normal : -160.8 ± 14.5 **Shear :** -8.0 ±6.9 (**Phi :** 0 **Psi :** 90)

Pseudo-Hydro : -1950.3 ± 16.0

Stress Tensor :

-387.3 ± 15.5	-146.2 ± 14.5	-8.0 ± 6.9
-146.2 ± 14.5	-160.8 ± 14.5	-12.6 ± 6.9
-8.0 ± 6.9	-12.6 ± 6.9	0.0 ± 0.0

F.18 Full stress tensor report for Grade 5 at 0.25 mm DOC and 125 m/min

8/23/2011 3:21:26 PM
Project: Stress_2D
Operator: Bruker Instrument Administrator
Site: NECSA
Measured : 07/26/11 15:40:39

Sample

Material	HKL	Wavelength	2theta	Poisson	Young	s1	1/2s2	Arx
Ti	(2 1 3)	0.154055 (Cu_)Ka1	139.32	0.32	112994.00	-2.832E-6	1.168E-5	1.00

Corrections : Absorption , Background (5) , Polarisation , Smooth , K alpha 2 (0.50)

Peak Evaluation Method : Pearson VII

Stresss Model : Biaxial + Shear

Normal : -203.6 ± 11.1 **Shear :** -18.0 ±5.3 (**Phi :** 90 **Psi :** 90)

Pseudo-Hydro : -1924.0 ± 12.2

Stress Tensor :

-203.6 ± 11.1	-107.8 ± 11.3	-13.5 ± 5.4
-107.8 ± 11.3	-102.6 ± 11.5	-18.0 ± 5.3
-13.5 ± 5.4	-18.0 ± 5.3	0.0 ± 0.0

F.19 Full stress tensor report for Grade 5 at 0.25 mm DOC and 150 m/min

8/23/2011 3:28:04 PM
Project: Stress_2D
Operator: Bruker Instrument Administrator
Site: NECSA
Measured : 07/27/11 09:37:45

Sample

Material	HKL	Wavelength	2theta	Poisson	Young	s1	1/2s2	Arx
Ti	(2 1 3)	0.154055 (Cu_)Ka1	139.32	0.32	112994.00	-2.832E-6	1.168E-5	1.00

Corrections : Absorption , Background (5) , Polarisation , Smooth , K alpha 2 (0.50)

Peak Evaluation Method : Pearson VII

Stresss Model : Biaxial + Shear

Normal : 25.6 ± 10.8 **Shear :** -16.6 ±5.2 (**Phi :** 90 **Psi :** 90)

Pseudo-Hydro : -1921.5 ± 11.9

Stress Tensor :

25.6 ± 10.8	-99.1 ± 11.0	-16.3 ± 5.3
-99.1 ± 11.0	2.7 ± 11.1	-16.6 ± 5.2
-16.3 ± 5.3	-16.6 ± 5.2	0.0 ± 0.0

F.20 Full stress tensor report for Grade 5 at 0.25 mm DOC and 175 m/min

8/23/2011 3:50:06 PM

Project: Stress_2D

Operator: Bruker Instrument Administrator

Site: NECSA

Measured : 07/29/11 15:02:56

Sample

Material	HKL	Wavelength	2theta	Poisson	Young	s1	1/2s2	Arx
Ti	(2 1 3)	0.154055 (Cu_)Ka1	139.32	0.32	112994.00	-2.832E-6	1.168E-5	1.00

Corrections : Absorption , Background (5) , Polarisation , Smooth , K alpha 2 (0.50)

Peak Evaluation Method : Pearson VII

Stresss Model : Biaxial + Shear

Normal : 168.5 ± 13.0 **Shear :** -19.9 ± 6.2 (**Phi :** 90 **Psi :** 90)

Pseudo-Hydro : -1990.6 ± 14.2

Stress Tensor :

168.5 ± 13.0	-87.6 ± 13.2	-12.1 ± 6.3
-87.6 ± 13.2	99.3 ± 13.3	-19.9 ± 6.2
-12.1 ± 6.3	-19.9 ± 6.2	0.0 ± 0.0

F.21 Full stress tensor report for Grade 5 at 0.25 mm DOC and 200 m/min

8/23/2011 4:19:44 PM

Project: Stress_2D

Operator: Bruker Instrument Administrator

Site: NECSA

Measured : 05/09/11 11:13:33

Sample

Material	HKL	Wavelength	2theta	Poisson	Young	s1	1/2s2	Arx
Ti	(2 1 3)	0.154055 (Cu_)Ka1	139.32	0.32	112994.00	-2.832E-6	1.168E-5	1.00

Corrections : Absorption , Background (5) , Polarisation , Smooth , K alpha 2 (0.50)

Peak Evaluation Method : Pearson VII

Stresss Model : Biaxial + Shear

Normal : -94.6 ± 10.9 **Shear :** 14.3 ± 5.2 (**Phi :** 90 **Psi :** 90)

Pseudo-Hydro : -1855.8 ± 11.9

Stress Tensor :

-94.6 ± 10.9	-60.7 ± 11.0	3.8 ± 5.3
-60.7 ± 11.0	27.3 ± 11.2	14.3 ± 5.2
3.8 ± 5.3	14.3 ± 5.2	0.0 ± 0.0

F.22 Full stress tensor report for Grade 5 at 1.00 mm DOC and finish cut

8/23/2011 2:43:03 PM
Project: Stress_2D
Operator: Bruker Instrument Administrator
Site: NECSA
Measured : 05/25/11 16:12:05

Sample

Material	HKL	Wavelength	2theta	Poisson	Young	s1	1/2s2	Arx
Ti	(2 1 3)	0.154055 (Cu)Ka1	139.32	0.32	112994.00	-2.832E-6	1.168E-5	1.00

Corrections : Absorption , Background (5) , Polarisation , Smooth , K alpha 2 (0.50)

Peak Evaluation Method : Pearson VII

Stresss Model : Biaxial + Shear

Normal : -105.0 ± 10.6 **Shear :** 32.2 ±5.1 (**Phi :** 90 **Psi :** 90)

Pseudo-Hydro : -1935.0 ± 11.6

Stress Tensor :

-105.0 ± 10.6	15.2 ± 10.8	2.7 ± 5.2
15.2 ± 10.8	-224.6 ± 10.9	32.2 ± 5.1
2.7 ± 5.2	32.2 ± 5.1	0.0 ± 0.0

F.23 Full stress tensor report for Grade 5 at 1.00 mm DOC and 70 m/min

8/23/2011 2:26:23 PM
Project: Stress_2D
Operator: Bruker Instrument Administrator
Site: NECSA
Measured : 05/25/11 10:25:07

Sample

Material	HKL	Wavelength	2theta	Poisson	Young	s1	1/2s2	Arx
Ti	(2 1 3)	0.154055 (Cu)Ka1	139.32	0.32	112994.00	-2.832E-6	1.168E-5	1.00

Corrections : Absorption , Background (5) , Polarisation , Smooth , K alpha 2 (0.50)

Peak Evaluation Method : Pearson VII

Stresss Model : Biaxial + Shear

Normal : -358.8 ± 19.5 **Shear :** -14.6 ±9.4 (**Phi :** 90 **Psi :** 90)

Pseudo-Hydro : -1882.0 ± 21.4

Stress Tensor :

-358.8 ± 19.5	-121.9 ± 19.7	4.4 ± 9.5
-121.9 ± 19.7	-157.5 ± 20.1	-14.6 ± 9.4
4.4 ± 9.5	-14.6 ± 9.4	0.0 ± 0.0

F.24 Full stress tensor report for Grade 5 at 1.00 mm DOC and 100 m/min

2012/04/20 05:08:59 PM
Project: Stress_2D
Operator: Bruker Instrument Administrator
Site: NECSA
Measured : 04/20/12 16:54:30

Sample

Material	HKL	Wavelength	2theta	Poisson	Young	s1	1/2s2	Arx
Ti	(2 1 3)	0.154055 (Cu)Ka1	139.32	0.32	112994.00	-2.832E-6	1.168E-5	1.00

Corrections : Absorption , Background (5) , Polarisation , Smooth , K alpha 2 (0.50)

Peak Evaluation Method : Pearson VII

Stresss Model : Biaxial + Shear

Normal : -396.6 ± 15.7 **Shear :** -3.1 ±9.3 (**Phi :** 90 **Psi :** 90)

Pseudo-Hydro : -2031.1 ± 18.9

Stress Tensor :

-396.6 ± 15.7	-154.2 ± 16.3	6.9 ± 10.1
-154.2 ± 16.3	-87.0 ± 17.5	-3.1 ± 9.3
6.9 ± 10.1	-3.1 ± 9.3	0.0 ± 0.0

F.25 Full stress tensor report for Grade 5 at 1.00 mm DOC and 125 m/min

2012/04/23 05:03:27 PM
Project: Stress_2D
Operator: Bruker Instrument Administrator
Site: NECSA
Measured : 04/23/12 10:57:26

Sample

Material	HKL	Wavelength	2theta	Poisson	Young	s1	1/2s2	Arx
Ti	(2 1 3)	0.154055 (Cu)Ka1	139.32	0.32	112994.00	-2.832E-6	1.168E-5	1.00

Corrections : Absorption , Background (5) , Polarisation , Smooth , K alpha 2 (0.50)

Peak Evaluation Method : Pearson VII

Stresss Model : Biaxial + Shear

Normal : -280.6 ± 8.9 **Shear :** -8.4 ±4.2 (**Phi :** 90 **Psi :** 90)

Pseudo-Hydro : -2089.9 ± 10.0

Stress Tensor :

-280.6 ± 8.9	-221.3 ± 9.2	-15.6 ± 4.5
-221.3 ± 9.2	-77.6 ± 10.0	-8.4 ± 4.2
-15.6 ± 4.5	-8.4 ± 4.2	0.0 ± 0.0

F.26 Full stress tensor report for Grade 5 at 1.00 mm DOC and 150 m/min

8/24/2011 11:39:21 AM
Project: Stress_2D
Operator: Bruker Instrument Administrator
Site: NECSA
Measured : 04/21/11 15:36:18

Sample

Material	HKL	Wavelength	2theta	Poisson	Young	s1	1/2s2	Arx
Ti	(2 1 3)	0.154055 (Cu_)Ka1	139.32	0.32	112994.00	-2.832E-6	1.168E-5	1.00

Corrections : Absorption , Background (5) , Polarisation , Smooth , K alpha 2 (0.50)

Peak Evaluation Method : Pearson VII

Stresss Model : Biaxial + Shear

Normal : -119.5 ± 9.4 **Shear :** 15.6 ± 4.5 (**Phi :** 90 **Psi :** 90)

Pseudo-Hydro : -2413.4 ± 10.3

Stress Tensor :

-119.5 ± 9.4	-95.0 ± 9.5	5.5 ± 4.6
-95.0 ± 9.5	-21.5 ± 9.7	15.6 ± 4.5
5.5 ± 4.6	15.6 ± 4.5	0.0 ± 0.0

F.27 Full stress tensor report for Grade 5 at 1.00 mm DOC and 175 m/min

8/23/2011 2:33:57 PM
Project: Stress_2D
Operator: Bruker Instrument Administrator
Site: NECSA
Measured : 05/27/11 09:06:07

Sample

Material	HKL	Wavelength	2theta	Poisson	Young	s1	1/2s2	Arx
Ti	(2 1 3)	0.154055 (Cu_)Ka1	139.32	0.32	112994.00	-2.832E-6	1.168E-5	1.00

Corrections : Absorption , Background (5) , Polarisation , Smooth , K alpha 2 (0.50)

Peak Evaluation Method : Pearson VII

Stresss Model : Biaxial + Shear

Normal : -250.2 ± 11.3 **Shear :** 15.1 ± 5.4 (**Phi :** 90 **Psi :** 90)

Pseudo-Hydro : -2000.6 ± 12.4

Stress Tensor :

-250.2 ± 11.3	-99.1 ± 11.5	2.7 ± 5.5
-99.1 ± 11.5	-176.6 ± 11.7	15.1 ± 5.4
2.7 ± 5.5	15.1 ± 5.4	0.0 ± 0.0

F.28 Full stress tensor report for Grade 5 at 1.00 mm DOC and 200 m/min

2012/04/24 09:45:18 AM

Project: Stress_2D

Operator: Bruker Instrument Administrator

Site: NECSA

Measured : 04/23/12 16:36:59

Sample

Material	HKL	Wavelength	2theta	Poisson	Young	s1	1/2s2	Arx
Ti	(2 1 3)	0.154055 (Cu)Ka1	139.32	0.32	112994.00	-2.832E-6	1.168E-5	1.00

Corrections : Absorption , Background (5) , Polarisation , Smooth , K alpha 2 (0.50)

Peak Evaluation Method : Pearson VII

Stresss Model : Biaxial + Shear

Normal : -107.6 ± 12.6 **Shear :** 17.9 ±5.9 (**Phi :** 90 **Psi :** 90)

Pseudo-Hydro : -1940.2 ± 14.2

Stress Tensor :

-107.6 ± 12.6	-147.5 ± 13.0	8.9 ± 6.5
-147.5 ± 13.0	26.2 ± 14.1	17.9 ± 5.9
8.9 ± 6.5	17.9 ± 5.9	0.0 ± 0.0

F.29 Extracted Grade 4 and 5 residual stress data

Table F.1 - Extracted Grade 4 residual stresses

0.25 mm depth of cut							
		σ_{11}	**error**	**σ_{22}**	**error**	**σ_{12}**	**error**
Cutting speed (m/min)	**0**	-145.9	12.3	-279.5	12.3	-9.4	12.9
	70	-174.8	12.9	-60.4	12.9	-86.9	13.6
	100	-24.8	19.7	35.8	19.6	-97.4	20.7
	150	50.3	18.2	117.8	18.1	-31.4	19.0
	200	-82.7	18.1	-4.2	18.1	-73.9	19.0
	250	135.3	18.6	70.5	18.5	-34.1	19.5
	300	42.6	18.0	46.6	17.9	-41.5	18.8
1.00 mm depth of cut							
		σ_{11}	**error**	**σ_{22}**	**error**	**σ_{12}**	**error**
Cutting speed (m/min)	**0**	-254.9	10.3	-527.8	10.3	25.2	10.8
	70	-149.3	10.8	1.8	10.8	-71.2	14.8
	100	-179.8	14.2	-56.3	10.0	-84.4	11.4
	150	-309.8	11.6	-142.7	11.6	11.6	12.1
	200	-51.6	15.7	-24.0	15.6	-54.0	16.5
	250	-12.0	18.2	-18.1	18.1	-73.1	19.1
	300	-34.1	14.4	-29.6	14.3	-52.0	15.1

Table F.2 - Extracted Grade 5 residual stresses

0.25 mm depth of cut							
		σ_{11}	error	σ_{22}	error	σ_{12}	error
Cutting speed (m/min)	**0**	-245.8	15.0	-269.4	15.5	-4.2	15.3
	70	-292.3	11.8	-235.5	12.2	-104.7	12.0
	100	-387.3	15.5	-160.8	14.5	-146.2	14.5
	125	-203.6	11.1	-102.6	11.5	-107.8	11.3
	150	25.6	10.8	2.7	11.1	-99.1	11.0
	175	168.5	13.0	99.3	13.3	-87.6	13.2
	200	-94.6	10.9	27.3	11.2	-60.7	11.0
1.00 mm depth of cut							
		σ_{11}	error	σ_{22}	error	σ_{12}	error
Cutting speed (m/min)	**0**	-105.0	10.6	-224.6	10.9	15.2	10.8
	70	-358.8	19.5	-157.5	20.1	-121.9	19.7
	100	-396.6	15.7	-87.0	17.5	-154.2	16.3
	125	-280.6	8.9	-77.6	10.0	-221.3	9.2
	150	-119.5	9.4	-21.5	9.7	-95.0	9.5
	175	-250.2	11.3	-176.6	11.7	-99.1	11.5
	200	-107.6	12.6	26.2	14.1	-147.5	13.0

Appendix G: Analysed Microstructure Images and Extracted Deformation Data

A range of images are analysed for each sample, from which several measurements are done. Only one image per sample however is presented in this section. The deformation angles measured in the images depict the angles between the grain orientation and machined surface. The measurements used in the investigation however, represent the angles between the shifted grains and a perpendicular line to the machined surface. These angles are presented in Table G.1. The depth at which these deformations reach into the material is the deformation depth. The extracted deformation depth averages are presented in Table G.2.

G.1 Microstructural images depicting deformation angle for Grade 4 at 0.25 mm DOC

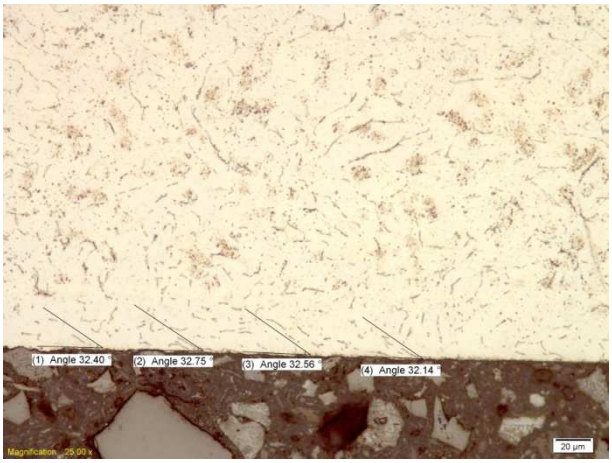

Figure G.1 - Grade 4 deformation angle at 0.25 mm DOC and 70 m/min

Figure G.2 - Grade 4 deformation angle at 0.25 mm DOC and 100 m/min

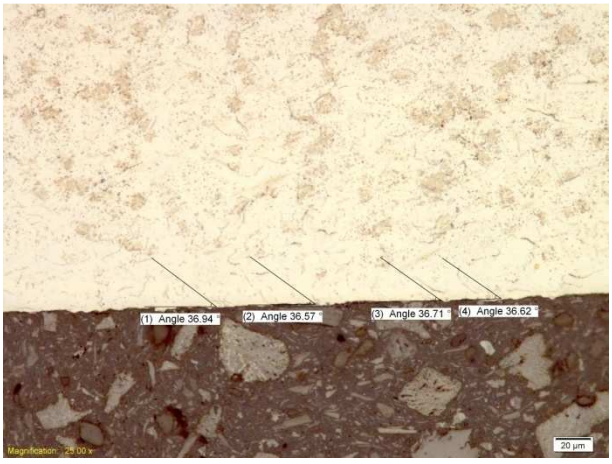

Figure G.3 - Grade 4 deformation angle at 0.25 mm DOC and 150 m/min

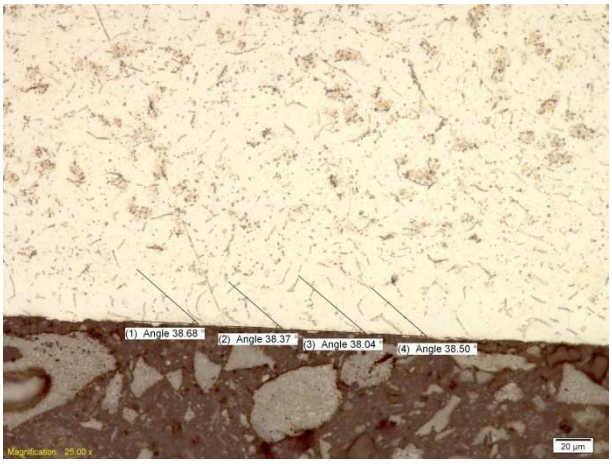

Figure G.4 - Grade 4 deformation angle at 0.25 mm DOC and 200 m/min

Figure G.5 - Grade 4 deformation angle at 0.25 mm DOC and 250 m/min

Figure G.6 - Grade 4 deformation angle at 0.25 mm DOC and 300 m/min

G.2 Microstructural images depicting deformation angle for Grade 4 at 1.00 mm DOC

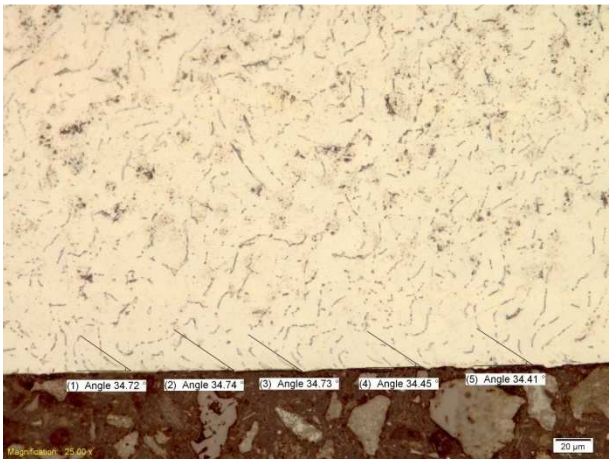

Figure G.7 - Grade 4 deformation angle at 1.00 mm DOC and 70 m/min

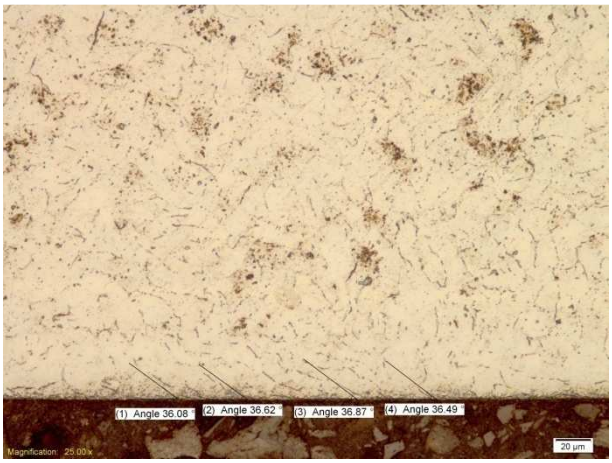

Figure G.8 - Grade 4 deformation angle at 1.00 mm DOC and 100 m/min

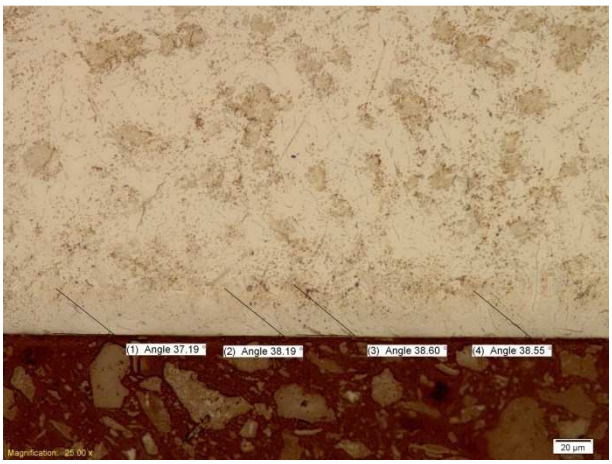

Figure G.9 - Grade 4 deformation angle at 1.00 mm DOC and 150 m/min

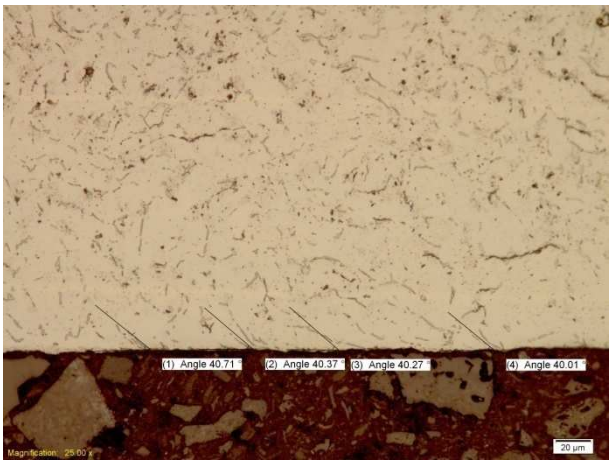

Figure G.10 - Grade 4 deformation angle at 1.00 mm DOC and 200 m/min

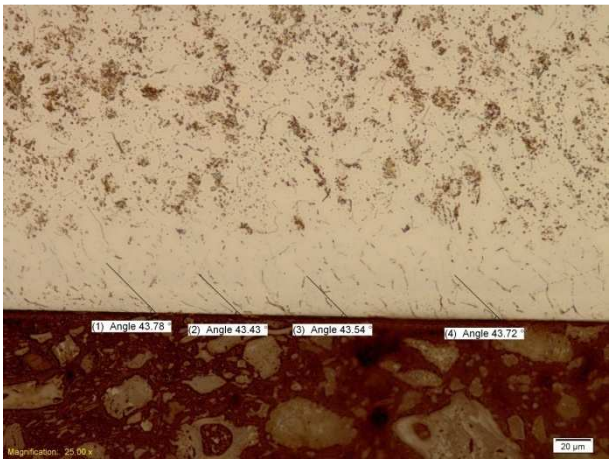

Figure G.11 - Grade 4 deformation angle at 1.00 mm DOC and 250 m/min

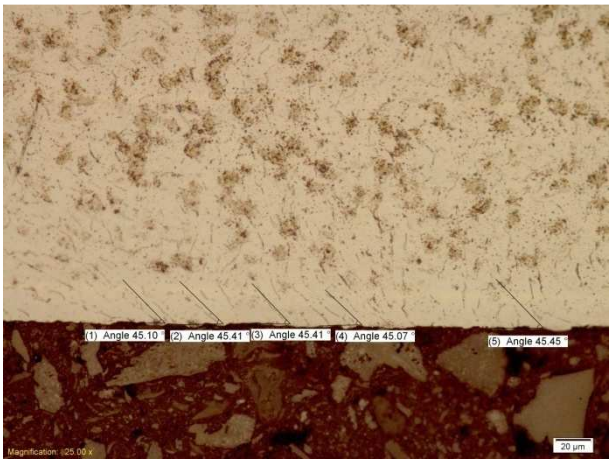

Figure G.12 - Grade 4 deformation angle at 1.00 mm DOC and 300 m/min

G.3 Microstructural images depicting deformation angle for Grade 5 at 0.25 mm DOC

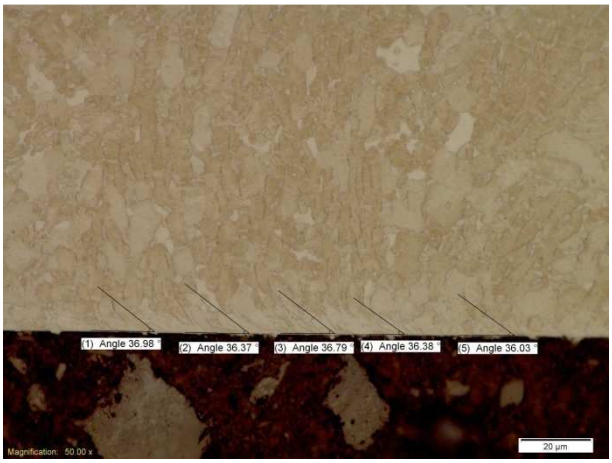

Figure G.13 - Grade 5 deformation angle at 0.25 mm DOC and 70 m/min

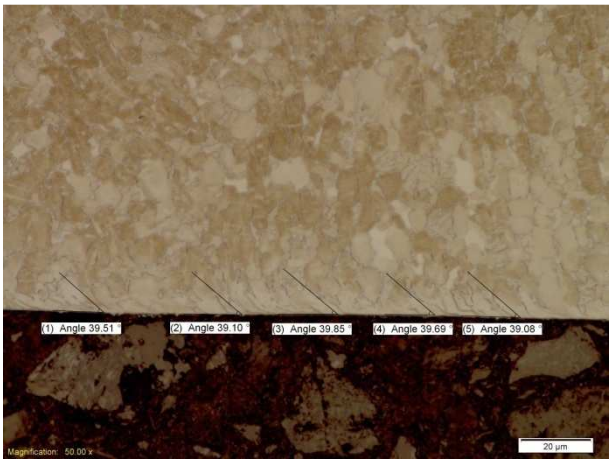

Figure G.14 - Grade 5 deformation angle at 0.25 mm DOC and 100 m/min

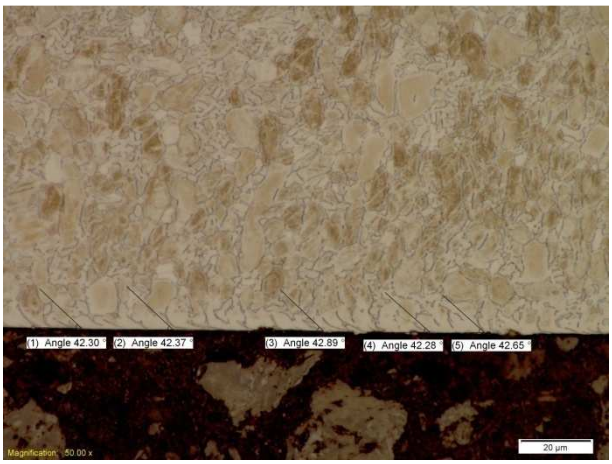

Figure G.15 - Grade 5 deformation angle at 0.25 mm DOC and 125 m/min

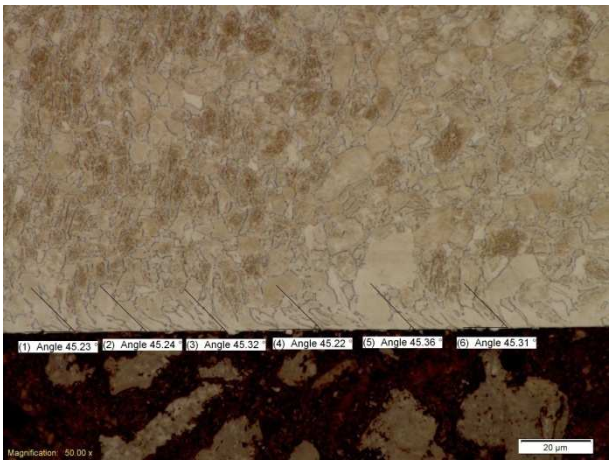

Figure G.16 - Grade 5 deformation angle at 0.25 mm DOC and 150 m/min

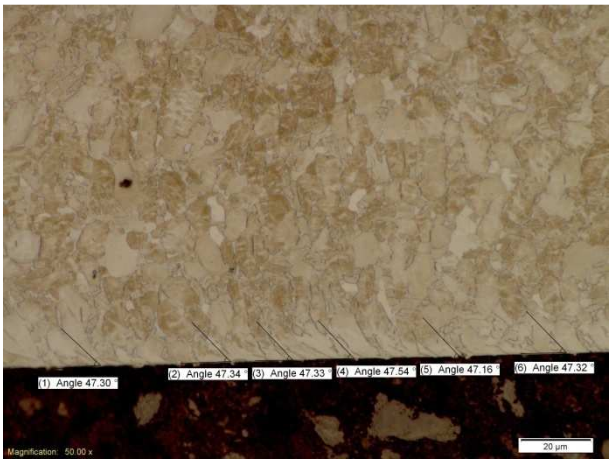

Figure G.17 - Grade 5 deformation angle at 0.25 mm DOC and 175 m/min

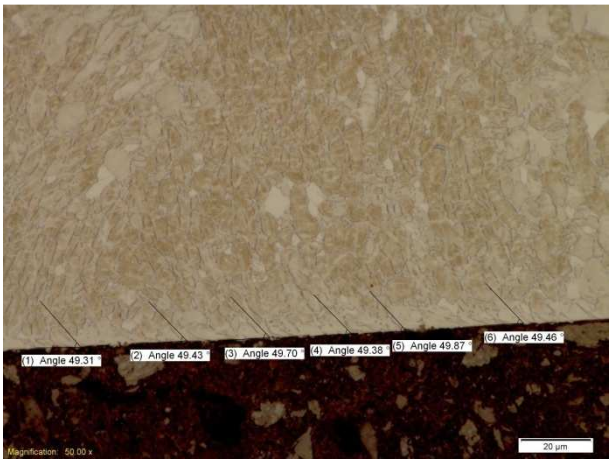

Figure G.18 - Grade 5 deformation angle at 0.25 mm DOC and 200 m/min

G.4 Microstructural images depicting deformation angle for Grade 5 at 1.00 mm DOC

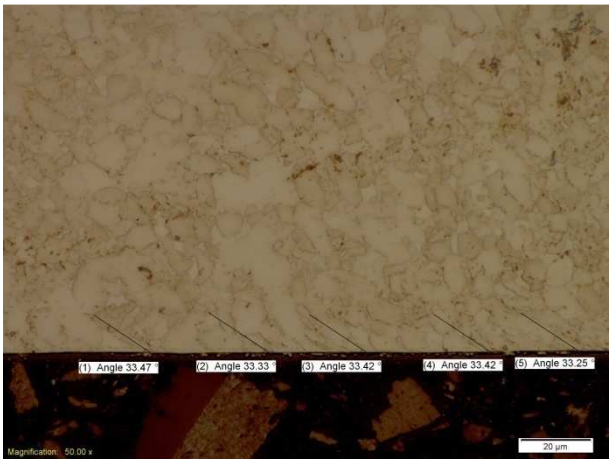

Figure G.19 - Grade 5 deformation angle at 1.00 mm DOC and 70 m/min

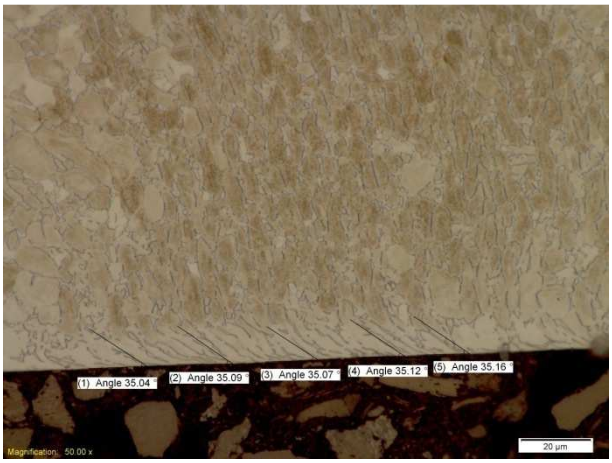

Figure G.20 - Grade 5 deformation angle at 1.00 mm DOC and 100 m/min

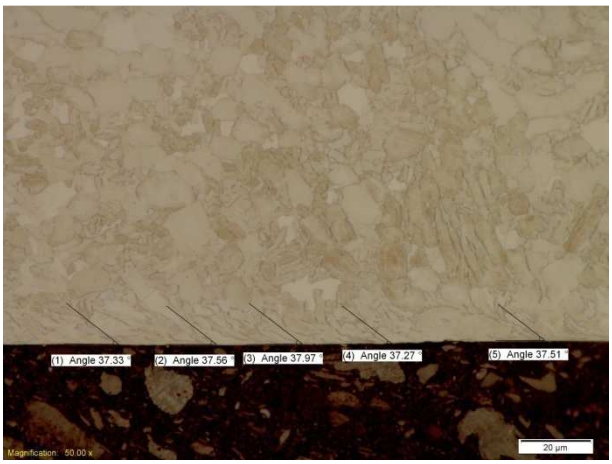

Figure G.21 - Grade 5 deformation angle at 1.00 mm DOC and 125 m/min

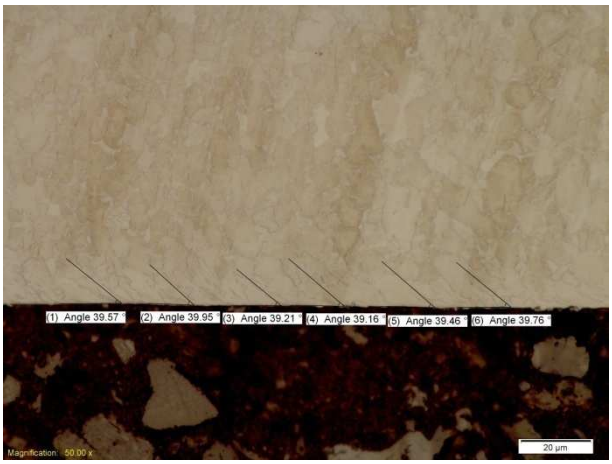

Figure G.22 - Grade 5 deformation angle at 1.00 mm DOC and 150 m/min

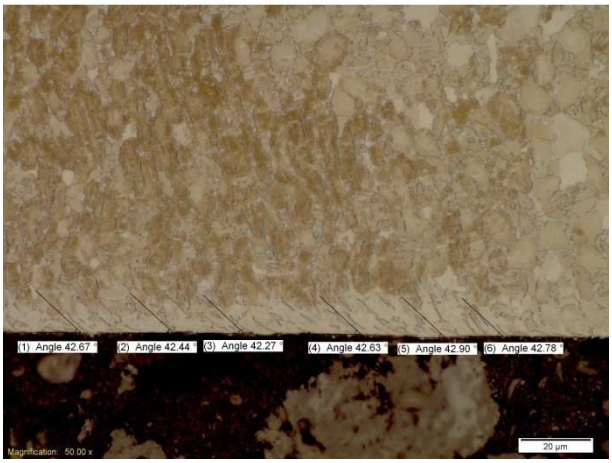

Figure G.23 - Grade 5 deformation angle at 1.00 mm DOC and 175 m/min

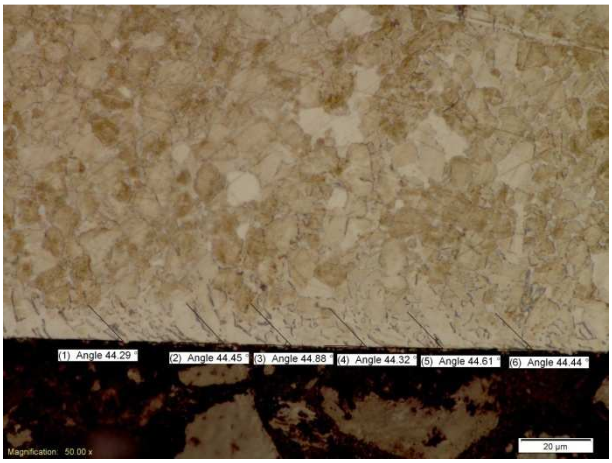

Figure G.24 - Grade 5 deformation angle at 1.00 mm DOC and 200 m/min

G.5 Microstructural images depicting deformation depth for Grade 4 at 0.25 mm DOC

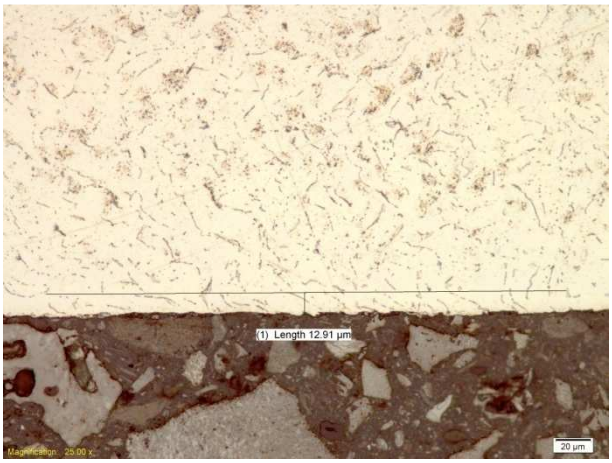

Figure G.25 - Grade 4 deformation depth at 0.25 mm DOC and 70 m/min

Figure G.26 - Grade 4 deformation depth at 0.25 mm DOC and 100 m/min

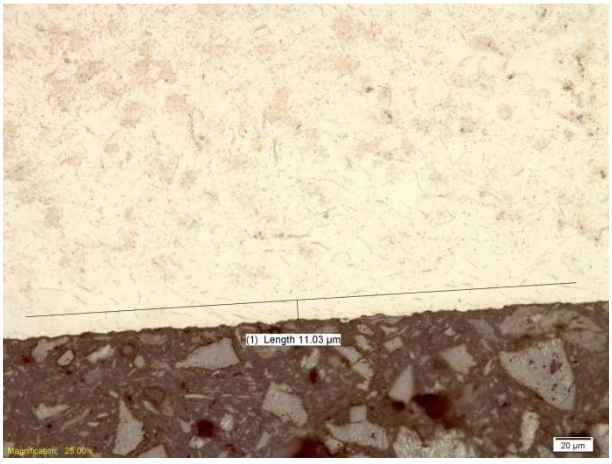

Figure G.27 - Grade 4 deformation depth at 0.25 mm DOC and 150 m/min

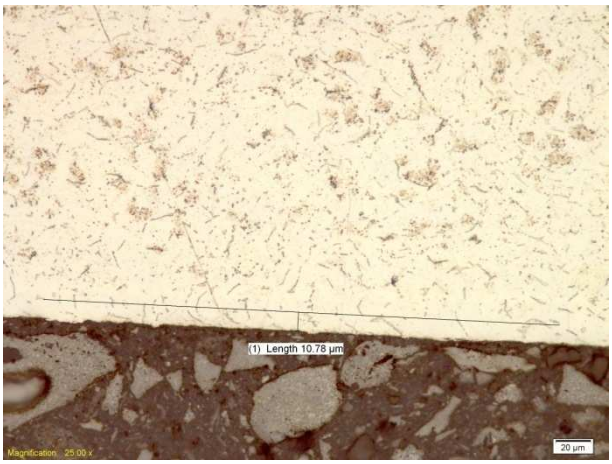

Figure G.28 - Grade 4 deformation depth at 0.25 mm DOC and 200 m/min

Figure G.29 - Grade 4 deformation depth at 0.25 mm DOC and 250 m/min

Figure G.30 - Grade 4 deformation depth at 0.25 mm DOC and 300 m/min

G.6 Microstructural images depicting deformation depth for Grade 4 at 1.00 mm DOC

Figure G.31 - Grade 4 deformation depth at 1.00 mm DOC and 70 m/min

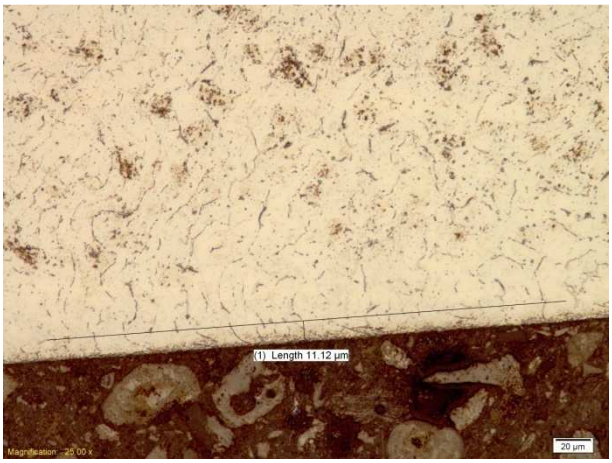

Figure G.32 - Grade 4 deformation depth at 1.00 mm DOC and 100 m/min

Figure G.33 - Grade 4 deformation depth at 1.00 mm DOC and 150 m/min

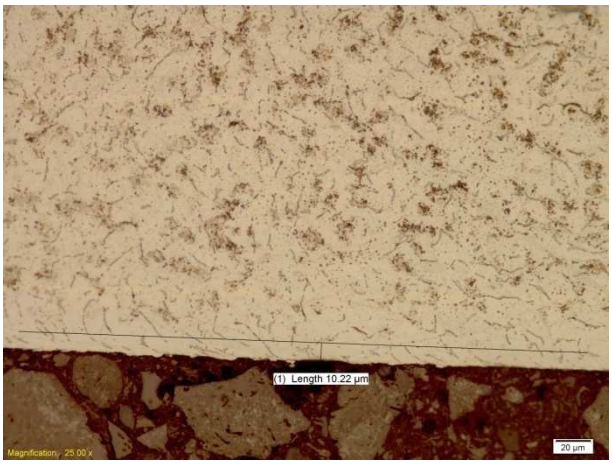

Figure G.34 - Grade 4 deformation depth at 1.00 mm DOC and 200 m/min

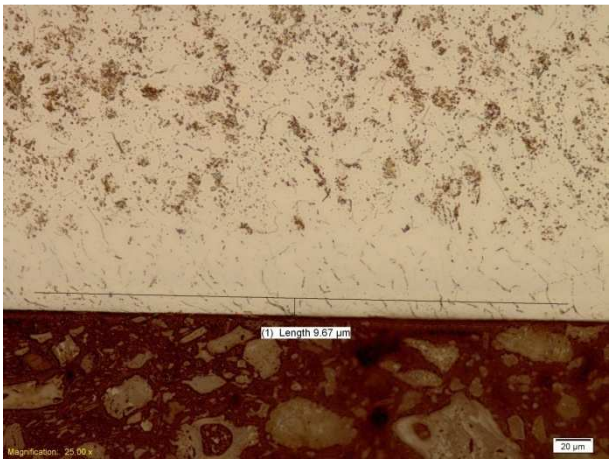

Figure G.35 - Grade 4 deformation depth at 1.00 mm DOC and 250 m/min

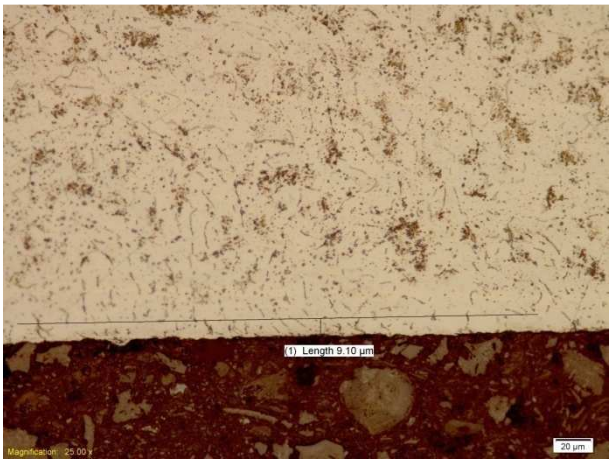

Figure G.36 - Grade 4 deformation depth at 1.00 mm DOC and 300 m/min

G.7 Microstructural images depicting deformation depth for Grade 5 at 0.25 mm DOC

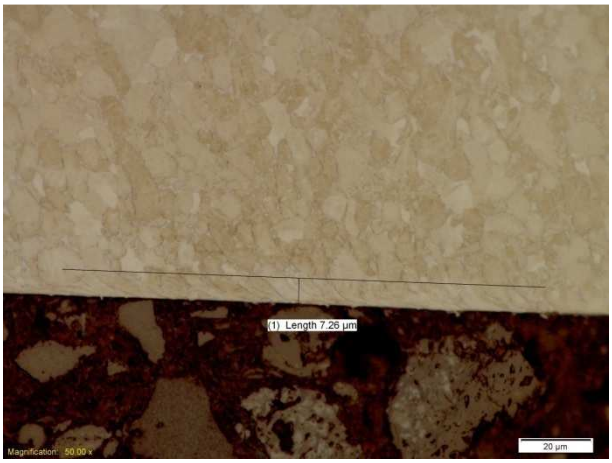

Figure G.37 - Grade 5 deformation depth at 0.25 mm DOC and 70 m/min

Figure G.38 - Grade 5 deformation depth at 0.25 mm DOC and 100 m/min

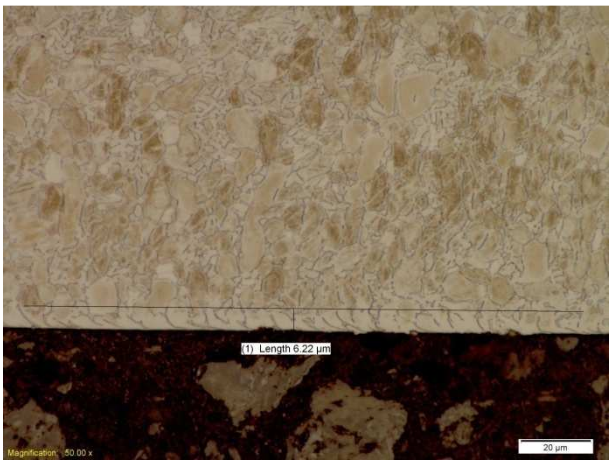

Figure G.39 - Grade 5 deformation depth at 0.25 mm DOC and 125 m/min

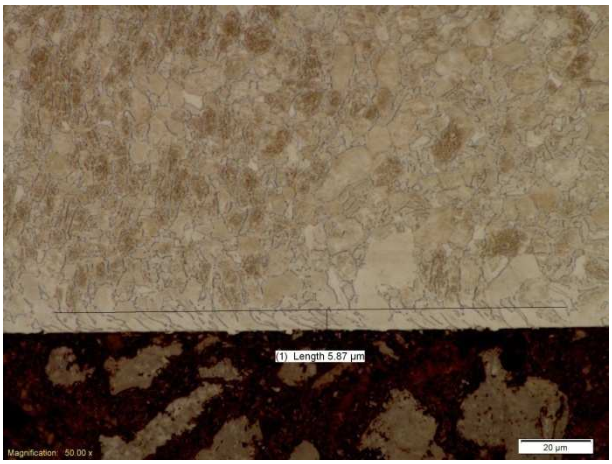

Figure G.40 - Grade 5 deformation depth at 0.25 mm DOC and 150 m/min

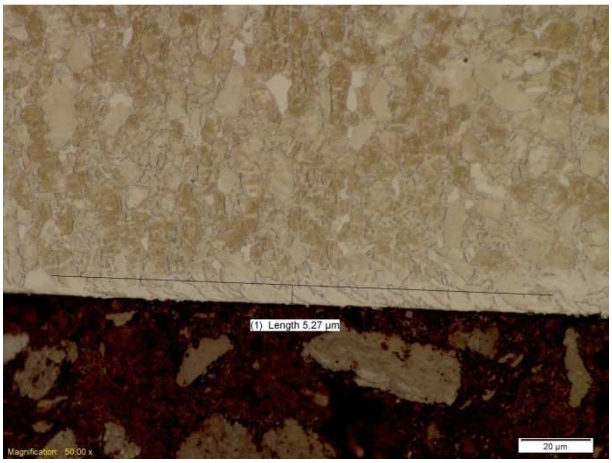

Figure G.41 - Grade 5 deformation depth at 0.25 mm DOC and 175 m/min

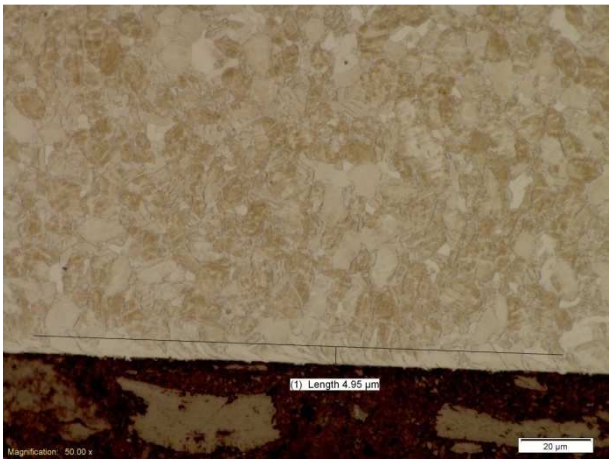

Figure G.42 - Grade 5 deformation depth at 0.25 mm DOC and 200 m/min

G.8 Microstructural images depicting deformation depth for Grade 5 at 1.00 mm DOC

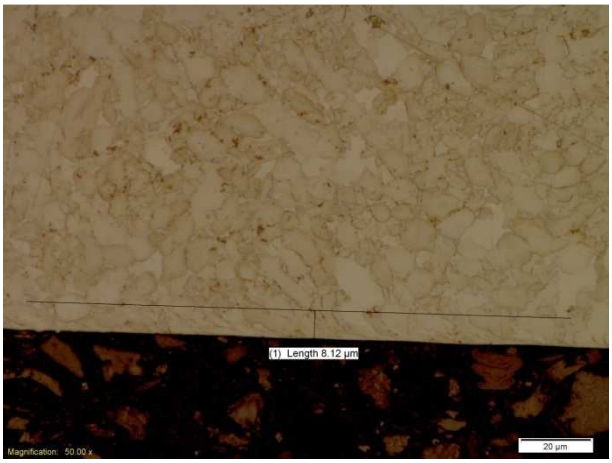

Figure G.43 - Grade 5 deformation depth at 1.00 mm DOC and 70 m/min

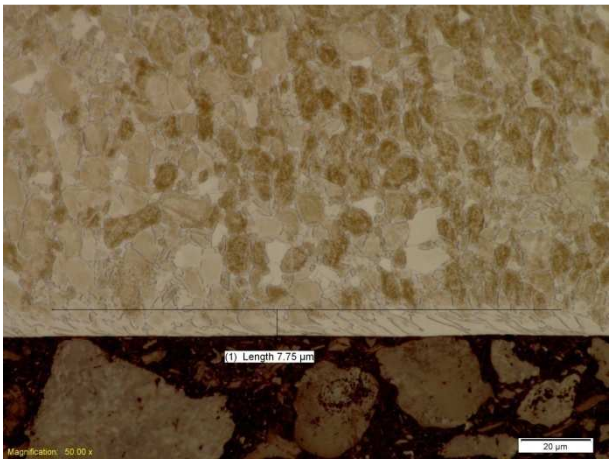

Figure G.44 - Grade 5 deformation depth at 1.00 mm DOC and 100 m/min

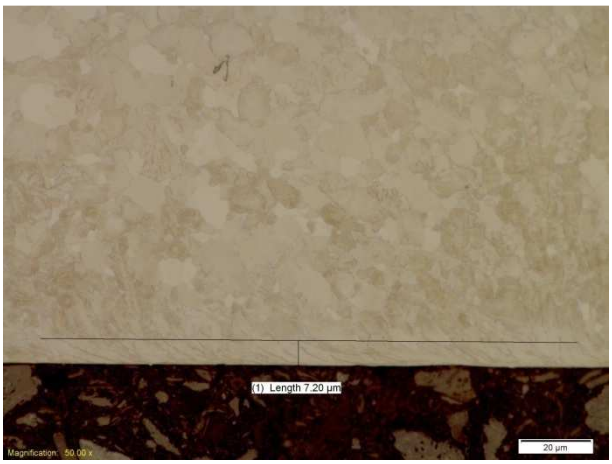

Figure G.45 - Grade 5 deformation depth at 1.00 mm DOC and 125 m/min

Figure G.46 - Grade 5 deformation depth at 1.00 mm DOC and 150 m/min

Figure G.47 - Grade 5 deformation depth at 1.00 mm DOC and 175 m/min

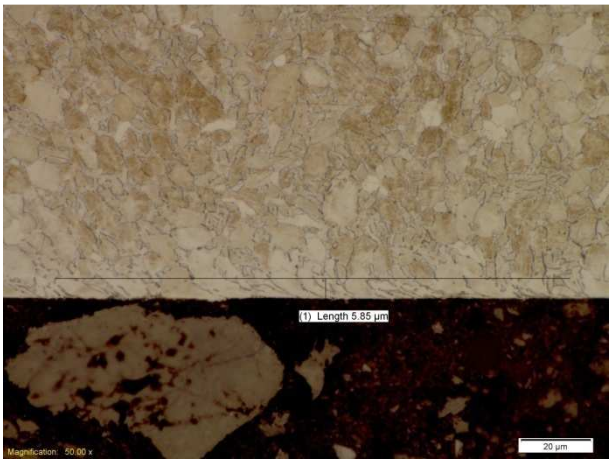

Figure G.48 - Grade 5 deformation depth at 1.00 mm DOC and 200 m/min

G.9 Extracted Grade 4 and 5 deformation data

Table G.1 - Extracted Grade 4 and 5 deformation angles

Grade 4			
Depth of cut (mm)		**0.25**	**1.00**
Cutting speed (m/min)	**70**	57.50	55.50
	100	55.40	53.50
	150	53.30	51.60
	200	51.50	49.60
	250	49.70	46.50
	300	47.50	44.70

Grade 5			
Depth of cut (mm)		**0.25**	**1.00**
Cutting speed (m/min)	**70**	53.40	56.50
	100	50.60	54.40
	125	47.60	52.40
	150	44.70	50.20
	175	42.60	47.50
	200	40.50	45.50

Table G.2 - Extracted Grade 4 and 5 deformation depths

Grade 4			
Depth of cut (mm)		**0.25**	**1.00**
Cutting speed (m/min)	**70**	12.75	11.88
	100	11.54	11.23
	150	11.05	10.64
	200	10.81	10.21
	250	10.17	9.69
	300	9.85	9.08

Grade 5			
Depth of cut (mm)		**0.25**	**1.00**
Cutting speed (m/min)	**70**	7.22	8.16
	100	6.68	7.68
	125	6.24	7.26
	150	5.86	6.83
	175	5.24	6.28
	200	4.96	5.86